

**Structural, electronic and  
magnetic properties of  
GaMnN, MnN and rare-earth  
nitride thin films**

by

Simon Edward Granville

A thesis  
submitted to Victoria University of Wellington  
in fulfilment of the  
requirements for the degree of  
Doctor of Philosophy  
in Physics.

Victoria University of Wellington  
2007



## Abstract

Materials that combine the useful properties of magnetic and semiconducting behaviours are sought for new and developing applications in electronics. In this thesis experimental studies of the properties of disordered thin films of several potentially magnetic semiconducting materials are presented. Previous research on the diluted magnetic semiconductor GaMnN is reviewed as an introduction to a study of GaMnN thin films grown with an ion-assisted deposition technique. Several complementary compositional and structural analysis techniques are used to determine that films can be grown with as much as 18 at. % Mn content and that contain no impurity phases, as are often detected in single crystalline GaMnN preparations with high Mn concentrations. The effects of varying Mn contents on the resistive, optical and magnetic properties of the thin films are investigated. The structural, electronic and magnetic properties of thin films of the potential impurity phase MnN have also been investigated and compared with band structure calculations. Recent predictions that the rare earth nitrides may have extremely useful electronic properties have been almost untested in the literature. A procedure for growing rare earth nitride thin films and capping them to protect from reaction with water vapour allows their resistivity, structural and magnetic properties to be established. The results on GdN, SmN, ErN and DyN support the recent predictions, and a more thorough study on GdN reveals that this material is a ferromagnetic semiconductor below 69 K.



# Acknowledgments

I must thank my PhD supervisors Emeritus Prof. Joe Trodahl and Dr. Ben Ruck for their fantastic help and support throughout the course of this project. In particular I owe Joe greatly for giving me my first small research project in 2000, and getting me hooked on experimental physics research. The opportunities you have both opened for me are most appreciated, and I realise just how lucky I have been to have such knowledgeable, supportive and internationally well-regarded supervisors.

Thanks is also very much due to Dr. Tony Bittar, Dr. Grant Williams and Associate Prof. Pablo Etchegoin for help in innumerable measurements and situations, and who have often been like secondary supervisors to me.

Others who have been of great assistance have been Dr. Felix Budde for sample growth and many other experimental concerns; former and current students Dr. Annette Koo, Andrew Preston, Dr. Daniel Pringle, Florian Kuchler and Nat Lund for their help on my project; Alan Rennie and Grant Franklin for their greatly appreciated work in mechanical manufacturing/liquid He transfer and glass-blowing abilities respectively; Dr. John Kennedy, David Flynn, Prof. Jim Metson, Dr. Nick Strickland, Martin Ryan and Erwan Hemery in New Zealand, Prof. Paul Munroe, Warren McKenzie, Dr. Julie Cairney and Dr. Mark Ridgway in Australia and Prof. Walter Lambrecht in the United States for access to various measurement techniques, equipment and expertise. Thank you also to Dr. Cristiana Grigorescu, Associate Prof. Arthur Smith and Rong Yang. A special thanks to David Housden for vital thesis proofreading as well as showing me how NOT to write acknowledgments.

I gratefully acknowledge funding received from Education New Zealand,

the New Economy Research Fund, Ministry of Research, Science and Technology, Victoria University of Wellington and most of all to the MacDiarmid Institute, Prof. Paul Callaghan and Associate Prof. Kate McGrath for all the chance-of-a-student-lifetime opportunities afforded to me.

Thanks to the VUW Hockey Club for the hockey, the recognition and the friends, to all my flatmates who kept me going for the last  $3\frac{1}{2}$  years, to my SCPS colleagues in Wellington and everyone I met in the MacDiarmid Institute, Sydney, Marseille, Canberra and Tsukuba along the way. Finally, a special thanks to Gabrielle, because I can and you'd tell me I shouldn't.

# Contents

<b>Acknowledgments</b>	<b>iii</b>
<b>Glossary</b>	<b>7</b>
<b>1 Introduction</b>	<b>11</b>
<b>2 Magnetism basics and electrical conduction in disordered materials</b>	<b>17</b>
2.0.1 Terminology . . . . .	17
2.1 Magnetism . . . . .	18
2.1.1 Exchange energy . . . . .	24
2.2 Conduction in disordered materials . . . . .	25
2.2.1 Variable Range Hopping (VRH) . . . . .	25
2.2.2 Weak localisation . . . . .	26
<b>3 GaMnN and MnN</b>	<b>31</b>
3.1 GaMnN . . . . .	31
3.1.1 Theory . . . . .	31
3.1.2 GaMnN preparation and structure . . . . .	36
3.1.3 Electrical conductivity . . . . .	40
3.1.4 Optical properties and Mn impurity level positions .	41
3.1.5 Magnetism . . . . .	42
3.2 MnN . . . . .	44
3.3 Summary and Outlook . . . . .	46
<b>4 Growth</b>	<b>49</b>
4.1 GaMnN and MnN films . . . . .	49

4.1.1	Ion-assisted deposition details . . . . .	51
4.2	Rare Earth Nitride films . . . . .	53
4.2.1	Growth details . . . . .	54
<b>5</b>	<b>Experimental Techniques</b>	<b>57</b>
5.1	Introduction . . . . .	57
5.2	Composition - Ion beam analysis (IBA) . . . . .	57
5.2.1	Rutherford backscattering spectroscopy (RBS) . . . . .	58
5.2.2	Nuclear Reaction Analysis (NRA) . . . . .	59
5.2.3	Particle Induced X-ray Emission (PIXE) . . . . .	60
5.2.4	Secondary ion mass spectroscopy (SIMS) . . . . .	60
5.3	Structure . . . . .	61
5.3.1	X-ray Diffraction (XRD) . . . . .	61
5.3.2	Transmission Electron Microscopy (TEM) . . . . .	63
5.3.3	X-ray absorption and emission spectroscopies . . . . .	64
5.3.4	Raman spectroscopy . . . . .	67
5.4	DC Electrical Resistivity . . . . .	69
5.4.1	Measurement Technique . . . . .	69
5.4.2	Resistance Measurement . . . . .	71
5.4.3	Temperature Measurement . . . . .	72
5.5	Optical absorption . . . . .	73
5.5.1	Optical reflection and transmission (300-1200 nm) . . . . .	73
5.5.2	Spectroscopic ellipsometry (SE) (200-750 nm) . . . . .	75
5.5.3	Fourier transform infra-red measurements - MnN . . . . .	76
5.6	Band structure calculations - MnN . . . . .	76
5.7	Magnetisation measurements . . . . .	77
<b>6</b>	<b>Composition and Structure of GaMnN and MnN films</b>	<b>81</b>
6.1	Introduction . . . . .	81
6.2	GaMnN . . . . .	82
6.2.1	Composition . . . . .	82
6.2.2	Structure . . . . .	84
6.3	MnN . . . . .	99
6.3.1	Composition . . . . .	99
6.3.2	Structure . . . . .	99



6.4	Summary . . . . .	103
6.4.1	GaMnN . . . . .	103
6.4.2	MnN . . . . .	103
<b>7</b>	<b>Electronic, optical and magnetic characteristics</b>	<b>107</b>
7.1	GaMnN . . . . .	107
7.1.1	DC electrical resistivity measurements . . . . .	107
7.1.2	Optical absorption . . . . .	111
7.1.3	Magnetic properties . . . . .	113
7.2	MnN . . . . .	123
7.2.1	Electrical and optical conductivity properties . . . . .	123
7.2.2	X-ray absorption and emission spectroscopies . . . . .	127
7.2.3	Magnetic properties . . . . .	128
7.3	Summary . . . . .	132
7.3.1	GaMnN . . . . .	132
7.3.2	MnN . . . . .	133
<b>8</b>	<b>Rare Earth Nitride Background</b>	<b>135</b>
8.1	Experiment . . . . .	135
8.2	Band Structure - Calculation and Experiment . . . . .	136
8.3	Summary and Outlook . . . . .	140
<b>9</b>	<b>Composition, structure, electronic and magnetic properties of rare earth nitrides</b>	<b>143</b>
9.1	Experimental Techniques . . . . .	143
9.1.1	Composition - Ion Beam Analyses . . . . .	143
9.1.2	Structural analysis . . . . .	144
9.1.3	DC electrical resistivity . . . . .	144
9.1.4	Magnetic behaviour . . . . .	144
9.2	Results . . . . .	145
9.3	Discussion and Summary . . . . .	156
<b>10</b>	<b>Summary and Conclusions</b>	<b>161</b>
10.1	Outlook . . . . .	165
	<b>References</b>	<b>168</b>



# List of Figures

2.1	Field loop for a ferromagnet . . . . .	22
3.1	Positions of Mn dopant energy levels in GaN band structure	32
3.2	Spin-resolved density of states for GaMnN . . . . .	34
4.1	Growth chamber used for deposition of thin films . . . . .	50
5.1	RBS spectrum of GaMnN . . . . .	59
5.2	FIB image of a thin film after ion-beam milling . . . . .	64
5.3	Geometry for resistivity measurement of GaMnN . . . . .	70
6.1	SIMS sputtering yields for GaMnN with low Mn content . .	83
6.2	SIMS sputtering yields for GaMnN with high Mn content . .	83
6.3	XRD patterns of GaMnN with varying Mn and O contents .	85
6.4	Low scattering angle XRD peaks of GaMnN . . . . .	85
6.5	TEM image of low Mn content GaMnN . . . . .	86
6.6	TEM image of high Mn content GaMnN . . . . .	86
6.7	High-resolution TEM image of high Mn content GaMnN . .	88
6.8	Selected area electron diffraction image of high Mn content GaMnN . . . . .	89
6.9	Fourier transform of EXAFS measurement on GaMnN . . . .	90
6.10	Experimental and simulated pseudo-rdfs for GaMnN and alternate phases . . . . .	92
6.11	Absolute Raman spectra of GaMnN taken at various excita- tion energies. . . . .	93
6.12	UV Raman spectra of GaMnN . . . . .	94
6.13	Time-dependent UV Raman spectra of GaMnN . . . . .	96

6.14	UV Raman spectra of GaMnN before and after annealing . .	97
6.15	Expanded 514 nm Raman spectrum of GaMnN showing molecular N <sub>2</sub> . . . . .	98
6.16	SIMS sputtering yields for MnN . . . . .	100
6.17	XRD pattern of MnN . . . . .	100
6.18	EXAFS of MnN . . . . .	102
6.19	Fourier transform of EXAFS measurement on MnN . . . . .	102
7.1	Temperature dependent resistivity of GaMnN. . . . .	108
7.2	Check for variable range hopping in GaMnN with low Mn content. . . . .	109
7.3	Temperature-dependent resistivity of GaMnN with high Mn content. . . . .	110
7.4	Optical absorption of GaN and GaMnN. . . . .	112
7.5	Magnetisation of GaMnN with low Mn content. . . . .	113
7.6	Field-normalised ZFC magnetisation of GaMnN with low Mn content. . . . .	114
7.7	Field loops of GaMnN with high and low Mn contents. . . .	115
7.8	Brillouin function fitting to M-H dependence of GaMnN. . .	117
7.9	Magnetisation of GaMnNO. . . . .	122
7.10	Temperature-dependent DC resistivity of MnN . . . . .	124
7.11	Measured and calculated optical conductivity of MnN . . . .	125
7.12	N(2 <i>p</i> ) edge XANES and XES of MnN . . . . .	127
7.13	Mn(2 <i>p</i> ) edge XANES of MnN . . . . .	129
7.14	ZFC magnetisation of MnN . . . . .	129
7.15	Field-normalised ZFC magnetisation of MnN . . . . .	131
7.16	Field loop of MnN . . . . .	131
8.1	LSDA+U calculation of GdN band structure . . . . .	138
9.1	XRD pattern of GdN . . . . .	146
9.2	XRD pattern of SmN . . . . .	146
9.3	Raman spectra of rare earth nitrides . . . . .	148
9.4	Differential conductivity of GdN as a function of N <sub>2</sub> pressure	150
9.5	Temperature-dependent DC resistivity of GdN. . . . .	152

---

9.6	Test of activated behaviour of GdN resistivity. . . . .	152
9.7	Temperature-dependent DC resistivities of rare earth nitrides.	153
9.8	ZFC magnetisation of GdN. . . . .	154
9.9	Field loop of GdN. . . . .	155



# List of Tables

3.1	Structural parameters of GaN and MnN thin films. . . . .	38
4.1	Typical partial pressures of residual gases in the UHV chamber before and after growth of a 200 nm GaMnN film. . . . .	52
4.2	Typical metal evaporation rates and final compositions for GaMnN IAD film growths. . . . .	53
4.3	Metal evaporation rate and final composition for MnN IAD film growths. . . . .	53
6.1	Compositions and thicknesses of GaMnN films. . . . .	82
6.2	Fitted EXAFS parameters for GaMnN. . . . .	91
6.3	Fitted EXAFS parameters for MnN. . . . .	101
7.1	Curie-Weiss law fitting results for GaMnN. . . . .	116
8.1	Structural and magnetic properties of rare earth nitrides. . .	137
9.1	Compositions and thicknesses of rare earth nitride films. . .	145
9.2	Magnetic characterisation results for rare earth nitrides. . .	156





# Glossary

<b>ASA</b>	Atomic Sphere Approximation.
<b>CPA</b>	Coherent Potential Approximation.
<b>DMS</b>	Diluted Magnetic Semiconductor.
<b>DOS</b>	Density of States.
<b>EPR</b>	Electron Paramagnetic Resonance.
<b>ESR</b>	Electron Spin Resonance.
<b>EXAFS</b>	Extended X-ray Absorption Fine Structure.
<b>FC</b>	Field Cooled.
<b>fcc</b>	face-centered cubic.
<b>fct</b>	face-centered tetragonal.
<b>FIB</b>	Focussed Ion Beam.
<b>FLAPW</b>	Fully Linear Augmented Plane Wave.
<b>FP-LMTO</b>	Full Potential Linear Muffin-Tin Orbital.
<b>FTIR</b>	Fourier Transform Infra-red.
<b>IAD</b>	Ion-Assisted Deposition.
<b>IBA</b>	Ion Beam Analysis.
<b>IR</b>	Infra-red.

<b>KK</b>	Kramers-Kronig.
<b>LDA</b>	Local Density Approximation.
<b>LMTO</b>	Linear Muffin-Tin Orbital.
<b>LSDA</b>	Local Spin-Density Approximation.
<b>MBE</b>	Molecular Beam Epitaxy.
<b>MCS</b>	Monte Carlo Simulation.
<b>MFA</b>	Mean Field Approximation.
<b>MOCVD</b>	Metal Organic Chemical Vapour Deposition.
<b>NRA</b>	Nuclear Reaction Analysis.
<b>PDOS</b>	Partial Density of States.
<b>PIXE</b>	Particle Induced X-ray Emission.
<b>PLD</b>	Pulsed Laser Deposition.
<b>pseudo-rdf</b>	pseudo-radial distribution function.
<b>RBS</b>	Rutherford Backscattering Spectroscopy.
<b>RE</b>	Rare Earth.
<b>REN</b>	Rare Earth Nitride.
<b>RGA</b>	Residual Gas Analyser.
<b>RKKY</b>	Rudermann-Kittel-Kasuya-Yosida.
<b>SAED</b>	Selected Area Electron Diffraction.
<b>SE</b>	Spectroscopic Ellipsometry.
<b>SIC</b>	Self-Interaction Correction.
<b>SIMS</b>	Secondary Ion Mass Spectroscopy.

---

<b>SQUID</b>	Superconducting Quantum Interference Device.
<b>SXRD</b>	Synchrotron X-ray Diffraction.
<b>TEM</b>	Transmission Electron Microscopy.
<b>UHV</b>	Ultra-High Vacuum.
<b>UV</b>	Ultra-Violet.
<b>VRH</b>	Variable-Range Hopping.
<b>XANES</b>	X-ray Absorption Near Edge Structure.
<b>XAS</b>	X-ray Absorption Spectroscopy.
<b>XES</b>	X-ray Emission Spectroscopy.
<b>XRD</b>	X-ray Diffraction.
<b>XTEM</b>	Cross-sectional Transmission Electron Microscopy.
<b>ZFC</b>	Zero-Field Cooled.



# Chapter 1

## Introduction

The properties of both magnetic and semiconducting materials have been exploited for decades to develop the large and important solid-state electronics industry. In recent years, attention has turned to find materials suitable for the manufacture of devices that exploit both electronic charge and spin degrees of freedom *simultaneously*. Through the simultaneous manipulation of electronic charge and spin, this field of spin electronics, or spintronics [1], promises devices that operate at higher speeds, reduced power consumption and have greater functionalities than possible with conventional devices. Research on several different spintronic devices has already been published in the literature such as the spin diode, the spin filter and the spin transistor [1]. One of the most promising avenues into developing spintronics devices is finding materials that combine both magnetic and semiconducting properties into one, and crucial to their successful commercial application are materials that retain useful magnetic properties above room temperature. Currently, research into finding suitable materials is approached in two main ways. Existing semiconductors can be doped with a proportion of one or more magnetic elements to induce magnetic behaviour in them, and these materials are known as diluted magnetic semiconductors (DMS). The other way is to find materials with both intrinsic semiconducting and magnetic properties, and one potential such group are the rare earth nitrides (RENs). This study investigates materials from both of these two categories.

DMS have been researched since at least the 1960s, and materials based

on II-VI compounds such as CdMnTe and ZnMnSe have been extensively studied [2]. In more recent years, interest has been renewed due to the quest for materials that are ferromagnetic above room temperature [3]. III-V semiconductors are in widespread use in the opto-electronics industry, and the introduction of magnetic elements into materials such as GaAs or GaN to make them magnetic would allow the required additional control over the spin degree of freedom [4].

$\text{Ga}_{1-x}\text{Mn}_x\text{As}$  with  $x = 5.3\%$  was shown to be ferromagnetic with a  $T_C$  of 110 K in 1998 [4], and the maximum yet achieved  $T_C$  is  $\sim 159$  K with  $x = 6.7\%$  [5]. The magnetic behaviour of GaMnAs is well described by a Ruderman-Kittel-Kasuya-Yosida (RKKY) or Zener model of ferromagnetism between localised spins mediated by delocalised carriers [6]. Mn doped into III-V semiconductors such as GaAs is in principle a source of holes if it substitutes for Ga atoms. This provides the source of the carriers required for the RKKY mechanism, although Mn incorporated at other sites (e.g. interstitial, substitution for N atoms) may have a different effect. Using the RKKY model applied to a number of other II-VI and III-V semiconductors, a prediction was made using a mean field approximation that ZnO and GaN doped with  $x = 5\%$  Mn and  $3.5 \times 10^{20}$  holes per  $\text{cm}^3$  would have  $T_C$  in excess of 300 K [3]. Reports on GaN with transition metal dopants including Mn added up to a few % are widespread in the literature, however the physical properties of these materials vary greatly, and a solid understanding of the physical principles involved is still lacking. One of the key issues is separating the observed effects of possible Mn-rich phases that may occur in GaMnN from the properties of the GaMnN material itself.

The rare earth (RE) elements have proven their usefulness for many magnetic and optical applications. In particular, they are a source of sharp luminescent lines when doped into semiconductors like GaN [7, 8] and show promise for the production of Si-based lasers [9]. The magnetic properties of the REs have also been used to make strong magnets, and some of these are in widespread commercial use. When existing RE alloys are compounded with N, materials with enhanced magnetic properties can be created [10]. The RENs retain the useful magnetism originating

from the spin polarisation of the partially filled RE  $4f$  electronic valence shell whilst significantly altering the band structure near the Fermi level. New band structure calculation techniques have recently been applied to the RENs, which are rich testing grounds for investigating the effects of strong electron correlations. These investigations have predicted that the RENs should exhibit a wide variety of electronic and magnetic properties, and a number may be intrinsic ferromagnetic semiconductors or half-metals [11]. Ferromagnetic semiconductors allow for both magnetic and semiconducting properties to be exploited simultaneously in one material, and half metals have a non-zero density of states at the Fermi level for one spin orientation only, thus both are promising candidates for spintronics material development. Experimental investigations into the real materials are highly desirable as such reports are scarce to date, and there is little certainty about their potentially useful properties. Additionally, recent experimental studies on RE-doped wide-bandgap semiconductors GaN [12–19], ZnO [20] and AlN [16] have reported ferromagnetic behaviour at room temperature, and there is an indication that ferromagnetic ordering of Gd-doped GaN may be possible through  $n$ -type carriers [21]. Determining the method of magnetic coupling in the RENs may illuminate the potential uses of RE metals in encouraging ferromagnetism in semiconductors.

In this study thin films of GaMnN with a range of Mn contents and a number of different RENs have been grown and investigated with a wide and complementary number of techniques for probing structure, electronic, optical and magnetic properties. Also investigated is the end member for the Ga-Mn-N sequence and a possible impurity phase: MnN. Chapter 2 sets out the basic theories of magnetism and conduction in disordered materials applied to the materials covered in this work. Chapter 3 is a review of the theoretical development and experimental reports of both GaMnN in the wurtzite phase and of MnN. Chapter 4 reports the procedures used to grow the GaMnN, MnN and REN thin films investigated in this study. Chapter 5 describes the mostly experimental techniques applied in determining the properties of these materials. Chapter 6 presents the results of the investigations into the composition and structure of GaMnN and MnN. Chapter 7 analyses the conduction, optical and

magnetic characteristics of GaMnN and MnN. The MnN results, including x-ray absorption and emission measurements, are interpreted using band structure calculations of the electronic density of states (DOS). Chapter 8 is a review of the existing literature reports on the RENs and Chapter 9 presents the results of the investigations into the structure, electronic and magnetic properties of a number of the RENs.







## Chapter 2

# Magnetism basics and electrical conduction in disordered materials

Before discussing the results of investigations into the properties of the thin films of interest in this study, it is important to introduce basic concepts of magnetism and conduction in disordered materials. The relations that describe magnetism and electrical conduction in this chapter will be applied to analyse the properties of the GaMnN, MnN and REN thin films in Chapters 7 and 9. For a more complete introduction to magnetism see Refs. [22–25], for a treatment of the quantum theory of magnetism see Ref. [26], and the conduction of disordered materials is covered in more detail in Ref. [27] and Chapter 5 of Ref. [28]. Terminology that is used in this thesis will also be introduced and defined in this chapter.

### 2.0.1 Terminology

The published literature on magnetism and magnetic characteristics of materials reports quantities in a mix of CGS and SI units, and as a consequence it is useful at this point to clarify the uses of several words or phrases used in this thesis. Throughout this thesis the results of magnetic analyses have been reported exclusively in SI units. The words *spin* or *spin moment* are used to refer to the (spin) magnetic moment of individ-

ual electrons in a material. The total magnetic moment of an electron in an unfilled valence shell includes the sum of the spin and orbital components of angular momentum, and this sum magnetic moment is referred to as *moment*. The value of the moment of a magnetic atom (i.e. an atom with net angular momentum) is the sum of the moments from unpaired electrons, and is reported in units of SI Bohr magnetons  $\mu_B = 9.2741 \times 10^{-24} \text{ JT}^{-1} (\equiv \text{Am}^2)$ . Both orbital and spin contributions to the moments of the electrons are taken into account to find the total moment of a magnetic atom, with the application of Hund's rules to find this total in the ground state. The magnetic response of a large collection of electrons, a material or thin film as a whole is referred to as the *magnetisation* of that material, and this is the moment per unit volume for that material. The SI unit of the magnetisation is in units of  $\text{Am}^{-1}$ .

### 2.1 Magnetism

The most natural way to characterise the magnetism of a material is with its response to an applied magnetic field. A magnetic field will induce a vector magnetisation  $\mathbf{M}$  in the material, and the relation between the two is the susceptibility  $\chi$

$$\mathbf{M} = \chi \mathbf{H}_0. \quad (2.1)$$

In general  $\chi$  is temperature  $T$  and magnetic field intensity  $\mathbf{H}_0$  dependent, and tells us about the state of magnetic ordering in the material.  $\mathbf{H}_0$  shall be assumed to be directed along one axis, and can therefore be represented by the scalar  $H$ . In general  $\chi$  is a tensor, and  $\mathbf{M}$  is not simply directed along one axis even where  $H$  is. For simplicity,  $\mathbf{M}$  will be represented as a scalar  $M$  corresponding to the component of  $\mathbf{M}$  in the direction of  $H$ . Similarly,  $\chi$  will be considered as a scalar resulting from the diagonal component equivalent to  $M/H$ . Note that Eq. 2.1 assumes that a magnetic field must be applied for a magnetisation to be present. However, many materials exist that have a spontaneous magnetisation with zero applied field, and in this situation Eq. 2.1 is invalid. With non-zero fields applied to such

materials, Eq. 2.1 is still applicable, although it must be noted that the net magnetisation of this type of material is not exclusively dependent on the instantaneous applied field according to Eq. 2.1, but also on the history of that field, as discussed below.

A small, negative, temperature-independent  $\chi$  is a sign of *diamagnetism*. Values of  $\chi$  for diamagnetic materials are typically  $\sim 10^{-5}$ , and are a consequence of Lenz's law for moving electric charges in a magnetic field. Materials that are diamagnetic are those with full electronic valence shells. All materials have a contribution to  $\chi$  from diamagnetism, but usually the magnetic response is dominated by other contributions to  $\chi$  except in the cases where all states in occupied electronic shells are full.

In materials with at least one partially filled electronic valence shell where the electrons do not interact with each other, *paramagnetism* is observed. In this case, the moments of unpaired electrons within the partially filled valence shells align with the magnetic field, yielding a positive  $\chi$  that is usually of the order of  $10^{-2}$  at room temperature, and varies with  $1/T$ . The temperature dependence of paramagnetic materials arises from the competing effects of the tendency towards alignment of the moments in a field and the effect of thermal fluctuations towards randomising the directions of the individual moments.

The ground state magnetisation of a collection of non-interacting moments as a function of temperature and magnetic field strength is

$$M = N \frac{\sum_{-J}^{+J} M_J g \mu_B e^{M_J g \mu_B H / k_B T}}{\sum_{-J}^{+J} e^{M_J g \mu_B H / k_B T}}, \quad (2.2)$$

where  $N$  is the number of magnetic atoms,  $J$  is the total electronic angular momentum,  $M_J$  can take values of  $(J, J-1, J-2 \dots -J+2, -J+1, -J)$ ,  $g$  is the Landé ( $g$ -factor  $g = 1 + \frac{J(J+1) + S(S+1) - L(L+1)}{2J(J+1)}$ ) and  $k_B$  is Boltzmann's constant ( $= 1.38 \times 10^{-23} \text{ JK}^{-1}$ ). Where the field strength term is small compared with the thermal energy, Eq. 2.2 can be reduced to

$$M = \frac{1}{3} N \frac{g^2 J(J+1) \mu_B^2 H}{k_B T}. \quad (2.3)$$

## 20 Magnetism basics and electrical conduction in disordered materials

Comparing Eq. 2.3 with Eq. 2.1, the temperature dependence of the molar susceptibility  $\chi_m$  for a collection of paramagnetic (non-interacting) moments is derived as

$$\chi_m = \frac{1}{3} N_A \frac{\mu_B^2 p_{\text{eff}}^2}{k_B T}, \quad (2.4)$$

where  $N_A$  is Avogadro's number and  $p_{\text{eff}} (= \sqrt{g^2 J(J+1)})$  is the effective Bohr magneton number. This is equivalent to Curie's law, where a plot of  $1/\chi_m$  versus  $T$  at high enough temperatures should yield a straight line which intercepts the  $T$  axis at 0 K.

Equation 2.4 is derived assuming that  $g\mu_B H/k_B T \ll 1$ , i.e. that the applied magnetic field is small compared with the thermal energy  $k_B T$ . At low temperatures and/or larger fields, Curie's law is not valid. The dependence of the magnetisation on field strength and temperature must be derived from Eq. 2.2 without the above assumption. The result is

$$M = Ng\mu_B J B_J(y), \quad (2.5)$$

where

$$y = \frac{Jg\mu_B H}{k_B T}.$$

The function  $B_J(y)$  is the Brillouin function and is described by

$$B_J(y) = \frac{2J+1}{2J} \coth\left(\frac{2J+1}{2J}y\right) - \frac{1}{2J} \coth \frac{y}{2J}, \quad (2.6)$$

and in the limit of classical free particles where  $J \rightarrow \infty$ ,

$$B_J(y) = \coth y - \frac{1}{y} = L(y), \quad (2.7)$$

where  $L(y)$  is known as the Langevin function.

Many materials show a spontaneous magnetisation at low temperatures, without the presence of a magnetic field to align the moments. In these materials the magnetic atoms interact with each other to align their

moments. The presence of a spontaneous magnetisation at low enough temperatures is *ferromagnetism*. At low enough temperatures all the moments in a ferromagnetic material align, and the magnetic response is as large as it can get, or is said to be saturated. Saturation can also be reached at higher temperatures with large enough applied fields. The temperature below which the spontaneous magnetisation is non-zero is known as the Curie temperature  $T_C$ . At temperatures lower than  $T_C$ , the thermal randomisation of the moment directions becomes weak enough that interactions between the magnetic ions begin to align their moments.

The spontaneous magnetisation in a ferromagnetic material at temperatures below  $T_C$  may be understood in relation to the magnetic history of that material. When an initially unmagnetised ferromagnetic material is exposed to a small applied field a magnetisation is induced in accordance with Eq. 2.1 (path O-A in Fig. 2.1.). This magnetisation is reversible until a critical applied field strength is reached (point B). After such a critical field is applied, returning the field to zero will leave the ferromagnet with a remanent magnetisation ( $M_r$ ) in the direction of the historically applied field. A coercive field ( $H_C$ ) needs to be applied in the opposite direction to this remanent magnetisation in order to return the magnetic response to zero (E). At large enough applied fields, the magnetisation reaches a maximum ( $M_s$ , points C and F), and increasing the field strength does not increase the magnetisation of the material any further. This phenomenon is known as saturation of the magnetic response, when all the moments are aligned in the direction of the field. Cycling the field from large positive values to large negative values results in the magnetisation of the ferromagnetic material plotting out a hysteresis loop, with a remanent magnetisation at zero applied field (points D and G) dependent on the history of the applied field and saturation values reached at high enough fields. Figure 2.1 is a diagram of a field loop for a ferromagnet at temperatures below  $T_C$ , with remanent magnetisation, hysteresis and saturation inherent.

The origin of the hysteresis present in field loops of ferromagnets is explained due to the presence of magnetically aligned domains within the ferromagnet. A ferromagnet below  $T_C$  with a zero net magnetisation does not have a random alignment of individual moments. Due to the cooper-

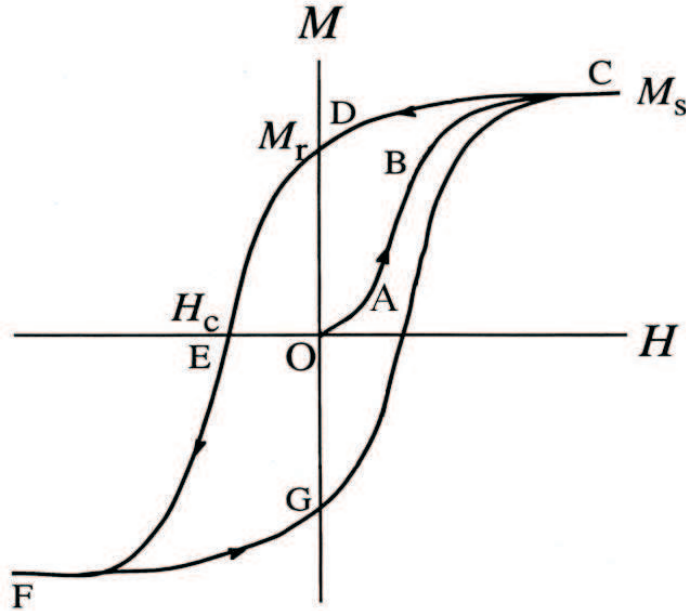


Figure 2.1: Typical field loop for a ferromagnet below  $T_C$ , showing a hysteresis [29]. Remanent magnetisation ( $M_r$ ), coercive field ( $H_c$ ) and saturation magnetisation ( $M_s$ ) are labelled.

ative mechanism operating between the moments, collections of moments are aligned in the same sense and said to form a *domain*. The domains are themselves oriented such that the sum of their net magnetisations is zero in zero applied field. The cost in energy associated with the loss of moment alignment in the grain boundaries is more than offset by the decrease in magnetic dipolar energy of the domains in the effective field of their neighbours. Under small applied fields, the domains begin to align, yielding the steep increase in magnetisation of the material at these fields. Once all the domains are aligned, the saturation magnetisation has been reached, and larger field strengths can no longer continue to increase the net magnetisation. Upon reducing the applied magnetic field, the domain alignment relaxes somewhat, but there remains a net alignment in the direction of the historically applied field, and as a result there is a remanent



magnetisation. The coercive field is the field strength necessary to rotate enough of the domains to point in the opposite direction to the original field such that the net magnetisation is once again zero.

Theoretically predicted before it was experimentally confirmed, another type of cooperative magnetic ordering is possible. *Antiferromagnetism* occurs where the magnetically interacting ions in a material can be subdivided into two lattices that are magnetically aligned in the opposite direction to each other. This results in a zero net magnetisation due to the sum of the magnetisations from each sublattice cancelling to zero. If the total magnetisation of the two sublattices is not the same, the ordered state results in a net magnetisation due to the difference between the two sublattice magnetisations. This is known as *ferrimagnetism*, which can be considered as a special case of antiferromagnetism and will not be further discussed here. As in the case for ferromagnetism, there is a temperature below which the ordered state exists, which is known as the Neel temperature  $T_N$ .

The susceptibility dependence on temperature for both antiferromagnets and ferromagnets above their respective ordering temperatures has the same form. For moments that interact, the Curie law for paramagnets still applies above the ordering temperature for the material where the magnetic field is not too large, but now the denominator must be modified to include an apparent Curie temperature  $\theta_p$ . Now the law (known as the Curie-Weiss law) is

$$\chi_m = \frac{1}{3} N_A \frac{\mu_B^2 p_{\text{eff}}^2}{k_B (T - \theta_p)}. \quad (2.8)$$

This relation emerges when simplifying the interactions between moments as a mean field that each individual moment interacts with. The apparent Curie temperature results from the extrapolation of the inverse of the high temperature susceptibility to zero and is in general not identical to the  $T_C$  or  $T_N$  in a material. It can however be useful, as in the case of ferromagnetic exchange interactions  $\theta_p \approx T_C$ . A negative value of  $\theta_p$  generally indicates antiferromagnetism, although not all antiferromagnets have  $\theta_p < 0$ .

### 2.1.1 Exchange energy

The interactions between moments in ferromagnetic or antiferromagnetic materials are described by *exchange energy*. The origin of this can be illustrated by considering the total energy of a system of two electrons in a potential from a positive ion core. The Hamiltonian describing the energy of this system of two electrons at  $\mathbf{r}_1$  and  $\mathbf{r}_2$  in the ion potential is

$$\mathcal{H} = \mathcal{H}_0(\mathbf{r}_1) + \mathcal{H}_0(\mathbf{r}_2) + \frac{e^2}{|\mathbf{r}_1 - \mathbf{r}_2|}, \quad (2.9)$$

where  $\mathcal{H}_0$  is the one-electron Hamiltonian and  $e$  is the electronic charge. Note that the electron spin states must be considered in the wavefunctions. If the electron-electron interaction energy is assumed to be small compared with  $\mathcal{H}_0$ , then this addition to the Hamiltonian can be treated with perturbation theory. It is also necessary to include the constraint on the wavefunctions imposed by the Pauli exclusion principle, that since fermions such as electrons are indistinguishable, *the wavefunctions must be antisymmetric if their positions and spin states are exchanged*. Two distinct energy levels are possible from this system, a singlet state (spins antiparallel) and a triplet state (spins parallel), and the difference in energy between the two is dependent on the exchange energy of the two electrons in sites  $i$  and  $j$ ,  $J_{ij}$ . Dirac showed that in the case of localised electrons occupying orthogonal orbital states, the Pauli principle could be included into the Hamiltonian of Eq. 2.9 by adding a term

$$\sum_{i < j} -J_{ij} \left[ \frac{1}{2} + 2\mathcal{S}_i \cdot \mathcal{S}_j \right], \quad (2.10)$$

where  $i$  and  $j$  denote the sites of the two electrons involved and  $\mathcal{S}_i, \mathcal{S}_j$  are the spin states of the two electrons. The exchange integral  $J_{ij}$  is the interaction of the charge distributions for the two electrons with each other. From this, the spin-dependent energy contributions to the Hamiltonian as a result of the Pauli principle can be represented as

$$\mathcal{H} = -2 \sum_{i < j} J_{ij} \mathbf{S}_i \cdot \mathbf{S}_j, \quad (2.11)$$

which is known as the Heisenberg Hamiltonian. The sign of  $J_{ij}$  determines whether parallel (ferromagnetic) or antiparallel (antiferromagnetic) arrangement of the spins is the lowest energy state for the system.

Although the exchange energy  $J_{ij}$  is derived in this way from a simplified picture of nearest neighbour wavefunction overlap between two electrons in the potential from a positive ion core, this concept is a useful starting point for determining the effects of charge distributions overlapping in larger numbers and at larger distances.

## 2.2 Conduction in disordered materials

### 2.2.1 Variable Range Hopping (VRH)

In crystalline homogeneous semiconductors, at high enough temperatures conduction is dominated by thermal activation of carriers from occupied valence band states or from defect states in the bandgap to the conduction band. The conductivity of these semiconductors obeys an exponential relation

$$\sigma \sim e^{-E_A/k_B T} \quad (2.12)$$

where  $E_A$  is the activation energy of the defect or valence band state. Carriers in a semiconductor will also experience a decrease of relaxation time as temperature is increased, and therefore the same decrease of conductivity with temperature as seen in metals will occur. However, at most temperatures of interest, the increase of carrier concentration due to thermal activation is the dominant effect.

Classically, the more disorder there is in a system, the smaller the mean free path of carriers, due to the higher concentration of defects that lead to scattering events. The defects will also add localised states to the set of

possible energy levels of the material. If the localised states pin the Fermi level deep enough in the bandgap that  $E_A$  is too great for activated conduction to be significant, a new conduction mechanism can occur: thermally activated hopping between the localised impurity states. There is a smaller probability of hopping between localised states that are more distant from each other, but at larger distances there is a higher probability of states being available at closer energies. The competition of these two effects leads to thermally-assisted hopping conductivity

$$\sigma \sim e^{-(\frac{T_0}{T})^{\frac{1}{4}}}, \quad (2.13)$$

where  $T_0$  is the Mott temperature, which is defined in terms of the density of states and decay length of wavefunctions for localised states. The dependence on  $T^{\frac{1}{4}}$  is for three-dimensional hopping, and variable range hopping (VRH) in two dimensions or one may be observed, in which case the factor is modified to  $e^{-(\frac{T_0}{T})^{\frac{1}{3}}}$  or  $e^{-(\frac{T_0}{T})^{\frac{1}{2}}}$  in each respective case.

### 2.2.2 Weak localisation

Disorder in a metal similarly requires a correction to the usual models of electronic conduction. Below is a brief description of the origin of this correction.

In the Drude model, electron-electron interactions are disregarded, and charge carriers experience elastic collisions with the massive positively charged ions with an average time between collisions  $\tau$  (relaxation time). Although electron-ion collisions are a physically incorrect picture of the origin of resistance in a material, this model provides a useful mathematical relation for the conductivity in a metal. The conductivity at finite temperatures resulting from finite relaxation time ( $\tau$  increases at lower temperatures) is

$$\sigma = \frac{ne^2\tau}{m}, \quad (2.14)$$

where  $n$  is the number density of charge carriers and  $m$  is the electronic mass. The semiclassical model of conduction treats the effect of the ions as a perfectly periodic potential in which the charge carriers are contained. In this model, the decreasing conductivity (and therefore decreasing  $\tau$ ) at higher temperatures is more realistically considered to be due to thermal vibrations (phonon modes) of the ion lattice, which violates the periodicity of the potential, rather than charge carrier collisions with the ions themselves. At low temperatures where thermal vibrations are suppressed, most metals have a conductivity limited by scattering from impurities or defects in the lattice structure.

The classical conductivity of a disordered metal has to be corrected for the effect of quantum interference of differing paths of propagation within a material. Quantum mechanically, conduction has to be considered as due to the total probability that a carrier travels from point A to point B. Between any two such points in a material there exist multiple trajectories that charge carriers can follow. The probability amplitude of a carrier arriving at B then is the sum of the probabilities of the multiple different trajectories from A to B. The phase of each trajectory needs to be accounted for in this sum, and in general both constructive and destructive interference affects the probability amplitude sum. The reason for this is that different trajectories contain different numbers of impurities and defects, and thus different numbers of scattering events (when considered in the classical analogue), which alters the relative phases of each trajectory. However, consider a particular trajectory from A back to A. Time reversal invariance informs us that traversing this path in either direction yields the same amplitude and phase, so the two possible trajectories always provide constructive interference, and thus the A-A probability amplitude is larger than for any other path. This leads to a smaller negative quantum interference correction to the classical conductivity for return trajectories than for any other possible trajectory. Hence, the increased scattering impurity concentration in a metal acts to enhance localisation of charge carriers through increasing the probability of return trajectories. This correction to the conductivity is known as weak localisation. As temperature is increased, the phase-destructive scattering events

become more frequent, resulting in a temperature dependence of the correction to the metallic conductivity. The effect of this results in an *overall* temperature dependence for the conductivity given by

$$\sigma \sim \ln T. \quad (2.15)$$

The weak localisation correction to the metallic conductivity has additional competing effects due to electron-electron interactions and spin-orbit scattering not taken into account in the above equation. These extra corrections are treated in Chapter 5 of Ref. [28], and for this study the brief overview presented is sufficient to allow an analysis of the results included here using Eq. 2.15.

The net result of the quantum interference on transport in a disordered metal is to increase the resistivity. This consideration becomes important for the nanocrystalline GaMnN films with very high Mn contents.







# Chapter 3

## GaMnN and MnN

### 3.1 GaMnN

#### 3.1.1 Theory

Since the original Dietl [3] prediction of room temperature ferromagnetism in GaMnN, further theoretical development of the understanding of magnetism in GaMnN and other III-V DMS has been sought using a variety of different approaches. It should be noted that though this prediction was made for both zincblende and wurtzite phase GaMnN, this review deals predominantly with research done on material in the wurtzite structure. In one method, a supercell in the wurtzite GaN lattice structure with between four and 108 atoms is theoretically constructed including two or more Mn atoms, and the electronic band structure calculated [30–40]. The effects of exchange and electron correlations are taken into account using the local spin-density approximation (LSDA) [32, 38, 40], self-interaction corrections (SIC) [36, 37] or with a Hubbard potential  $U$  applied [30, 33, 38, 40]. The total energies are calculated with the Mn spins arranged in each of the parallel, antiparallel and disordered alignment states. The total energy difference between these cases is used to predict which state is stable; ferromagnetic (parallel alignment), antiferromagnetic (antiparallel) or spin-glass/paramagnetic (disordered) [39, 41, 42]. Where the ferromagnetic state is the lowest in energy, the ferromagnetic stabilisation energy can be compared to that calculated for the better understood GaMnAs. From

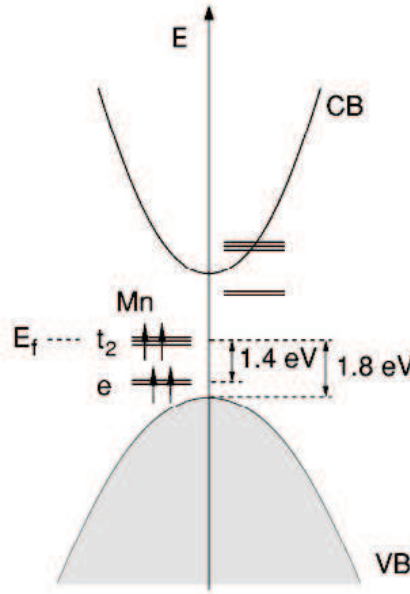


Figure 3.1: Positions of the Mn 3d-related energy levels within the bandgap of GaN (from Ref. [43]). The band structure is split into spin up (left hand side) and spin down (right hand side).

this comparison, inferences can be made about whether  $T_C$  for GaMnN is higher or lower than in GaMnAs [32, 38].

Figure 3.1 shows the the position of the Mn 3d energy levels in the band structure of GaMnN. These positions were found from a LSDA calculation for GaMnN with Mn substituting on the Ga lattice sites, from Popovic *et. al* [43]. The scheme for the position of the Mn states is typical of the band structure calculations performed that assume substitutional Mn incorporation on the cation Ga sites. The Mn 3d levels are split by the exchange interaction into spin up states and spin down states. The effect of the tetrahedral crystal field is to split the states further into a doublet of  $e_g$  symmetry and a triplet of  $t_{2g}$  symmetry for each spin orientation. The  $e_g$  states lie at lower energies than the  $t_{2g}$  states of the same spin. The precise energy separations between these states are dependent on the occupation of the 3d states, but for Mn in the 3+ (four 3d electrons) or 2+ (five 3d electrons) oxidation states the exchange splitting dominates, and the five spin up states are at lower energies than the spin down states, and are located within the

GaN bandgap. As a consequence of the strong exchange splitting of the Mn 3*d* states, a key parameter is the location of the Fermi level in GaMnN, as this will determine the oxidation state of the incorporated Mn. The Mn oxidation state in turn determines the value of the local Mn moments, and influences the value and sign of the inter-ionic exchange interaction between neighbouring Mn ion moments. Understanding this is crucial in determining the state and origin of magnetic ordering in GaMnN.

From the calculated band structures, some studies have investigated the hybridisation between the Mn 3*d* and N 2*p* levels, and also examined the precise location of the Mn-related bands in the GaN bandgap [35–37]. In most cases these studies derive from the assumption that the Mn is in certain fixed positions within the supercell used for the calculation. The coherent potential approximation (CPA) method allows for configurational averaging and band structure calculations with the CPA have also been applied to GaMnN [41, 44] to account for the effects of structural disorder. Some groups have gone further by mapping the energy of the calculated band structure from the supercell or CPA methods on to a Heisenberg Hamiltonian using the frozen-magnon technique [33] to determine the effective exchange energies. From there  $T_C$  was found within a mean field approximation (MFA) [31, 33, 34] or with the aid of Monte Carlo simulations (MCS) [44–46].

Many of these calculations [33, 47] of the band structure and magnetic ordering agree with the original MFA-based Dietl prediction that hole-doped GaMnN should exhibit ferromagnetism above room temperature. In GaMnAs where Mn is a shallow acceptor and hole states are created in the valence band at finite temperatures, the MFA-based predictions have been experimentally verified, showing this is the mechanism of ferromagnetic ordering. The Mn ion moments interact antiferromagnetically with these delocalised holes, and therefore the Mn moments are indirectly ferromagnetically aligned, mediated by the coupling to the holes. However, as seen in the sketch of the dopant energy levels in Figure 3.1, in GaN the Mn 3*d* states are introduced much deeper into the bandgap than in GaAs. Figure 3.2 shows the spin-resolved density of states derived from a typical band structure calculation for GaMnN, and it is clear that the Mn 3*d* states

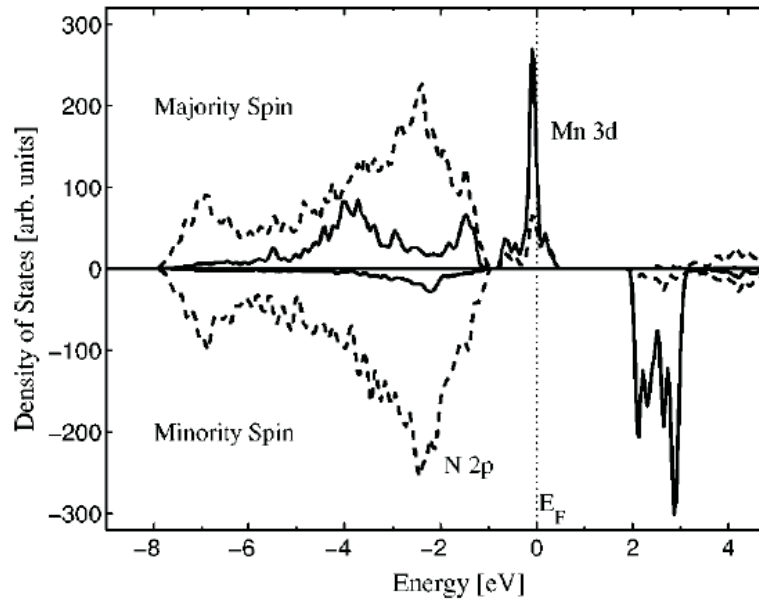


Figure 3.2: Spin-resolved density of states for  $\text{Ga}_{0.937}\text{Mn}_{0.063}\text{N}$  in the wurtzite structure resolved into Mn 3d (solid lines) and N 2p (dashed lines) states (from [35]). Note the position of the majority spin Mn band at the Fermi level ( $E_F$ ) deep within the GaN bandgap.

form a narrow band far from either the valence or conduction band edges.

The Fermi level in GaMnN without additional dopants lies inside the majority spin Mn band in the GaN bandgap, and so a non-zero spin moment giving rise to exchange is expected for the Mn. However, the exchange energies are calculated as being of a similar magnitude to those in GaMnAs, which casts doubt on the prediction that single-phase GaMnN has a higher  $T_C$  than GaMnAs. Moreover, the exchange is short-ranged [31, 38, 40, 44, 45], further weakening the possibility of long-range ordering in low Mn-doped GaMnN occurring through hole-mediation. As discussed above, the position of the Fermi level in relation to the Mn 3d states is of great importance in determining the strength and overall character of the magnetism, and doping with either electrons or holes can destroy the ferromagnetism [48]. Some studies have considered the deep acceptor nature of the substitutional Mn to completely rule out the possibility of hole-mediated magnetism, as there will be a negligible number of

holes thermally excited in the valence band at room temperature [37, 40]. Instead, ferromagnetism should only occur at higher Mn concentrations when the percolation threshold is reached [44, 45] and the original MFA model predictions have been concluded to significantly overestimate  $T_C$  for GaMnN [46]. A discussion of electron-mediated exchange has found it feasible, but weak unless symmetry around the Mn is lowered [49], and this is unlikely for GaN in either of its crystalline forms. An alternative explanation of the ferromagnetism favoured by some groups [31, 37, 38, 40] is due to double exchange involving electrons in the Mn states. These electrons are not itinerant as in the case of the carrier-mediated mechanism, but are delocalised enough to hop between adjacent Mn ions in different oxidation states. This hopping leads to a lowering of the total energy state for spin alignment of the two Mn ions over the case where these Mn ions have their spin moments anti-aligned, favouring ferromagnetism [50]. As this relies only on Mn-Mn interactions through unoccupied levels in the Mn  $3d$  states, there is no requirement for valence band holes as in the carrier-mediated models. Instead, this model depends heavily on the position of the Fermi level, and if all Mn ions are in the  $2+$  state the majority spin Mn  $3d$  levels are filled and ferromagnetism through double exchange cannot occur [32, 51]. The nature of the short range exchange interaction requires higher doping levels of Mn for ferromagnetism through the double exchange mechanism than in other models, although room temperature  $T_C$  in  $\text{Ga}_{1-x}\text{Mn}_x\text{N}$  has been predicted with as low as  $x = 0.02$ .

Another alternative to the itinerant carrier-mediated model considers ferromagnetism in the case that the carriers are more localised than in the RKKY mechanism. In this model, the Mn ions interact with carriers to form a bound magnetic polaron with a large number of spin-polarised hole carriers, and at large enough concentrations of Mn the polarons intersect and align over macroscopic volumes [52].

Finally, fuelled by observations of clustering and alternate phases in GaMnN, others have treated theoretically the possibility of such phases contributing to the magnetism in GaMnN.  $\text{Mn}_x\text{N}_y$  clusters are calculated to have large localised magnetic moments that align ferromagnetically and are energetically favoured to form in GaN [53], so may be the source of the

high  $T_C$  seen in many preparations. The band structure of GaMnN with interstitial Mn has been calculated and compared with the case of substitutional Mn [43]. The effects of Mn clustering on  $T_C$  have also been investigated [34], and some consider the presence of metallic phases important to supply the carriers necessary for RKKY ferromagnetism in GaMnN [54], or that the magnetic behaviour of GaMnN is entirely due to these precipitates [55, 56].

### 3.1.2 GaMnN preparation and structure

Since the Dietl prediction GaMnN has been grown using many different techniques and investigated extensively. The earliest GaMnN [57] reported was in the form of small crystals grown using resublimation of a mixture of Mn and GaN powders [58]. The GaN powder was grown from the reaction of Ga vapour with  $\text{NH}_3$  [59]. GaMnN reported in the literature, in addition to the single crystal form, has had the form of microcrystalline grains [60, 61], nanowires [62–66] or crystalline thin films. Thin films of GaMnN have been prepared through molecular-beam epitaxy (MBE) [55, 67–83] with a wide spread of substrate temperatures, deposition and annealing of a Mn-layer onto a GaN film [84, 85], nebulised spray pyrolysis [86], metal organic chemical vapour deposition (MOCVD) [87, 88], pulsed laser deposition (PLD) [89],  $\text{Mn}^+$  [66, 88, 90–96] or  $\text{Mn}^+$  and  $\text{N}^+$  [97] ion implantation into already-prepared GaN films. GaMnN has also been grown co-doped with a number of different elements [54, 82, 98–106].

Most of these types of growth are well established as effective methods of preparing highly crystalline thin films with low concentrations of unintentional dopants, although their application to DMS like GaMnN is not as straightforward. From studies done on doping magnetic ions into other III-V semiconductor materials, the solubility limit of Mn in GaN was expected to be much lower than the  $\sim 5\%$  necessary for achievement of high temperature ferromagnetism [107]. The growth techniques mentioned have been successfully utilised to incorporate Mn randomly in the GaN lattice at much greater concentrations than the equilibrium state, al-

though there are still limits to the Mn content able to be incorporated.  $\text{Ga}_{1-x}\text{Mn}_x\text{N}$  with Mn concentrations of  $x = 0.01\text{--}0.05$  are commonly achieved using these growth methods, although the high mobility of the dopant at the temperatures involved often results in precipitations such as Mn clusters [108],  $\text{Ga}_x\text{Mn}_y$  [81, 88, 109–112],  $\text{Mn}_3\text{GaN}$  or  $\text{Mn}_4\text{N}$  [81, 88, 110, 112–117] or other  $\text{Mn}_x\text{N}_y$  phases [88, 97, 116]. A number of these phases are ferromagnetic at high temperatures [118], and it can be extremely difficult to separate the contributions of multiple phases from the optical and magnetic properties of a GaMnN film, especially where these phases are not all detected in typical structural analyses. The highest Mn-concentration single phase material reported was prepared by PLD and contains 26 at. % Mn [119], although samples grown with similar concentrations in the same study exhibited XRD peaks from alternate phases. Techniques for preparing material in a state even further from equilibrium, such as those involving low energy ions, have been suggested as potential methods of growing  $\text{Ga}_{1-x}\text{Mn}_x\text{N}$  with Mn concentrations above  $x \sim 0.05$  without the presence of alternate phases or precipitations [42, 94].

In this study GaMnN films have been grown using low energy N ions, in a process that has been previously used to successfully grow nanocrystalline and amorphous GaN thin films [120, 121]. The substrates were held at ambient ( $\sim 30^\circ\text{C}$ ) temperatures during film deposition, resulting in films in a state far from equilibrium. Growth at this temperature inhibits the mobility of the constituents once they impinge upon the substrate, allowing Mn to be incorporated randomly at concentrations far in excess of the normal range permitted by the methods mentioned above, which rely on substrate temperatures of  $250^\circ\text{C}$  and above.

Most GaMnN films reported have crystallised in the wurtzite GaN structure, which is the most stable at ambient temperatures and pressures [122]. The experimental investigations reviewed here concentrate on material in the wurtzite phase, although note that a number of reports exist on successful preparation of GaMnN in the zincblende phase [83, 123, 124]. The lattice spacings and ionic radius of Ga in wurtzite GaN are quoted in Table 3.1. Some transmission electron microscopy (TEM) and x-ray diffraction (XRD) studies on the wurtzite films have shown that

Material	Structure	$a$ - $b$ lattice spacing (Å)	$c$ lattice spacing (Å)	Ga ionic radius (Å)
GaN	Wurtzite	3.188 <sup>a</sup>	5.186	0.47 <sup>b</sup>
	Zincblende	4.52 <sup>c</sup>	4.52	
MnN	Distorted rocksalt	4.256 <sup>d</sup>	4.189	

Table 3.1: Structural parameters of GaN and MnN thin films at room temperature.

<sup>a</sup> Leszczynski *et al.* 1996 [130]

<sup>b</sup> Weast 2005-2006 [131]

<sup>c</sup> Strite and Morkoç 1992 [132]

<sup>d</sup> Suzuki *et al.* 2000 [133]

the addition of Mn alters the  $a$  and/or  $c$  axis lattice spacing relative to undoped GaN [55, 58, 75, 88, 89, 94, 105, 109, 116, 125–129], due to strain resulting from Mn substituting for the Ga in the films. This can be used to infer the oxidation state of the incorporated Mn, as different ionised states have very different ionic radii [119]. The few cases of zincblende GaMnN films prepared report no change of lattice spacing from the zincblende GaN value [83, 124].

The microcrystalline structure is recognised as one of the most crucial aspects in determining the magnetic properties of GaMnN, and much attention has been paid to investigating this in the literature. XRD is routinely used to rule out the presence of clustering or alternate phases, although it is known that small crystallites or amorphous Mn-rich material may not be visible in typical XRD patterns [134], and such phases have been detected using TEM or x-ray photoelectron spectroscopy that have been invisible in XRD [56]. Synchrotrons provide a far more intense source of monochromatic x-rays than used in conventional diffractometers, and synchrotron x-ray diffraction (SXRD) has been applied to more sensitively investigate the crystal structure of phases in GaMnN [97]. More com-



monly, TEM imaging and electron diffraction patterns have proven useful in identifying nanometer-sized Mn clusters barely seen or completely invisible in typical XRD patterns of GaMnN films [112, 128, 129]. However, it is not feasible to investigate an entire macroscopic specimen using electron microscope techniques, and a lack of identification of alternate phases with these methods is therefore no proof of their absence. SXRD may still not identify the presence of material in a disordered state, and cannot be considered definite evidence of single-phase material in isolation either. Extended x-ray absorption fine structure (EXAFS) remains the most powerful technique for probing a macroscopic specimen on the nanometer-scale [135].

EXAFS measurements have previously been applied to GaMnN films, and a number of reports exist on the spectra observed from single- and multi-phase material. Most such studies reported an increase in the Mn-N and Ga-N bond lengths over that seen for the Ga-N bond in crystalline Mn-free GaN films [68, 136–139]. The extension of this bond length appears to scale with Mn concentration, up to 6.2% at  $x \sim 0.05$ . The presence of Mn-rich alternate phases that might give rise to the ferromagnetic behaviour seen in many reports was confirmed in a number of films [83, 114, 139]. EXAFS was crucial in identifying these phases, which were invisible in other structural measurements used. Others have ruled out the presence of such alternate phases with comparisons of modelled structures to the experimental EXAFS-derived pseudo-radial distribution functions (pseudo-rdfs) [136] and support the conclusion of substitutional incorporation of Mn for Ga in GaMnN films up to  $x \approx 0.05$  [137, 138]. At higher Mn contents up to  $x = 0.18$ , unwanted phases that affect both the conductive and magnetic properties could be seen to form [114].

In this study a number of characterisation measurements have been performed on GaMnN samples with Mn concentrations ranging from 4–18 at. % in order to investigate the structure of the films. In particular EXAFS measurements have been used to sensitively determine the effect of such high Mn contents on the microstructure.

### 3.1.3 Electrical conductivity

As discussed in Section 3.1.1, many of the theoretical calculations for above-room temperature  $T_C$  in GaMnN assume a model of hole-mediated ferromagnetism. Mn is nominally a  $p$ -type dopant in GaN, and is expected to be compensated by donor defects present in GaN films such as N vacancies and Ga interstitials, resulting in highly resistive material. GaMnN thin films grown by MBE have been seen to exhibit higher resistivities than in undoped GaN, and resistivity increases with increasing Mn concentration up to  $x = 0.10$  [66, 140–142]. There is a wide spread in room temperature resistivity values for films with similar Mn contents from  $10^{-3}$  to above  $10^{10} \Omega\text{cm}$  [142–144]. Mn-implanted films are expected to have a larger concentration of defects, and these films have lower resistivities than MBE films, although co-implantation with  $N^+$  ions decreases the density of N vacancies, increasing the resistivity significantly [97]. Co-doping with numerous elements has been used to adjust the film resistivities [82, 106, 145], and this has an effect on the magnetic behaviour also.  $P$ -type conduction in wurtzite GaMnN was achieved through MBE growth, and  $\text{Mn}_3\text{GaN}$  precipitates lowered the resistivity of the films due to the higher density of carriers originating from this metallic phase, accompanied with an enhancement of the ferromagnetic signal [115]. However, as the extra carriers are electrons, it is not clear exactly how the precipitates aid ferromagnetism through the hole-mediated model. The same enhancement of carrier concentration has been seen in hydride vapour-phase epitaxy  $n$ -type films upon high Mn doping, accompanied by room temperature magnetic hysteresis [116]. It is worth noting the point has been raised that the predominant conduction mechanism observed in films grown on  $n$ - or  $p$ -type substrates may be due to the substrates themselves. Strassburg *et al.* pointed out that the conduction of MBE-GaMnN grown on  $n$ -type GaN substrates was  $n$ -type, with carrier concentrations close to the values expected from the bare substrate layer, even in the case of additional doping with Si donors [146]. MBE-GaMnN layers grown on Mn-containing GaN substrates however were highly resistive.

In this study temperature-dependent resistivity measurements have

been made on the GaMnN films, and the conduction characteristics of disordered films with very high Mn contents will be shown.

### 3.1.4 Optical properties and Mn impurity level positions

The other key considerations regarding the magnetic properties of carrier-mediated ferromagnetism in models for DMS are the positions of the dopant magnetic ion energy levels within the semiconducting bandgap and the oxidation state of the dopant. Three types of Mn centres have been reported in III-V semiconductors: a neutral acceptor formed by substitutional  $\text{Mn}^{3+}$ ; a neutral acceptor of substitutional  $\text{Mn}^{2+}$  with a weakly bound hole associated with the Mn  $3d$  states; an ionised acceptor of substitutional  $\text{Mn}^{2+}$  [60]. Each Mn oxidation state has a distinct value for the ground state moment and adds electronic states at different energies, so the oxidation state(s) in a given material can in principle be determined using probes of the magnetic and electronic structure. The optical properties of GaMnN are often used to draw conclusions about the state of the incorporated Mn.

In the literature at this time there are two differing interpretations of optical measurements on GaMnN films. The first attributes an optical absorption seen at 1.4 eV to transitions from the valence band to a  $\text{Mn}^{2+}$   $3d$  final state deep in the GaN bandgap, and considers a broad absorption above 2.1 eV to originate from transitions from the same Mn state to the conduction band [86, 117, 147, 148]. The second interpretation rules out the presence of Mn in the  $2+$  oxidation state in highly resistive films, and places a  $3d$  state of  $\text{Mn}^{3+}$  at 1.8 eV above the valence band. A combination of photothermal deflection spectroscopy with reflection and transmission measurements and photoluminescence shows that the transition at 1.4 eV corresponds to a spin-allowed internal transition between  $3d$  states of  $\text{Mn}^{3+}$ , and an absorption onset above 1.8 eV is the direct  $\text{Mn}^{3+}$   $3d$  state to valence band transition [75, 143, 149]. This interpretation is supported by measurements on other highly resistive GaMnN layers [56, 140, 145, 150]. Otherwise the level concerned is attributed to a  $3d$  state of the similar  $\text{Mn}^{2+}$ +hole configuration [151, 152]. Other methods of deter-

mining the spin state of the incorporated Mn involve magnetic resonance. Electron spin resonance (ESR) or electron paramagnetic resonance (EPR) spectroscopy reveals Mn is predominantly in the 3+ ionisation state in resistive GaMnN or GaMnN:Mg [143, 145], and in the 2+ state upon codoping with Si [143]. Mn-implanted GaN films show a large number of mid-gap energy levels, likely related to transitions involving extensive types of implantation-induced defects such as N or Ga vacancies and Ga interstitials [153]. Red- and blue-shifts of the bandgap in Mn implanted or PLD films of  $\sim 30$  meV have both been seen [66, 89], and are well correlated with a respective increase or decrease of the lattice parameter [95, 109]. Numerous other optical characterisation studies exist that explore the energies of transitions involving intrinsic donor and acceptor levels, excitons or levels associated with dopants such as Mg and Si [80, 103].

The one agreement amongst all measurements is that the Mn acceptor level is located deep in the bandgap of GaN, and is unlikely to lead to the delocalised *p*-type carriers that are expected to be necessary for RKKY-type ferromagnetism. In line with this and the theoretical calculations, it is essential that the oxidation state of the incorporated Mn is investigated on a case-by-case basis to aid in determining the predominant exchange mechanism present.

In this study a combination of optical measurements has been used to ascertain photon absorption within the bandgap of GaN that is induced by the Mn content.

### 3.1.5 Magnetism

Despite the near unanimous agreement on the unsuitability of the position of Mn acceptor levels in generating free carriers, ferromagnetic properties have often been reported in all types of GaMnN film preparations; MBE [72, 115, 154–156], MOCVD [100], PLD [119], nebulised spray pyrolysis [86], Mn-implantation [56, 94] and co-doping with Si, Mg [54, 98], N [97], O [157], H [102] or Be [82]. The reported Curie temperatures cover a huge range, from 10 K [67, 142] to above 750 K [72, 142, 155, 158]. Others have reported majority paramagnetic behaviour [61, 68, 141, 159–161],

antiferromagnetic correlations to low temperatures [55, 93, 154, 162], or spin-glass behaviour [55, 118].

Although some *n*-type films exhibit ferromagnetism to extremely high temperatures [72, 98], others believe that the unexpected high electron concentration is evidence that the ferromagnetic behaviour in such films originates from metallic precipitate phases [55, 56]. Ferromagnetic behaviour is most often seen at Mn concentrations lower than  $x = 0.05$  [80]. Higher Mn contents may cause enhancement of the direct Mn-Mn antiferromagnetic coupling [76], or more of the Mn may be in the form of antiferromagnetic precipitates [114]. Hole transfer from buffer layers [163] or direct co-doping with hole dopants such as Mg [54, 114, 164] have been seen to significantly improve the ferromagnetism in some films. However, in other films ferromagnetism has been eliminated upon co-doping with either *p*- or *n*-type dopants [100]. These conflicting reports point to the clear importance of the position of the Fermi level to the magnetic character, in each individual preparation. Some studies also prove the importance of reducing intrinsic defects in ensuring the strongest magnetic responses [78, 102, 157]. In some cases the presence of precipitates is even considered to be beneficial, as the ferromagnetic coupling of single-phase GaMnN is believed to be due to the extra carriers supplied by the metallic phases [54], or due to the secondary phases themselves interacting through the carrier-mediated model [56].

Often the only evidence taken that the material is ferromagnetic has been observation of magnetic hysteresis and/or remanence [94, 116, 119]. As with structure, more careful measurements of the magnetic properties are necessary to unambiguously determine the presence of a ferromagnetic phase. The more thorough studies on the magnetic behaviour of GaMnN involve temperature-dependent measurements after cooling in and out of applied fields [154, 156, 158], EPR/ESR measurements [104], magneto-optical studies [159] or Curie-Weiss law fitting to the magnetic response [154]. Even once a definite ferromagnetic phase is identified, determining its origin is still difficult. In many cases for ferromagnetic films, the magnetic character was reported to be due to the alternate phases from the Ga-Mn-N formula discussed in the review on structure [56, 116, 126,

137], often through direct detection of such phases [74, 112, 128, 165]. One study exists that showed above-room temperature ferromagnetic  $\text{Mn}_x\text{N}_y$  phases were grown using the same conditions used to grow low-carrier ferromagnetic GaMnN films [166]. This is further evidence for the role of impurity Mn-rich phases in the observed cooperative magnetism of GaMnN, and reinforces the need for the combination of careful structural and magnetic characterisation of individual film preparations to determine all the phases present.

In this study magnetic measurements have been carried out using field loops and temperature dependent magnetisation curves to probe the magnetic character of the GaMnN films. Curie-Weiss law and Brillouin function fits have also been used to draw conclusions regarding the type of magnetic interactions present and on the spin state of the incorporated Mn ions.

### 3.2 MnN

The most N-rich of the Mn-N system of compounds is of particular interest as the end member of the  $\text{Ga}_x\text{Mn}_{1-x}\text{N}$  series. As a possible secondary phase in these materials, it is surprising that few studies have been undertaken into its electronic properties. It has been hypothesised that Mn-N compounds may be the cause of the high temperature ferromagnetism seen in GaMnN [135]. The structure and magnetic behaviour of other stable compounds  $\text{Mn}_4\text{N}$  and  $\text{Mn}_3\text{N}_2$  are known [76, 111, 128, 135, 167] and quoted in many studies as possible causes of the GaMnN ferromagnetism [74, 165, 166], so in this study attention is turned to the less known MnN.

In some early theoretical works the band structure was calculated using incorrect structure or magnetic ordering for MnN [168, 169]. Theoretical rocksalt (NaCl) and ZnS structures for MnN have been investigated using the full-potential linearised augmented plane wave (FLAPW) method for calculating total energies. The experimentally observed NaCl structure was found to have the lowest energy [170] and to be a metal. A number of calculations based on this first principles method have found

the equilibrium NaCl structure lattice parameters to be in close agreement with experiment [171, 172] and that the antiferromagnetic state is stable [171]. LSDA calculations agree that antiferromagnetism is the lowest energy state in NaCl-MnN, and calculations of the equilibrium lattice constants have shown general agreement with experiment, although the expected underestimation of lattice constants from the LSDA method applied to such narrow-band systems was noted [172]. Magnetic orderings of MnN in the hypothetical wurtzite, zincblende and NiAs structures have also been investigated within spin-polarised density functional theory [173, 174].

Experimentally, almost stoichiometric MnN films have been prepared by DC reactive sputtering of a Mn target in a mixture of Ar-N<sub>2</sub> gas [175, 176], MnN powder with a few % N vacancies has been made through nitriding Mn powder in NH<sub>3</sub> at 600 °C for 12 hours [177] and thin films were grown on MgO[001] substrates using MBE at temperatures of 250-450 °C [178]. Powder XRD studies showed that MnN has a face-centered tetragonal (fct) structure with lattice constants  $a = 4.256 \text{ \AA}$  and  $c = 4.189 \text{ \AA}$ , and slightly smaller values of  $a = 4.219 \text{ \AA}$  and  $c = 4.129 \text{ \AA}$  in preparations with N vacancies. The MBE films agree with the structure of the N deficient material, having  $a = 4.22 \text{ \AA}$  and  $c = 4.12 \text{ \AA}$ . A comparison of the intensity of the scattered x-ray peaks of the stoichiometric material with those calculated from the two possible fct phases for AB compounds - NaCl or ZnS - revealed that MnN is in the NaCl structure, with a slight compressive distortion in the  $c$  axis [175]. This so-called  $\theta$ -MnN phase was found to be stable to 753 K, and N loss at higher temperatures resulted in the signature of Mn<sub>3</sub>N<sub>2</sub> and other N-poor phases becoming predominant in XRD measurements. Temperature-dependent XRD performed from 323 to 803 K showed that the splitting of the  $a$  and  $c$  axis reflections disappears at 668 K, where the structure becomes face-centered cubic (fcc) without the  $c$  axis distortion [179]. Measurements at higher temperatures performed under 3 GPa of h-BN to prevent N loss from the MnN powder showed a sharp increase of  $c$  above 600 K until the structure becomes fcc at 668 K. The structural characteristics of MnN at ambient temperatures and pressures are quoted in Table 3.1 for ease of reference.

Measurements of the magnetic behaviour to 750 K revealed an almost constant magnetisation below 650 K, with decreasing values at higher temperatures [175]. Neutron diffraction measurements [176, 177] confirmed that MnN is antiferromagnetic, with moments ferromagnetically aligned in the  $c$  axis planes, and adjacent  $c$  axis planes antiferromagnetically aligned. This type of ordering is known as antiferromagnetic order of the first type. The Mn moments are tilted away from the  $c$  axis direction by  $22.7^\circ$  at ambient temperatures, and at 550 K have rotated parallel to the  $c$  axis direction [177]. At higher temperatures the moments reduce continuously to zero, providing strong evidence for a transition to a paramagnetic state above  $T_N = 650$  K. The  $c$  axis compression at temperatures less than  $T_N$  is considered to be due to magnetostriction resulting from the antiferromagnetically ordered state, since the structural change to fcc occurs at the same temperature as the loss of the magnetic ordering [175].

The contribution of this study to understanding  $\theta$ -MnN is an analysis of the structure, DC resistivity and optical conductivity behaviour of thin films of MnN. The optical conductivity behaviour will be compared with band structure calculations performed by a collaborating researcher and interpreted on the basis of a combination of inter- and intra-band transitions and a metallic Drude term. X-ray probes of the partial density of states (PDOS) for both Mn and N will be compared with the band structure calculations. Magnetic measurements have also been undertaken to investigate the reported antiferromagnetic ordering at room temperature.

### 3.3 Summary and Outlook

Despite preparation of GaMnN thin films with a number of different processes and extensive experimental investigation, there is no agreement on the optimum preparation conditions or on the intrinsic magnetic character of single phase films. Recent theory suggests that GaMnN may not be as promising a material to realise room-temperature semiconducting ferromagnetism as first thought [44, 45, 180]. However, due to the continuing reports of such behaviour in experimental studies, further exploration of films prepared with different growth techniques is of significant interest.



In particular, preparation of GaMnN with highly non-equilibrium techniques is an area almost unexplored in the literature, and is highly desirable as a method that reduces the likelihood of precipitation of unwanted phases. Because of the apparent strong tendency of Mn to form alternate phases in the GaN film when grown with standard methods, as well as the sensitivity of magnetic characteristics to the exact growth conditions, it is essential to investigate both the structure and magnetic behaviour of individual preparations very carefully. Utilising a number of complementary methods is highly recommended in order to ensure the detection or exclusion of the possibility of alternate phases of the Ga-Mn-N compound series.

One possible alternate phase that may be present in GaMnN films is MnN. Despite a few experimental investigations, there has until recently been little effort applied to compare band structure calculations with experimental measurements on MnN. Such a comparison is of value in refining first principles calculations of the properties of these potential alternate phases in GaMnN, and may help determine their effects on the observed properties of this DMS. Transition metal nitrides are known to be harder and less sensitive to corrosion than the pure metals, and are thus of similar interest in technological applications. These materials have also proved an efficient testing ground for methods of band structure calculation that treat systems containing strongly correlated  $3d$  electron states, and assembling experimental data on them is of importance in the further development of these techniques.



# Chapter 4

## Growth

### 4.1 GaMnN and MnN films

The usual GaMnN film growth techniques of MBE and MOCVD are carried out at high temperatures and necessarily involve high mobilities of the Mn, which can result in undesired precipitation of Mn-rich material. In Mn-ion implantation of already-prepared GaN films the depth distribution of Mn is non-uniform and dependent on the ion energy. Low temperature growth techniques can avoid these drawbacks, by allowing large concentrations of dopants to be incorporated into a film with a uniform depth distribution whilst simultaneously avoiding precipitation.

One such technique is ion-assisted deposition (IAD), which is the technique used in this study to grow GaMnN films with high Mn concentrations. IAD growth results in films in structurally disordered states, which also provides the opportunity to investigate the effect of disorder on material properties. Previously, GaN and GaN:O thin films have been grown using IAD and a number of studies have been made on these materials. Disordered GaN [120, 181, 182] has been found to retain many of the useful qualities of single-crystalline films, in line with theoretical predictions [183], without the disadvantage of expensive and difficult preparation techniques. Little attention has been paid in the literature to whether the properties of GaMnN films could also prove insensitive to a higher degree of disorder.

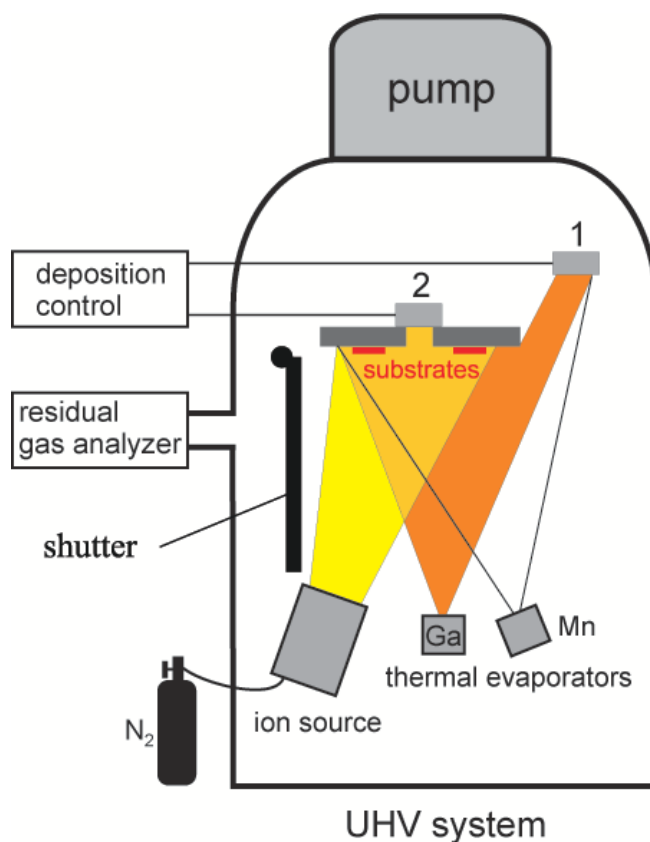


Figure 4.1: Diagram of growth chamber used for deposition of GaMnN and MnN thin films.

A diagram of the equipment used for IAD growth of GaMnN thin films is shown in Figure 4.1. High purity Ga and Mn metals are thermally evaporated in a vacuum onto a number of substrates. Simultaneously a beam of low energy N ions is directed onto the substrates, resulting in the growth of a thin film. Controlling the Mn evaporation rate allows GaMnN films to be grown with a range of Mn contents. For MnN films only Mn metal is evaporated during sample growth. Depositions are carried out at room temperature in a chamber previously pumped and outgassed to  $\sim 10^{-8}$  mbar. A single preparation results in film growth over an area of  $\sim 10 \text{ cm}^2$ , allowing films to be deposited on multiple substrates simultaneously.

### 4.1.1 Ion-assisted deposition details

Ga (99.9999% purity) and Mn (99.99% purity) metal sources are loaded into the ultra-high vacuum (UHV) chamber in an alumina basket and a W boat respectively. The UHV chamber is approximately 300 mm in diameter with an approximate capacity of 80 l. Substrates ([100] oriented Si, glassy SiO<sub>2</sub>, glassy C and mylar) are cleaned in an ultrasonic bath of isopropyl alcohol and rinsed in deionised water before loading them onto the substrate holder. The substrates are held onto the substrate holder with carbon tape. The ion gun is fed with ultra-high purity N<sub>2</sub> gas (<0.5 ppm O<sub>2</sub>), which is passed through a Ni sponge scrubber for further reduction of unwanted residual gases. The N<sub>2</sub> gas flow rate into the ion gun is 3 sccm, and a potential of 55.5 V ionises a portion of the gas. The N<sub>2</sub><sup>+</sup> and N<sup>+</sup> ions are then accelerated at energies of up to 1000 eV.

Prior to film growth the UHV chamber is pumped out with an Alcatel ATP900 turbo-molecular pump, which pumps N<sub>2</sub> gas at a maximum of 900 ls<sup>-1</sup>. Thermal outgassing of the chamber walls, ion gun, substrate holder and metal sources results in a base pressure of  $\sim 4 \times 10^{-8}$  mbar. The concentration of residual gases is monitored throughout with a residual gas analyser (RGA). The non-ionised N<sub>2</sub> gas flow through the ion gun increases the pressure in the chamber to  $\sim 1 \times 10^{-4}$  mbar during ion gun operation. Before film growth, the N<sub>2</sub><sup>+</sup>/N<sup>+</sup> ions sputter the top  $\sim 10$  nm of the substrates as an additional cleaning method. A shutter is then closed to block the substrates from the ions and metal sources.

To grow a film, power is gradually increased to the thermal evaporators until the desired evaporation rate for each metal is reached, as measured by quartz crystal monitor #1, which is shielded from the ion source. The shutter is then opened, and the substrates exposed to the evaporated metals and ions. The evaporated metals are deposited onto the substrates, and immediately sputtered away with the high ion flux. The ion current is lowered to reduce sputtering of the deposited metals until the film is growing at a constant rate of 0.5 Ås<sup>-1</sup>, measured with quartz crystal monitor #2. This is approximately half of the Ga deposition rate measured on crystal monitor #1. It is believed that the flux of high energy ions

Gas	Starting partial pressure (mbar)	Final partial pressure (mbar)
O <sub>2</sub>	$1.6 \times 10^{-9}$	$8 \times 10^{-8}$
H <sub>2</sub> O	$1.3 \times 10^{-8}$	$1.1 \times 10^{-7}$
He	$2.4 \times 10^{-9}$	$2.4 \times 10^{-9}$
Ar	$5.6 \times 10^{-8}$	$5.6 \times 10^{-8}$
H <sub>2</sub>	$2.4 \times 10^{-7}$	$1.9 \times 10^{-6}$
CO <sub>2</sub>	$1.6 \times 10^{-8}$	$1.6 \times 10^{-7}$

Table 4.1: Typical partial pressures of residual gases in the UHV chamber before and after growth of a 200 nm GaMnN film.

serves to break homopolar bonds on the deposited films and aids in the formation of stronger heteropolar bonds, resulting in more stable, uniform films [120]. A study on the effect of ion energy on the stoichiometry of GaN films grown in this way found that 500 eV ions yield uniform films with a  $\sim 1:1$  Ga:N ratio [184]. This same ion energy has been used in the growth of all GaMnN and MnN films examined in this work. The low temperature of this growth technique means the films are left in a state far from equilibrium, and are nanocrystalline. The choice of substrate material has not been found to affect the final composition or structure of the films. Growth of a 200 nm film of GaMnN or MnN takes approximately 70 minutes. Post-growth the UHV chamber is vented with high purity N<sub>2</sub> gas (O<sub>2</sub> <3 ppm) and the samples are removed from the substrate holder for analysis.

Typical partial pressures of residual gases before and after growth of GaMnN films are reported in Table 4.1. During growth, heat from the ion gun and thermal evaporators increases the chamber temperature from ambient (30 °C) to  $\sim 50$  °C, liberating higher quantities of adsorbed gases from the interior surfaces. Tables 4.2 and 4.3 report the evaporation rates of the Ga and Mn sources and the metal composition of the resultant films. In the case of preparation of MnN films only the Mn metal is evaporated.

Metal	Evaporation rate ( $\text{\AA s}^{-1}$ )	Film composition (%)
GaMnN films		
Ga	1.1	39
Mn	0.1	4.3
Film growth rate	0.5	
Ga	1.1	34.5
Mn	0.2	9
Film growth rate	0.5	

Table 4.2: Typical metal evaporation rates and final compositions for GaMnN IAD film growths. Examples are films GaMnN8 and GaMnN9 from Table 6.1. Compositions were determined using ion beam analyses (see Chapters 5.2 and 6.2.1).

Metal	Evaporation rate ( $\text{\AA s}^{-1}$ )	Film composition (%)
MnN films		
Mn	1.1	49.7
Film growth rate	0.5	

Table 4.3: Metal evaporation rate and final composition for MnN IAD film growths. Compositions were determined using ion beam analyses (see Chapters 5.2 and 6.3.1).

## 4.2 Rare Earth Nitride films

Growth of a number of REN thin films under UHV conditions was accomplished. The method involves evaporation of the RE metal using an electron gun or thermal evaporator in the presence of  $\sim 1 \times 10^{-4}$  mbar of ultra-high purity  $\text{N}_2$  gas. The RE metals react strongly with  $\text{N}_2$  gas, and films of RENs are formed where the evaporated RE metal is deposited. The growth process for the REN films is described in more detail below.

### 4.2.1 Growth details

REN films have been grown on polished  $\text{Al}_2\text{O}_3$ , on 50, 100 and 300  $\mu\text{m}$  thicknesses of [100] oriented Si and on mylar film substrates. The substrates were cleaned as described in Section 4.1.1 and then held onto the substrate holder with small melted In metal pieces, with the exception of the mylar substrates, which were held on with carbon tape. The In also provided good thermal contact between the substrates and the holder. One  $\text{Al}_2\text{O}_3$  substrate in each preparation had two Ag electrodes deposited on its surface prior to REN film growth to enable the resistance of the film to be monitored *in-situ* during growth. The path dimensions for the portion of the film deposited between the Ag electrodes are 1 cm width  $\times$  200  $\mu\text{m}$  length.

A RE metal ingot of Gd, Dy, Sm or Er of 99.9% purity is placed into a W thermal boat, alumina basket or electron gun prior to pumping the chamber to UHV ( $\sim 3 \times 10^{-8}$  mbar) conditions.  $\text{MgF}_2$  powder (99.8%) or Ga metal (99.999%) is placed into another alumina basket to provide a source for a capping layer. All metal and  $\text{MgF}_2$  sources, the ion gun, the substrate stage and the chamber walls are outgassed to ensure UHV conditions are reached. The RE metal is heated to evaporation at a rate of  $1 \text{ \AA s}^{-1}$  for approximately 10 min. This deposits a layer of reactive RE metal on the walls of the UHV chamber. This layer acts as a getter for the residual  $\text{O}_2$  and  $\text{H}_2\text{O}$  in the chamber. After this process the residual gas composition of  $\text{O}_2$  has fallen from  $1.3 \times 10^{-9}$  mbar to  $2.7 \times 10^{-10}$  mbar and  $\text{H}_2\text{O}$  from  $1.7 \times 10^{-8}$  mbar to  $2.1 \times 10^{-9}$  mbar. Compositions of residual H, He and Ar are at  $\sim 1 \times 10^{-8}$  mbar each. Ultra-high purity  $\text{N}_2$  gas is passed through the Ni sponge scrubber into the chamber at a rate of 2 or 3 sccm. The chamber pressure rises to  $1 \times 10^{-4}$  mbar with this flow. The RE metal evaporation rate is adjusted to the desired rate as measured by quartz crystal monitor #1 and then the shutter is opened, exposing the substrates to the evaporated RE metal. The RE metal reacts with the  $\text{N}_2$  gas to form a film of REN on the substrates. For this growth process the film growth rate is equal to the RE metal evaporation rate, to within the resolution of the crystal monitors ( $0.1 \text{ \AA s}^{-1}$ ). The growth and evaporation rates are stable



over the growth of a 200 nm film, which takes approximately 50 minutes. After film growth the shutter is closed, and the RE metal evaporation rate is lowered to zero.

The resulting REN films, like bulk RENs, are very sensitive to water vapour and need to be capped with a suitable material to protect them from oxidation. Monitoring the resistance across the narrow gap between the two Ag contacts during venting of the UHV chamber is a sensitive measure of the reactivity of the films. Within the first few seconds of venting the chamber with the high-purity  $N_2$  gas the resistance of unprotected films increases from  $\sim k\Omega$  to greater than  $100 G\Omega$  as the films react with residual water vapour in the venting gas. Additionally, the crystal monitors, now covered in a film of REN, register a mass increase of  $\sim 25\%$  within several hours of exposure to atmosphere, the films become transparent, and  $NH_3$  gas is released. This indicates that the unprotected REN films take up a large quantity of water from the atmosphere. To protect the REN films long enough to perform the range of characterisation techniques detailed in this study, thin film capping layers of several different materials have been deposited onto the RENs prior to exposing them to the venting gas and atmosphere. Capping layers investigated have been  $MgF_2$  and GaN. A layer of  $MgF_2$  is deposited on some films after growth by thermal evaporation of  $MgF_2$  powder onto the REN films. Other films have GaN capping layers, which are deposited using the IAD technique described for GaMnN films, omitting the Mn evaporation.

The path resistance through the film deposited between Ag contacts is measured as a function of temperature from ambient to  $\sim 90$  K after both film growth and capping layer deposition. In all cases the film resistance is found to be the same over the full range of temperatures before and after capping layer growth, indicating that the capping layer is more resistive than the REN layer and does not affect the underlying REN film besides providing protection from water vapour. With a 50-200 nm capping layer of  $MgF_2$  or GaN the film resistance does not change over  $\sim 2$  days of atmospheric exposure. After this period film resistance begins to increase and the film and capping layer begin to flake off the substrate. Storing capped films under vacuum lengthens their lifespan to months.



# Chapter 5

## Experimental Techniques

### 5.1 Introduction

Investigations of the composition, structural, electronic, optical and magnetic characteristics of GaMnN and MnN films were made using a wide and complementary variety of techniques. In this chapter these techniques are outlined.

### 5.2 Composition - Ion beam analysis (IBA)

Ion beam analysis (IBA) techniques use energetic ion beams to probe the elemental composition or structure of materials with thicknesses anywhere from tens of nm to several  $\mu\text{m}$ . These techniques typically do not alter the composition of a material and can provide depth profiles with a resolution  $\sim 10$  nm, making them very useful for thin film characterisation. In this section is a brief description of the particular IBA techniques used to determine the composition of the films examined in this study.

### 5.2.1 Rutherford backscattering spectroscopy (RBS)

A beam of ionised low mass particles (typically  $^4\text{He}^+$  or  $^1\text{H}^+$ ) directed at a solid material will mostly implant into the material (bulk), or pass through it if it is thin enough, which is the case for the thin films in this study. However, a proportion of the particles will interact with atoms in the top few  $\mu\text{m}$  of the material and backscatter. The energy of the backscattered particles is dependent on the mass of the atom within the material from which they scatter, and also the distance travelled in the material before scattering. The distribution of backscattered particles in energy space yields information on the depth distribution and relative compositional weights of the elements present. A Rutherford backscattering spectroscopy (RBS) experiment involves measurement of this spectrum and determination of the atomic ratios and depth profiles of elements with different masses present in the substance probed. This method is sensitive to elements with masses larger than the incident particle. For lighter mass elements, or in the case where the material is thick enough that backscattered particles from different elements overlap in the RBS spectrum, other IBA techniques such as Elastic Recoil Detection or Nuclear Reaction Analysis (NRA) may be necessary.

A well-established library of scattering cross-sections and recoil energies for elements of different masses exists, and using this, a simulated RBS spectrum can be calculated from a model of multiple layers comprised of given compositions and thicknesses. In practice, this model is refined until the simulated spectrum most closely matches the experimental spectrum. In this study the RBS simulation program RUMP [185] was used to find the desired values. A typical RBS experimental spectrum of a 97 nm GaMnN film with a fitted RUMP simulation spectrum is shown in Figure 5.1.

RBS has been applied in conjunction with NRA measurements to determine compositions and thicknesses of GaMnN and MnN thin films, and with both NRA and Particle-Induced X-ray Emission (PIXE) in the case of the REN films. The particle beam used in the RBS measurements was a 2.5 MeV  $^4\text{He}^+$  beam, and backscattered particles were collected over  $\sim 10$

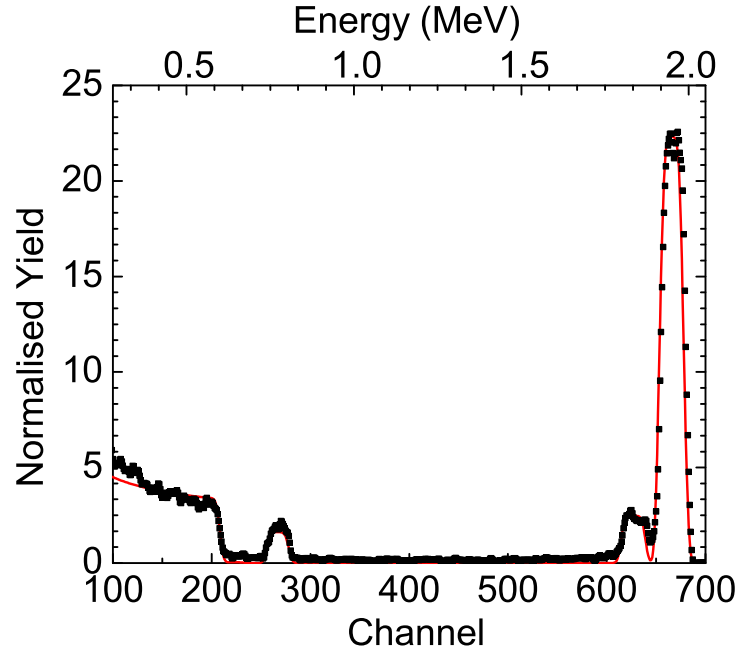


Figure 5.1: Experimental RBS spectrum (black squares) of a GaMnN film plotted with a spectrum simulated using RUMP (red line). The simulated spectrum is for film GaMnN5, and model parameters are reported in Table 6.1.

minutes until 30  $\mu\text{C}$  charge was collected. All RBS, NRA and PIXE measurements were performed with the collaboration of Dr. John Kennedy using ion beams produced by the 3 MV Van-de-Graaff accelerator at the National Isotope Centre, GNS Science, Lower Hutt, New Zealand.

### 5.2.2 Nuclear Reaction Analysis (NRA)

When the high-energy ion beam used in RBS impinges on a material, nuclear reactions may take place involving elements with  $Z < 30$  ( $Z$  = atomic number). The products of these reactions include gamma rays of precise energy, that can be identified as resulting from a particular reaction. The number of counts detected corresponding to each reaction can be used to give an absolute composition for the starting elements. This measurement can be performed simultaneously with an RBS experiment and pro-

vides a useful method of confirming the concentration of lower mass elements such as N, O and C, especially in the case where overlap between backscattered peaks from elements of interest is large in the RBS measurement. NRA performed simultaneously with the RBS measurements has been used to confirm the N and O compositions of the GaMnN, MnN and REN films. Analysis of NRA measurements was carried out by Dr. John Kennedy.

### 5.2.3 Particle Induced X-ray Emission (PIXE)

Similar to NRA, the energetic ion beam can induce the emission of x-rays from atoms excited to higher energy states in the material under investigation. PIXE x-rays can be detected and analysed for most elements with  $Z > 11$ . Since the count rate is proportional to the number of atoms of a particular element present in the material, absolute compositions of the heavier elements can be determined in a similar way to the method used in NRA. For the REN thin films, in the RBS spectra there was substantial overlap between the RE peaks and the Ga peaks from the GaN capping layers. PIXE measurements have been applied to the REN thin films to check the RBS-derived compositions of the RE elements present. These measurements were performed by Dr. John Kennedy.

### 5.2.4 Secondary ion mass spectroscopy (SIMS)

An alternative IBA method for determining a depth profile of the composition of a thin film is secondary ion mass spectroscopy (SIMS), which uses an incident beam of high energy, high mass ions. Counter to RBS and NRA, which do not ablate the material they impinge upon, the ion beam used in SIMS sputters an area of the sample. Most of the sputtered material has a relatively high probability of ionisation, and the ionised particles are detected with a mass spectrometer. The absolute elemental composition cannot be determined from SIMS without comparing the sputtering yields from a sample of interest to those from a standard of known composition. However, uncalibrated SIMS yields as a function of depth are very useful in investigating depth-dependent variations in the elemental

concentrations. SIMS experiments have been used in this study to find qualitative elemental depth profiles in GaMnN and MnN samples, and complement the quantitative elemental concentrations determined from RBS and NRA. In these experiments the particles detected were not individual N, Ga etc. ions, but quasi-particles of ionised Cs bonded to the atoms ablated from the films. The SIMS measurements were performed with the assistance of Armando Atanacio and Dr. Ben Ruck at ANSTO, Lucas Heights, New South Wales, Australia using a  $^{133}\text{Cs}^+$  ion beam at 2.42 keV.

## 5.3 Structure

As outlined in Section 3.1.2, the structure of GaMnN is a crucial consideration involved in interpreting the measured electronic and magnetic properties. Characterisation with a number of complementary methods is necessary for a thorough understanding of the microstructure of individual preparations. Several different experimental techniques have been performed to determine the structure of the GaMnN films, including EXAFS on films with differing Mn concentrations. The structures of MnN and REN films have also been investigated using XRD. EXAFS has also been performed on MnN.

### 5.3.1 X-ray Diffraction (XRD)

XRD is a technique that involves the coherent interference of scattered monochromatic x-rays to deduce the structure of a material. An electron that experiences a periodic electromagnetic field will oscillate with the same frequency as the field. When an x-ray interacts with an atom, the atom's electrons oscillate with the x-ray frequency and re-emit radiation. The emitted radiation from multiple atoms interferes constructively in only a few directions due to the presence of structural order in the material. For crystalline materials, this process is normally described as constructive interference from x-rays reflecting off parallel crystalline planes. The Bragg condition contends that a constructive interference peak occurs

where the path length difference between scattering planes is equal to an integer number of wavelengths of the x-ray radiation. The equation that determines the Bragg condition is given by

$$n\lambda = 2d \sin \theta, \quad (5.1)$$

where  $n$  is an integer,  $\lambda$  is the x-ray wavelength (in the case of this study Co  $K_\alpha$  radiation with  $\lambda = 1.79 \text{ \AA}$  is always used),  $d$  is the spacing between scattering planes and  $\theta$  is the angle between the incident x-ray and the normal to the crystal plane. The lattice spacings and structure of the probed material can be determined from comparison of the angular position and relative intensities of constructive interference peaks in the experimental XRD pattern with reference patterns calculated for different crystal structures, or with direct calculations using known crystal structures.

In strongly structurally disordered materials such as thin films grown using low-energy, low-temperature deposition only very short-range structure is maintained. This reduces the intensity of constructive interference peaks, but such peaks can still be detected, allowing conclusions to be drawn about the structure of the material with reference to the crystalline description above. Strongly disordered GaN maintains its configurational order at short range [186], allowing XRD measurements to be useful in investigating the structure of GaN and GaMnN films grown using such low energy techniques.

For XRD involving small crystallites, the Debye-Scherrer formula allows determination of the average size of the crystallites. This equation is given by

$$D = \frac{k\lambda}{W \cos \theta}, \quad (5.2)$$

where  $D$  is the average crystallite size,  $k$  is a shape factor  $\sim 1$  (usually 0.9),  $W$  is the width of the peak and  $\theta$  is the angle at which the peak appears. As all thin film samples examined in this work are nanocrystalline, this equation will be used to determine the average crystallite size within the



films.

All films examined by XRD in this study have thicknesses of 80-200 nm and were deposited on crystalline Si substrates at least 300  $\mu\text{m}$  thick. In order to maximise scattering from the thin film and minimise the presence of strong substrate peaks the XRD was performed at grazing ( $0.5\text{-}1^\circ$ ) incident angle relative to the film plane. This increases the effective thickness of the film by 50-100 times. XRD was performed by Dr. Grant Williams and Martin Ryan on MnN, GaMnN and REN thin films to determine their lattice spacings and crystallite sizes.

### 5.3.2 Transmission Electron Microscopy (TEM)

TEM allows imaging of structures smaller than the wavelengths of light used in conventional microscopy. The de Broglie wavelength of an electron accelerated to 100s of keV is  $\sim 10^{-12}$  m, which enables resolution on the sub-nanometer scale, and allows electron microscope images of individual crystallites within a nanocrystalline or amorphous matrix to be created. These electrons diffract and constructively interfere in a similar manner to x-rays in XRD, creating a diffraction pattern. Unlike XRD, where the broad x-ray beam probes a large area of the sample, the narrow focus (sub-nanometer) possible with the electron beam allows the structure of nanometer-sized regions within the film to be selectively examined.

Thin films were prepared for TEM through mechanical grinding to  $\sim 50$   $\mu\text{m}$  width using a number of different sizes of grained polishing paper. Following this process, the samples were glued to half a standard Cu TEM grid, so as to partially protrude beyond the flat cut edge of the grid. The thin sample edge was then coated with a protective layer of  $\sim 100$  nm of Pt, and a trench was cut on each side of the sample using a Focussed Ion Beam (FIB) of  $\text{Ga}^+$  ions. The remaining wedge of sample was  $\sim 100$  nm thick and of a suitable thickness to transmit electrons. Figure 5.2 is a FIB image of a typical thin film sample after FIB thinning. A measurement through this film is called cross-sectional TEM (XTEM). XTEM was performed on the GaMnN films with the collaboration of Dr. Julie Cairney at the Electron Microscope Unit, University of New South Wales, Sydney, Australia.

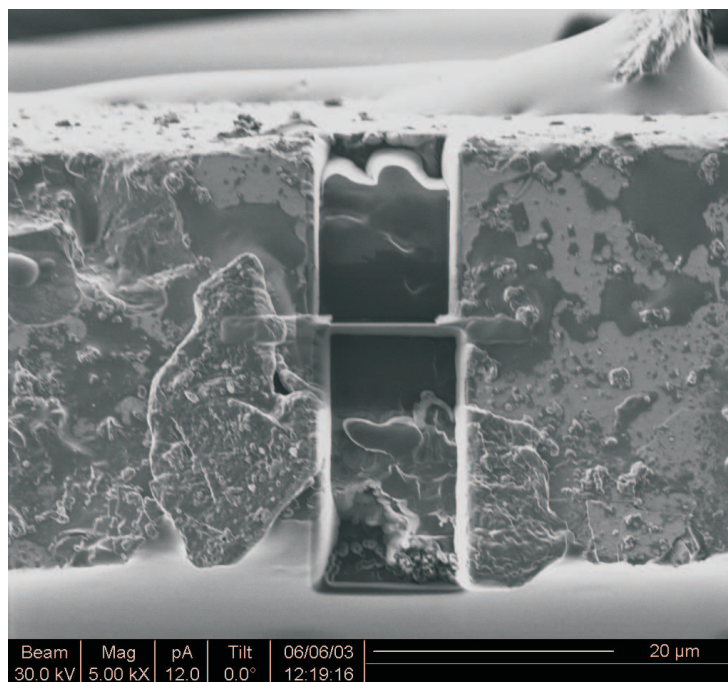


Figure 5.2: FIB image of a thin film after ion-beam milling a wedge suitable for TEM imaging. The electron beam passes through the thin wedge in the middle of the image.

### 5.3.3 X-ray absorption and emission spectroscopies

X-ray absorption and emission spectroscopies allow the partial densities of states <sup>1</sup> (PDOS) for elements present in a material to be directly probed. This information allows comparisons to be made between the calculated and experimental PDOS for different elements and is extremely useful in interpreting observed electronic, optical and magnetic properties in terms of band structures. X-ray absorption and emission experiments require a high intensity tuneable source of x-rays; usually synchrotrons are the generator of choice for these x-rays.

X-rays that are incident on a material with sufficient energy excite core electrons to unoccupied states in the conduction band. The absorption of a material as a function of incident x-ray energy can be used to determine

<sup>1</sup>The contribution from one element to the density of available electronic states in a material.

the environment of the particular absorbing atom as well as the distribution of unoccupied electronic states. X-ray absorption spectroscopy (XAS) is usually divided into two regions: the region immediately above the absorption edge for the element is known as x-ray absorption near edge structure (XANES), and the region  $\sim 50$ -100 eV and above the absorption edge is the extended x-ray absorption fine structure (EXAFS).

XANES is used to map out the unoccupied PDOS for each element. Absorption onsets for different elements are separated in incident x-ray energy space, and allow the PDOS to be determined for each individual element present in a compound. Additionally, XANES can yield information on the precise oxidation state of the element, as well as seeing some effect from differing coordination around the atoms. Information on the orbital states giving rise to particular regions of the PDOS can also be obtained with reference to selection rules for electronic excitations.

EXAFS measurements provide element specific information about local atomic bonding environments. The photoelectron emitted from the core state upon absorption of an x-ray has a de Broglie wavelength given by

$$\lambda = \frac{h}{p}, \quad (5.3)$$

where  $h$  is Planck's constant and  $p$  is the photoelectron momentum. Using the relation

$$E = \frac{p^2}{2m}, \quad (5.4)$$

where  $E$  is the energy of the photoelectron and  $m$  is the (electronic) mass, the de Broglie wavelength is related to energy via

$$\lambda = \frac{h}{\sqrt{2mE}}. \quad (5.5)$$

An incident x-ray with energy 100 eV above the absorption edge for a particular element creates a photoelectron with wavelength = 1.2 Å, which is

of the order of the interatomic spacing in solid materials. As a result of this, the photoelectron scatters from atoms neighbouring the atom from which it originated and the photoelectron wave interferes with itself. This interference creates an oscillation of the absorption spectrum at energies higher than  $\sim 50$ - $100$  eV above the absorption edge of the element of interest. This is the EXAFS spectrum. Through a combination of Fourier analysis to transform the EXAFS in photoelectron wavevector space to a spectrum in real space and comparison of experimental with simulated EXAFS spectra for given atomic structures, the measured EXAFS spectrum yields information about the environment immediately around the scattering atom. Because of the element specificity of EXAFS spectra, this technique is particularly useful for investigations of the structure of DMS such as GaMnN. By comparing the environment around the host Ga and the dopant Mn atoms, conclusions can be drawn about whether the Mn is incorporated substitutionally in the GaN lattice, at interstitial sites, as clusters or in alternate phases. EXAFS is an extremely useful complement to XRD and TEM measurements for nanocrystalline and amorphous materials since it relies on scattering only from the nearest few atomic shells.

The core hole left by the x-ray absorption process is filled when an electron from the valence band falls into that empty state. The energy difference between the valence band state and the core state results in emission of an electron or photon. Spectroscopy on the energy of these emitted particles maps out the occupied valence band states. Similar to XAS, this x-ray emission spectroscopy (XES) yields element-specific information on the *occupied* PDOS. Together, XANES and XES are an effective method of probing the DOS both above and below the Fermi level, and provide a means of comparison with calculated electronic band structures.

EXAFS experiments were performed on GaMnN films at beamline 20-B of the Australian National Beamline Facility in the Photon Factory, Tsukuba, Japan. Absorption spectra were collected over the Mn and Ga *K*-edges from 6.33 keV to 7.55 keV and 10.15 keV to 11.61 keV respectively. These data were collected in fluorescent yield mode using a 36 element Ge detector. The films were cooled to 10 K with a closed-cycle cryostat to reduce the effect of thermal vibrations. The spectra were analysed using

the iFEFFIT program package [187]. In an already published study EXAFS, XANES and XES were performed on MnN [188]. The EXAFS was performed at 77 K on the Mn *K*-edge for the MnN films with spectrometer EXAFS-13, line D42 at LURE, Paris Sud University, and was collected and fitted by Dr. Annette Koo. For MnN, XANES was performed at the N *K*-edge and Mn *L*-edge using the soft x-ray undulator beamline 511 at MAXLab in Lund, Sweden. XES was carried out at the same beamline at the N *K*-edge. Both XANES and XES were collected by Drs. Ben Ruck and James Downes. Relevant results from this study will be included in the discussion of MnN structure in Section 6.3.2 and in comparison to the band structure in Section 7.2.2.

### 5.3.4 Raman spectroscopy

Raman spectroscopy measures the inelastic scattering of light from a material which arises from the excitation of vibrational phonon modes. These vibrational modes depend on the strength of bonding in the material and the structure, and a Raman spectrum can be used to draw inferences about the structure of a material [189, 190].

In a Raman scattering experiment, a beam of light with energy  $E_i = h\nu_0$ , usually from a laser, is directed onto the material of interest. The periodic electromagnetic radiation of the laser causes electrons around an atom in the material to oscillate, creating an electric dipole moment. This electric dipole can couple with ions in the material to excite vibrational phonon modes of the ion lattice. The atom has been excited to a higher energy 'virtual' state, and upon relaxation, if a phonon has been excited, the atom relaxes to a different final state than the initial, due to energy loss to the phonon modes. The probability of excitation of a phonon is small, and most relaxation is to the same initial state. To conserve energy a photon is emitted from the atom, and in the case that the final state is different to the original state, this photon has a different energy  $E_f$  than the original exciting photon energy  $E_i$ . The absorption and emission of the two photons involved takes place over very short timescales, and the photon is said to be 'scattered' rather than 'emitted' in order to distinguish this from processes

that take place over longer timescales such as luminescence. The spectrum of scattered photons is detected and constitutes a Raman spectrum. There are three types of scattering: Rayleigh scattering is elastic scattering of light (i.e. where no phonons are created), where the outgoing photon is of the same energy as the initial excitation  $E_f = h\nu_0$ ; Stokes frequency photons are those scattered when the final atom state is at a higher energy than the initial state  $E_f = h(\nu_0 - \nu_w)$ ; anti-Stokes frequency photons are scattered when the final state is at a lower energy than the initial state  $E_f = h(\nu_0 + \nu_w)$ . This study will be concerned only with Stokes Raman scattering, where the outgoing photon is shifted to a lower energy due to excitation of vibrational phonon modes in the material.

The difference in energy between the exciting and scattered photons is used to determine the vibrational or phonon modes of the material being probed. In practice the intensity of the inelastically scattered light is plotted as a function of the frequency difference  $\nu_w$  from the excitation light. Not all possible vibrational modes are visible in a Raman spectrum; there are selection rules which govern the modes that can be detected.

The wavevector of the exciting photons is small, so the only phonons involved in Raman processes in crystalline materials are those very close to the centre of the Brillouin zone, and light is inelastically scattered at reasonably sharp, distinct frequencies. In the case of disordered material, there are no longer well-defined crystal wavevectors, and the scattered light consequently has a range of frequencies around those for the crystalline case. The Raman spectra in this study are all from nanocrystalline films, and the peaks seen are broad because of this relaxation of the momentum conservation rule.

Raman scattering typically involves 'virtual' excited states of the atom, molecule or solid that interacts with the incoming photon. If the exciting photons have an energy near that of a transition between stable electronic levels, the magnitude of the scattered light is greatly enhanced. This process is known as resonant Raman scattering. With semiconductors, an appropriate choice of excitation energy for resonant Raman scattering is one near the bandgap energy, corresponding to electronic transitions from the top of the valence band to the bottom of the conduction band.

In this study, both non-resonant and resonant Raman scattering have been used to probe the Raman-active vibrational states of GaMnN and the RENs. An Ar<sup>+</sup> ion laser with excitation wavelengths of 514 and 458 nm has been used as an excitation source for non-resonant Raman. A HeCd laser provided light at 325 nm for measuring resonant Raman scattering in GaMnN films. The experiments were carried out with a Jobin-Yvon LabRam microscope Raman spectrometer, enabling a focussed spot of 1  $\mu\text{m}$  at 1 mW power when using visible light and an approximately 3  $\mu\text{m}$  spot at 0.5 mW power with UV light. Experiments were performed at ambient temperatures on films grown on Si substrates.

## 5.4 DC Electrical Resistivity

To investigate the transport properties of GaMnN, MnN and REN films, DC electrical resistivity measurements were performed as a function of temperature. The following section describes the technique of these measurements.

### 5.4.1 Measurement Technique

#### GaMnN films

The resistances of GaMnN films grown on SiO<sub>2</sub> substrates were measured using a four-point probe method. A channel with two arms was scribed on the surface of each thin film using a tungsten carbide scribe. The geometry of the channel is reproduced in Figure 5.3. The channel width was typically 3-5 mm. Indium metal contacts were pressed on to the scribed channel at positions 1-4. Thin constantan wire leads were attached to the pressed In pads and held in place with another In pad pressed over the top of each contact. The GaMnN film was attached to the Cu block end of a closed-cycle cryostat with General Electric (GE) 7031 varnish. The insulating nature of the GE varnish and substrate material means the film was electrically isolated from the cryostat. A Si diode thermometer (thermometer 2) was attached to the surface of the film. A metal can was then

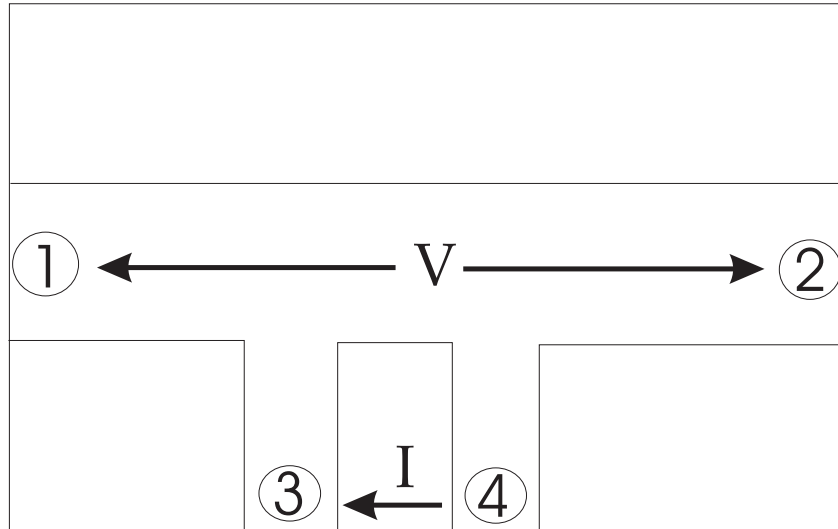


Figure 5.3: Geometry for resistivity measurement of GaMnN thin films. The channel length between positions 1-2 is typically 10-15 mm, and the channel width 3-5 mm.

placed around the film and thermometer to shield them from light and possible photoconductive or radiative heating effects during the measurement, and the sample space was pumped to  $\sim 10^{-6}$  mbar with a diffusion pump. A liquid  $N_2$  cold trap was used to prevent oil backstreaming from the pumps into the sample space. The closed-cycle cryostat and heater were then used to control the temperature of the film down to 8 K. The temperature was controlled using a Lakeshore Model 332 Temperature Controller. The controller uses a feedback loop from measurements of temperature using thermometer 1, mounted inside the Cu block of the cryostat. The correct film temperature measurement was that taken from thermometer 2, mounted directly on the surface of the film, as the insulating substrate inhibited good thermal contact between the film and the cryostat. Below 100 K the sample space was isolated from the vacuum pumps to prevent  $N_2$  gas from backstreaming and condensing on the film and contacts, and at these temperatures the sample space cryopumps itself. Temperature and resistance values were recorded during both cooling and heating of the sample. The films were cooled at a rate of 1 or 2  $Ks^{-1}$ , and left to return to room temperature gradually, at an approximate



rate of  $0.01 \text{ K s}^{-1}$ .

### MnN films

The MnN films grown on  $\text{SiO}_2$  substrates were scribed in the same four-point geometry as the GaMnN films, and were mounted in a similar way; attached to the Cu insert with GE varnish. However, due to the considerably lower metallic resistivity of MnN, measurements to liquid He temperatures were able to be made without encountering the significant leakage currents limiting the GaMnN measurements. For this measurement, the Cu insert with the attached MnN films was loaded into a glass cryostat. Both inner and outer vacuum jackets were pumped to a pressure of  $\sim 10^{-2}$  mbar. A small volume of  $\sim 1 \text{ cm}^3$  air was allowed to enter the vacuum jackets to act as a thermal transfer gas, and He gas is pumped into the sample space. Liquid  $\text{N}_2$  was poured into the outer space to pre-cool the sample space through the transfer gases. Once liquid  $\text{N}_2$  temperatures had been achieved in the sample space, liquid He was poured into the inner space. This cools the sample space through the He transfer gas. The transfer gas in the vacuum jackets condenses, providing good thermal insulation for the cooled sample space. Pumping on the sample space allowed measurements to be made to  $\sim 2.7 \text{ K}$ . Measurements were performed as the sample warmed up to ambient temperatures. Full details of the cryostat and sample holder design are contained in Ref. [191].

## 5.4.2 Resistance Measurement

### GaMnN films

A potential difference of 10 V was applied between contacts 1 and 2, and the current was measured between contacts 3 and 4 to determine the resistance of the film path between the arms of contacts 3 and 4. The maximum power dissipated in the films was 10 mW, which resulted in negligible resistive heating at temperatures of 60 K. The potential was applied with a 10 V battery and the current measured using either a Keithley 614 electrometer (currents  $< 20 \mu\text{A}$ ) or a Keithley 519A digital multimeter. The substrate

resistance is over four orders of magnitude greater than the maximum GaMnN film resistance at room temperature, therefore the measured current over much of the temperature range was dominated by that flowing in the channel of the film. Leakage currents in the circuit allowed for a maximum sample resistance measurement of  $\sim 10^{12} \Omega$ . Resistance measurements are precise to within 1 part in  $10^3$ .

### MnN films

In the case of the MnN films, a constant current of  $10 \mu\text{A}$  was passed through contacts 1 and 2, and the induced voltage was recorded across contacts 3 and 4. The voltages measured were due to resistances eight orders of magnitude lower than that of the substrates, implying that the resistance measured was entirely due to the MnN films. The current was supplied by a Keithley 224 Programmable Current Source and the voltage across the films was measured with a Keithley 195A Digital Multimeter, resulting in a resistance measurement precision of 1 part in  $10^5$ .

## 5.4.3 Temperature Measurement

### GaMnN films

The temperature was measured using two thermometers, both Lakeshore Si diode resistance thermometers, type DT-470. The voltages in both thermometers were recorded with a constant current of  $10 \mu\text{A}$ . The resistances of the Si diodes were calculated and converted to temperature with a standard calibration curve for the DT-470. The calibration is accurate to within 0.15 K from 345 K to 60 K, 0.25 K from 60 K to 30 K and 0.5 K below 30 K and covers the full range of temperatures in the experiment. Thermometer 1 was mounted in thermal contact with the Cu block at the end of the cryostat, and thermometer 2 was attached with a thin layer of GE varnish to the surface of the film being measured. The GE varnish provided good thermal contact between the thermometer and the film without allowing for an electrically conducting path. The low vapour pressure of the varnish did not affect the vacuum of the film environment during operation

of the cryostat.

The temperature from thermometer 1 was measured with a Lakeshore Model 332 temperature controller, using the pre-programmed calibration appropriate for the DT-470. Current was applied to thermometer 2 with a Yokogawa 7651 Programmable DC Current Source, and the induced voltage was measured with a Keithley 195A Digital Multimeter. The multi-meter resolution of the voltage ranges of interest was  $10\ \mu\text{V}$ , which led to a maximum uncertainty in the temperature measured of 5.5 mK. This uncertainty is small in comparison with the reported DT-470 calibration table accuracy.

### MnN films

The temperature was measured using a Rh - 0.5% Fe thermometer attached with GE varnish to the Cu insert which was in good thermal contact with the films. There was a maximum 5 mK temperature uncertainty. Full details of the thermometer calibration are contained in Ref. [28].

## 5.5 Optical absorption

As has already been described, the interaction of electromagnetic radiation with matter can yield very useful information on the properties of that material. Ultraviolet (UV), visible and infra-red (IR) light are commonly used to probe the electronic states of materials. Light in this range of energies can be used to determine the absorption or optical conductivity of materials, and is widely used to characterise both metals and semiconductors. In this section the techniques of optical absorption measurements on GaMnN and MnN over the different energy ranges of interest will be briefly described.

### 5.5.1 Optical reflection and transmission (300-1200 nm)

The amplitudes of light reflected from and transmitted through a material when light is incident normal to its surface can be calculated using

the complex indices of refraction  $\mathbf{n}$  ( $= n - ik$ ) for the media involved. The values for the amplitudes of the reflected (R) and transmitted (T) waves travelling from an incident medium  $\mathbf{n}_1$  into a medium  $\mathbf{n}_2$  are given respectively by

$$R = \frac{|\mathbf{n}_1 - \mathbf{n}_2|^2}{|\mathbf{n}_1 + \mathbf{n}_2|^2} \quad (5.6)$$

$$T = \frac{4\mathbf{n}_1\mathbf{n}_2}{|\mathbf{n}_1 + \mathbf{n}_2|^2}. \quad (5.7)$$

Equations 5.6 and 5.7 apply for reflection and transmission through the interface between two semi-infinite half-spaces with complex indices of refraction  $\mathbf{n}_1$  and  $\mathbf{n}_2$ . In the case of thin films,  $\mathbf{n}_1$  and  $\mathbf{n}_2$  correspond to the optical properties of the incident medium (usually air) and the film material respectively. In this instance, the finite extent of the film requires that the effects of reflections from the film/substrate interface as well as reflections from the bottom of the substrate are taken into account when calculating the observed reflectance and transmittance, and extra terms will appear in Eqs. 5.6 and 5.7. The problem of finding  $\mathbf{n}_i$  from measured values of R and T over a range of wavelengths can be accomplished by assuming a model for  $\mathbf{n}_i(\lambda)$ , calculating R and T and comparing with the measured  $R(\lambda)$  and  $T(\lambda)$ . The starting model is adjusted and the procedure repeated until a satisfactory match between the calculated and measured  $R(\lambda)$  and  $T(\lambda)$  is found.

If the refractive index of the incident material (usually air) is known, it is possible to use the model for  $\mathbf{n}_i(\lambda)$  to calculate the value of absorption coefficient  $\alpha = 4\pi k/\lambda$ , where the extinction coefficient  $k$  is the imaginary component of the refractive index. The value  $\alpha$  is of interest in semiconductors as it provides a measure of the absorption of light in the material and is used to determine the joint density of states, which can be used to infer the semiconducting bandgap energy.

In the visible region of the electromagnetic spectrum  $\alpha$  for the GaMnN films in this study was found using measured values of  $R(\lambda)$  and  $T(\lambda)$  as described above. R and T values were measured on these films by Drs. Tony Bittar and Annette Koo, and  $\alpha$  found from them using a program de-

signed by Dr. Ben Ruck. This analysis is possible where the film is partially transparent; at wavelengths where a film is totally opaque or near totally transparent (i.e.  $R(\lambda) + T(\lambda) \approx 1$ ) it does not apply. To extend the range of wavelengths investigated beyond the visible spectrum, or to investigate the optical properties of MnN, which is opaque to electromagnetic radiation over the whole range of wavelengths of interest in this study, spectroscopic ellipsometry and Fourier transform infra-red spectroscopy were used.

### 5.5.2 Spectroscopic ellipsometry (SE) (200-750 nm)

At excitation wavelengths short enough to be at or above the bandgap of a semiconducting film, transmitted electromagnetic waves have very low amplitudes, making modelling of  $n_i(\lambda)$  using measurements of  $R$  and  $T$  difficult in this region. Spectroscopic ellipsometry (SE) is used to determine the variation in polarisation angle of an initially linearly polarised light beam upon reflecting from the surface of a sample. Two values are measured, the amplitude and phase of polarisation, and these can be used to calculate the refractive index of the material, assuming Eqs. 5.6 and 5.7 hold.

This technique requires that the reflecting surface be smooth, flat and absorbing. At wavelengths where the material transmits a proportion of the incident light, interference from multiple reflections between the film/air and film/substrate boundaries makes determining the optical constants difficult. SE measurements have been used to determine the absorption coefficient at wavelengths near and above the absorption onset, where the films are opaque. At these wavelengths, the extraction of  $\alpha$  from the measured data requires two steps. First, the complex dielectric function must be calculated from the ellipsometric values. This can be done easily with the assumption that the light is incident on an absorbing medium such that the multiple reflections mentioned before are not a significant factor. Second, the extinction coefficient  $k$  and hence  $\alpha$  can be calculated from the complex refractive index  $\varepsilon (= \varepsilon_r - i\varepsilon_i)$  through

$$k = \sqrt{\frac{-\varepsilon_r + \sqrt{\varepsilon_r^2 + \varepsilon_i^2}}{2}} \quad (5.8)$$

and

$$\alpha = \frac{4\pi k}{\lambda}. \quad (5.9)$$

The optical absorption of GaMnN films above the absorption edge (200 to approximately 300 nm) was determined in this way using a Beaglehole Instruments Picometer Ellipsometer. The optical conductivity of MnN was calculated from SE measured over the full range of wavelengths available (200-750 nm).

### 5.5.3 Fourier transform infra-red measurements - MnN

Beyond 1200 nm the optical response of MnN has been investigated with infra-red (IR) reflection spectroscopy and more complete details are reported in another study [188]. These measurements were performed over the mid-IR-visible using a Bomem DA8 Fourier transform infra-red (FTIR) spectrometer and high-accuracy spectrophotometer, and collected by Drs. Nick Strickland and Tony Bittar. The optical conductivity was extracted from the reflectivity using Kramers-Kronig analysis such that the ellipsometry determined conductivity in the UV spectral range was reproduced.

## 5.6 Band structure calculations - MnN

As part of the analysis of the optical conductivity for MnN films, the experimental results will be compared to calculations of the band structure and optical response functions. These calculations were performed by Prof. W. R. L. Lambrecht [188] at the Department of Physics, Case Western Reserve University, Cleveland, Ohio, USA, and were carried out using the linearized muffin-tin orbital (LMTO) method in the atomic sphere approximation (ASA) [192]. The results for the band structure obtained in

this manner are in good agreement with the more detailed full-potential (FP-LMTO) calculations by Lambrecht *et al.* [193]. The imaginary part of the dielectric function was then calculated using the approach described in Ref. [194]. A description of the details of the calculation is beyond the scope of this thesis, although the results will be applied here as they are relevant to interpreting the measured conductivity values. Full details of the calculation are available in Ref. [188].

## 5.7 Magnetisation measurements

The response of GaMnN, MnN and REN thin films to applied magnetic fields was measured using a Quantum Design magnetic property measurement system (MPMS) superconducting quantum interference device (SQUID). Measurements were performed from 2 K to 300 K, in fields of up to 6 Tesla (T).

The films measured with the SQUID were those deposited on Si or on mylar substrates. These substrates have small magnetic moments and the magnetic moment of the thin films was expected to dominate the measured response. Measurements were performed on bare mylar and Si substrates of similar sizes to the GaMnN films. The magnetic responses were indeed found to be small compared to the responses of the films and have not been subtracted from the measured magnetisations of the films discussed here.

A plastic straw was cut to  $\sim 14$  cm length and folded along its length, then fitted into an uncut straw of  $\sim 19$  cm length. For the Si substrate films, the sample was cleaved into a suitable size ( $\sim 5$  mm  $\times$  10 mm or less) and placed between the two straws at a position where it would lie near the centre of the SQUID measurement coils. The mylar substrate films could be folded up and much larger areas of sample were used,  $\sim 20$  mm  $\times$  30 mm. In the case of these films, the interior straw was not needed, and the film was folded until it fit into the uncut straw without support. The uncut straw was then fitted onto the end of the Cu SQUID insert probe, using mylar tape wrapped around the end of the probe to provide a snug fit for the straw. The probe was inserted into the SQUID at room temperature

and zero applied field.

In a typical SQUID experiment, the samples were first centered in the pickup coils at applied fields of around 1 T at ambient temperature, then cooled to the starting temperature of 2-10 K in zero applied field. After the temperature had been allowed to stabilise, a magnetic field was applied to the sample. This field created a net polarisation of the magnetic moments in the film. The magnitude of this polarisation could be detected by moving the sample through a set of pickup coils wound in a second-order gradiometer configuration. This configuration consists of a centre coil of two turns of the superconducting wire and two singly wound coils, one located above and one below the centre coil. The two singly-wound coils are wound in the opposite sense to the centre coil. The second-order gradiometer setup allows the local flux change associated with the sample moving through the centre coil to be measured, whilst cancelling the effect of fluctuations in the applied magnetic field. The samples were small compared with the spatial extent of the gradiometer coils, and the effect of the magnetic moment of the sample moving through the centre coils induced a change in the current flowing through them in accordance with Faraday's law, which was not cancelled in the oppositely wound coils. The reason for this is that the sample behaved ideally as a point-source magnetic dipole moving through the centre coils, and the local change in flux was detected as a change in the current flowing through the detection coil. The variation of the SQUID voltage (current) as a function of position of the sample relative to the centre coil was fitted with a dipole curve, a linear background and a constant offset. The equation of fit that was used for this is

$$P1 + P2 \times x + P3 \times \left[ \frac{2}{(0.97^2 + (x + P4)^2)^{3/2}} + \right. \\ \left. (0.97^2 + [1.519 + (x + P4)]^2)^{-3/2} - \right. \\ \left. (0.97^2 + [-1.519 + (x + P4)]^2)^{-3/2} \right], \quad (5.10)$$

where  $P1$  is the constant offset term,  $P2$  is the linear background,  $x$  is the (vertical) dimension that the dipole moves through the SQUID coils,  $P3$  is



the dipole strength and  $P4$  is the  $x$ -position of the dipole. The fitted value of  $P3$  was transformed into a magnetic moment using

$$m(emu) = \frac{P3 \times S1}{(S2 \times sens \times S3)}$$

$$S1 = 1.825$$

$$S2 = 7512.185$$

$$S3 = 0.9125,$$
(5.11)

where *sens* is the sensitivity value of the measurement range (0.1, 0.2, 0.5, 1, 2, 5...) and the other values are calibration values specific to the SQUID in use.

The magnetisations of GaMnN, REN and MnN films were measured in this way as a function of temperature. MnN and GaMnN film measurements were done in part by Dr. Grant Williams. In a routine experiment magnetisation was measured using two temperature sweeps: a zero-field cooled run (ZFC), where the sample was cooled to low temperatures before the field was applied and the magnetisation measured as the sample was heated in the field; a field cooled run (FC), when the magnetisation was measured as the sample was cooled in the field applied at ambient temperature. In a typical experiment both ZFC and FC measurements were performed at two different applied field strengths, low (10-500 mT) and high (1-6 T). Additionally, the magnetisation was measured at a constant temperature in varying field, from -6 to +6 T. All films were measured with the applied field in the direction of the plane of the film.



## Chapter 6

# Composition and Structure of GaMnN and MnN films

### 6.1 Introduction

Investigations of the composition and structural characteristics of GaMnN and MnN films were made using a wide and complementary variety of techniques as described in Chapter 5. In this chapter the results will be presented and interpreted.

It is important to note a difference in the terminology used in this study from that common in the DMS literature. Routinely in literature reports on GaMnN material the Mn content is described as the percentage of cation (Ga+Mn) composition, so a  $\text{Ga}_{1-x}\text{Mn}_x\text{N}$  film may be referred to as containing  $x = 8\%$  or  $x = 0.08$  Mn. In this study, individual elemental compositions are expressed as percentages of the *total* (Ga+Mn+N+O) composition, so the equivalent to the aforementioned example in this study would be a GaMnN film containing 4% Mn, 46% Ga and 50% N. For this chapter and Chapter 7 the latter terminology will be used as standard, i.e. Mn content will be expressed as a proportion of the total composition. In cases where it is necessary to compare with literature reports, the Mn composition of the literature report will be expressed as  $x = \dots\%$ , and the Mn content of the films from this study as ... atomic percent (at. %) Mn.

## 6.2 GaMnN

### 6.2.1 Composition

Sample name	Thickness (nm)	Ga (at. %)	Mn (at. %)	N (at. %)	O (at. %)
GaMnN2	115	42	4.2	52	0.8
GaMnN4	114	41.4	6.2	52.3	0
GaMnN5	97	37.7	6.4	55.3	0.5
GaMnN8	183	39.2	4.3	54.2	2.4
GaMnN9	182	34.5	9	55.5	1
GaMnN10	159	44.6	10.8	40.2	4.4
GaMnN11	205	34.8	11.7	50	3.5
GaMnN12	230	26	18	52	4
GaMnNH <sub>2</sub> O	205	32	19	13	36

Table 6.1: Compositions and thicknesses of GaMnN films. Uncertainties are estimated at 1-2 %.

The compositions of GaMnN films as determined by RBS and NRA are listed in Table 6.1. The films have Mn contents varying from 4-18 at. %. Half of the films have O contents of 1 at. % or lower, and the films with higher (10.8, 11.7, 18 at. %) Mn contents tend to have higher O contents of up to 4.4 at. %. A film has also been prepared with intentionally high Mn (19 at. %) and O (36 at. %) contents throughout the film.

Figures 6.1 and 6.2 show the sputtering yields of Ga, Mn, N and O from the SIMS experiments on GaMnN5 and GaMnN10. The Ga, Mn and N yields increase only very gradually with depth into the film and are almost constant for sample GaMnN10. The O yield is lower than any of the other elements throughout most of the thickness of the film, but rises towards the surface, corresponding to an increased outgassing from the UHV chamber as the films grow. There is a sharp increase of O yield in the top  $\sim 2$ -10 nm of the films, which indicates much of the O detected in the RBS measurements is due to surface oxidation. The few % O detected by

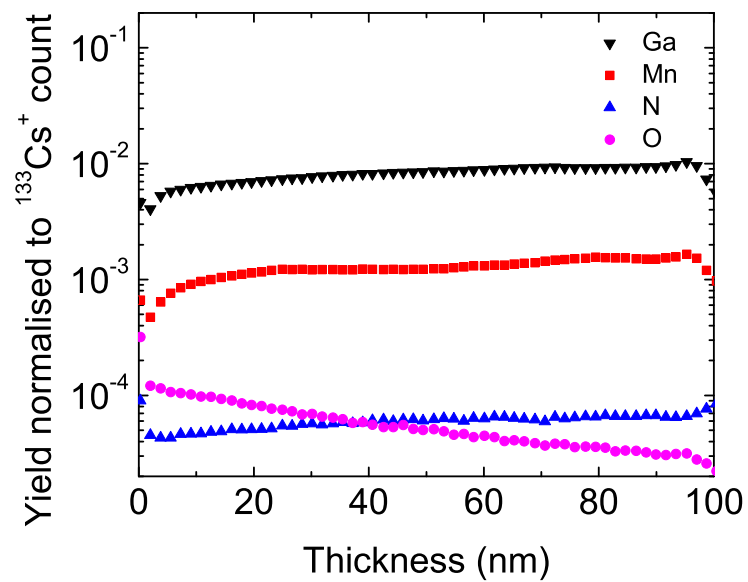


Figure 6.1: Normalised SIMS sputtering yields for GaMnN5 (6.4 at. % Mn).

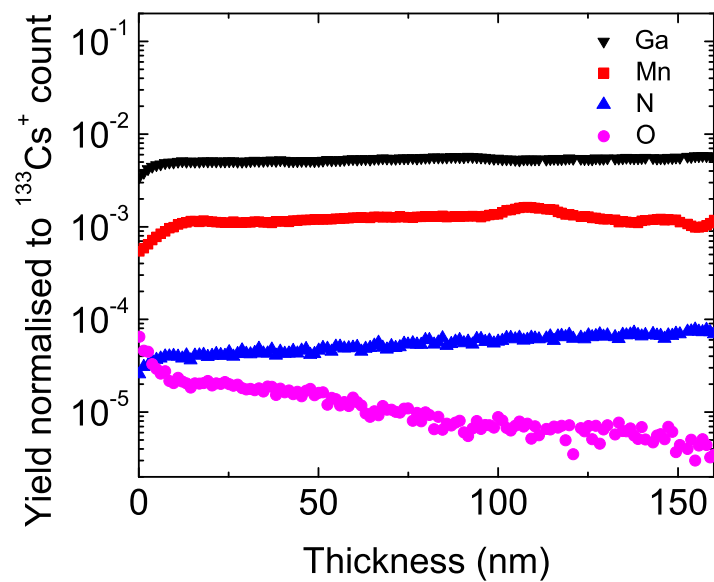


Figure 6.2: Normalised SIMS sputtering yields for GaMnN10 (10.8 at. % Mn).

RBS and NRA in these films is thus regarded as resulting from an almost unavoidable post-growth partial oxidation of the top surface and will not affect the properties of the bulk of the film. In the high O content film (not shown) the O content is distributed uniformly throughout the film, and the properties of this film are considered to result from GaMnNO material. All films except GaMnN10 and GaMnNH<sub>2</sub>O have an excess of N + O over Ga + Mn. As will be seen in the Raman spectroscopy results the excess N is in the form of N<sub>2</sub> molecules.

### 6.2.2 Structure

The grazing incidence XRD patterns of GaMnN films prepared at all Mn contents closely resemble those of Mn-free nanocrystalline GaN (*nx*-GaN) films (Figure 6.3). Using Eq. 5.2 the average crystallite size was determined to be  $\sim 3$  nm for all films. The broad XRD peaks observed agree with XRD simulations for a structure of randomly alternating wurtzite and zincblende GaN atomic configurations (random-stacked structure) [121]. The Debye-Scherrer analysis of Eq. 5.2 for the average crystallite size based on the XRD peak widths is usually applied only in the case that a single structural configuration contributes to a given peak. However, the analysis is permitted by the existence of similarly spaced parallel planes of atoms over a distance of at least several lattice spacings. In the case of the random-stacked structure of the GaMnN films, parallel planes of atoms are still present, satisfying the condition of validity for the Debye-Scherrer analysis.

In Figure 6.4 it can be seen that there is a monotonic decrease in  $2\theta$  position of the peaks as Mn is increased in the GaMnN films, which can be attributed to an expansion of the lattice spacing with increasing Mn composition. The line at  $\sim 42^\circ$  appears not to shift by the same amount as the line at  $\sim 37^\circ$ , however it should be noted that the XRD patterns of Figure 6.4 are actually comprised of three broad overlapping peaks, and this complicates an accurate quantitative measure of the extension of the lattice parameter based on the shift of the peaks. Nevertheless, a rough estimate of this lattice expansion can be made, here based on the shift of

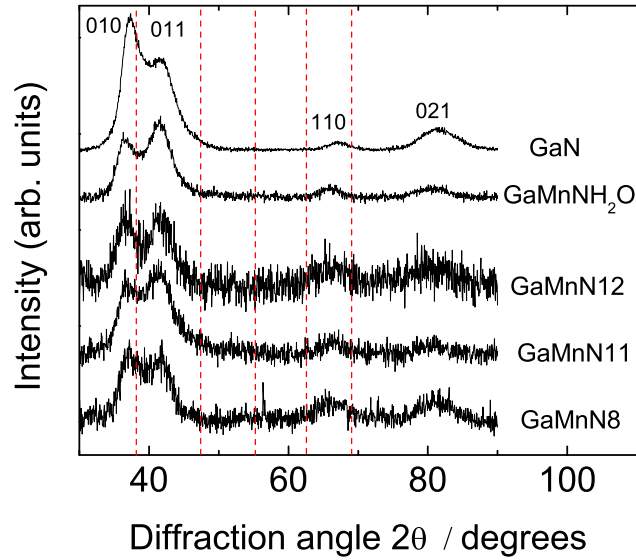


Figure 6.3: XRD patterns of GaMnN with varying Mn and O contents. Patterns resemble that for  $nx$ -GaN films in a random-stacked structure. The  $nx$ -GaN pattern peaks are labelled with Miller indices calculated for the wurtzite GaN structure. Red dashed lines indicate the calculated  $2\theta$  positions for the possible GaMn<sub>3</sub>N or Mn<sub>4</sub>N alternate phases.

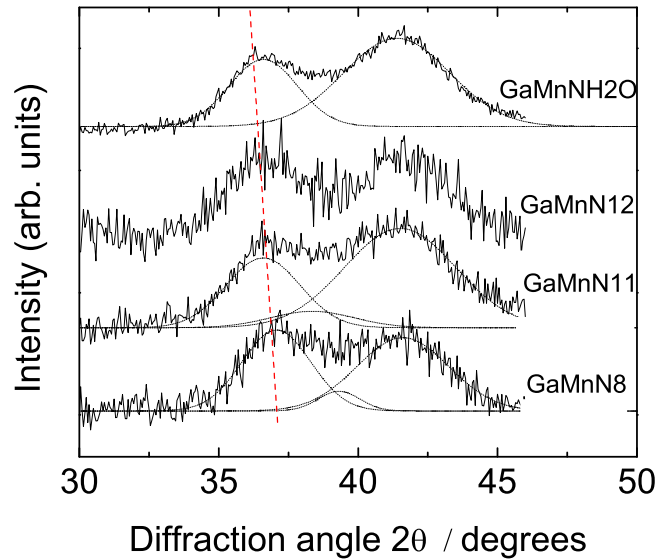


Figure 6.4: Low scattering angle XRD peaks of GaMnN with varying Mn and O contents. Fitted Gaussians and the line are guides to the eye, showing that these peaks shift to lower angles with higher Mn concentrations.

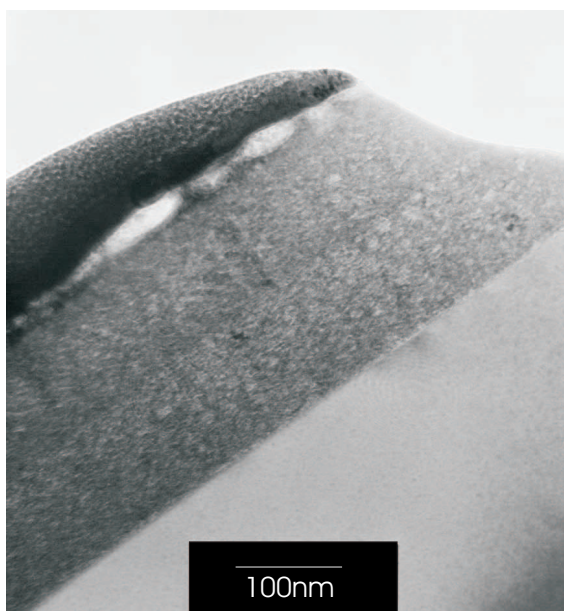


Figure 6.5: TEM image of GaMnN containing 4.3 at. % Mn. Scale bar is shown.



Figure 6.6: TEM image of GaMnN containing 9 at. % Mn. Scale bar is shown.



the low angle peak at  $\sim 37^\circ$ . The films with the highest ( $\sim 18$  at. %) Mn composition have the largest lattice expansion of approximately 2 %. Not all studies on GaMnN report such an increase in lattice spacing, although it is noteworthy that high quality free-standing single crystals of GaMnN do have larger  $a$  and  $c$  spacings than in GaN [58], and cannot be affected by substrate mismatch strain. Neglecting the partially covalent nature of bonding in GaN, some idea of the origin of this increase in lattice spacing can be gleaned. If Mn is incorporated on the Ga lattice sites in the  $2+$  oxidation state, an increase in lattice spacing is expected as the ionic radius of 4-fold coordinated Mn is 66 pm compared with the 4-fold coordinated  $\text{Ga}^{3+}$  radius of 47 pm [131]. The  $\text{Mn}^{3+}$  ion radius is smaller, and any lattice spacing increase is expected to be too small to identify. Therefore the increase of lattice spacing with increasing Mn incorporation is an indication that the incorporated Mn in these films is predominantly in the  $\text{Mn}^{2+}$  state, and this argument has been applied in other reports of high Mn content thin films [119]. The conclusion that Mn is incorporated in this oxidation state was reached in studies of single crystalline GaMnN films with Mn contents of  $\sim 5\%$  and large concentrations of donors [143]. Another possible origin of lattice expansion is Mn taking up interstitial sites, but this is an unlikely explanation in the films considered in this study as it does not account for the EXAFS measurements.

XTEM imaging was performed on GaMnN films containing 4.3 and 9 at. % Mn. The films are shown in Figures 6.5 and 6.6. The dark layer on the top of the films is the Pt layer deposited prior to FIB thinning to protect the films from ion bombardment damage. The light coloured substrate is Si for both films. Both films are uniformly comprised of crystallites throughout their thickness. A change in contrast midway through the 4.3 at. % Mn film corresponds to a small change in Mn and Ga evaporation rates during growth to maintain the film growth rate at  $0.5 \text{ \AA s}^{-1}$ . A higher magnification image of the 9 at. % Mn film in Figure 6.7 shows one of the crystallites, which are approximately 3-5 nm in size in both films, in agreement with the analysis of the XRD peak widths.

A selected area electron diffraction (SAED) pattern of an area containing the 3-5 nm crystallites in the film with 9 at. % Mn (Figure 6.8) is com-

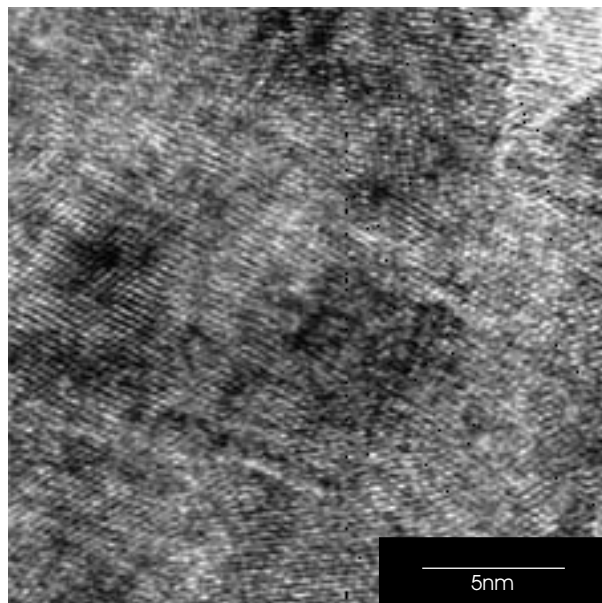


Figure 6.7: High-resolution image of GaMnN containing 9 at. % Mn. Scale bar is shown. Lattice fringes from individual crystallites can be clearly seen.

prised of a number of spotty rings. The presence of rings indicates the film is nanocrystalline. The ring diameters are attributed to the diffraction pattern from GaN-like material in the wurtzite structure, and there is no evidence for a contribution from any other phases. A spotty nature of a SAED pattern usually indicates a texturing or preferential orientation of the crystallites probed by the electron beam. However, the area of the sample exposed to the beam from which this pattern was obtained is small, of the same magnitude in area as the image of Fig. 6.7. The spottiness of the SAED pattern does not necessarily reflect a texturing of the bulk of the film in this case, and may result from the small number of crystallites involved in the creation of the pattern.

The SAED and TEM images reveal no evidence of alternate phases to the random-stacked GaMnN structure determined from XRD, and there is no sign of clusters of Mn as has been seen in TEM studies of single crystalline MBE-grown GaMnN films [165].

The Fourier transforms of the EXAFS spectra taken in photoelectron



Figure 6.8: SAED image of GaMnN containing 9 at. % Mn. The diffraction rings indicate the film is nanocrystalline and well represented by the wurtzite GaN structure.

wavevector space are pseudo-rdfs<sup>1</sup>, and are used to determine the radii of shells of atoms around the scattering atom of interest. In Figure 6.9 the pseudo-rdfs of both the Ga and Mn edges of GaMnN containing 9 at. % Mn are plotted. The first two neighbouring peaks (corresponding primarily to Ga-N, Ga-Ga for the Ga edge or Mn-N, Mn-Ga for the Mn edge) are at the same radial distance from each scattering atom, suggesting that the local environment around each atom is very similar. The pseudo-rdfs for both edges closely resemble that of the Ga edge in the EXAFS of Mn-free *nx*-GaN films previously grown with IAD [121]. A fit was made to the first two peaks from both edges using a fixed co-ordination of four N nearest neighbour atoms and 12 Ga next-nearest neighbour atoms, features common to wurtzite, zincblende or random-stacked GaN sequences. The fitted values of the model were shell radius ( $R$ ), mean square displacement factor ( $\sigma^2$ ) and edge energy correction factor ( $\Delta E$ ). The best fit parameters are

<sup>1</sup>EXAFS-derived radial distribution functions will not typically reproduce the correct amplitude of neighbouring peaks, hence they are referred to here as 'pseudo-rdfs'.

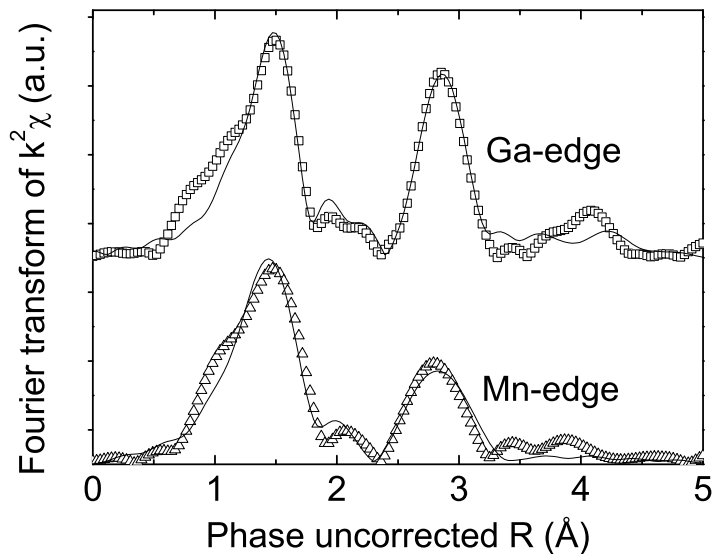


Figure 6.9: Fourier transform of EXAFS measurements taken at Ga and Mn  $K$ -edges for a GaMnN film containing 9 at. % Mn. The squares are the experimental data, the lines are best fits to the data using a model of four N nearest neighbours and 12 Ga next-nearest neighbours. The best fit parameters are printed in Table 6.2.

reported in Table 6.2. Note that wurtzite GaN actually has three nearest neighbour N atoms at 1.946 Å and one nearest neighbour N atom at a reduced distance of 1.937 Å. In zincblende GaN the first neighbouring shell is comprised of four N atoms at 1.93 Å [139]. However, these differences are close to the uncertainty in the measured bond length ( $\pm 0.01$  Å).

The radial distances to the first and second nearest shells from the Mn and Ga edges are equal to within the fitting uncertainty, and both agree with the shell radii around Ga in Mn-free crystalline GaN. An extension of the Mn-N bond length by 1 % is allowed for by the uncertainty in the best fit, and with this extension the position of the first shell peak is more closely matched by the model. However, the fit residual is slightly worsened with this expansion. The small possible bond length extension from the EXAFS is in agreement with the slight lattice expansion detected by XRD for films with similar Mn concentration (1.6 % expansion for Mn = 11.7 at. %). The result here contrasts with EXAFS measure-

	Nearest Neighbour	R	$\sigma^2$	$\Delta E$
	Atom	(Å)	( $10^{-3} \text{ Å}^{-2}$ )	(eV)
Ga edge	N	$1.92 \pm 0.01$	$2.8 \pm 1.3$	$4.23 \pm 0.64$
	Ga	$3.22 \pm 0.01$	$9.8 \pm 0.9$	$10.97 \pm 2.04$
Mn edge	N	$1.93 \pm 0.02$	$5.6 \pm 3.0$	$1.82 \pm 2.12$
	Ga	$3.19 \pm 0.03$	$17.7 \pm 2.8$	$5.52 \pm 2.27$

Table 6.2: Fitted EXAFS parameters for a model of wurtzite GaN fit to the Ga and Mn *K*-edges of the GaMnN film in Figure 6.9. The fitting was done using phase corrected data and the radii reported can be directly compared to expected bond lengths.

ments reported on single-crystalline GaMnN films that exhibit a significantly greater lengthening of the Mn-N bond, by 6.2% for  $x = 5\%$  [136, 195]. An increase of this magnitude would be easily signalled in the data of Table 6.2, so in comparison to the earlier studies, in these films the structure includes Mn primarily in sites substituting for Ga, and with similar bond lengths. The values of  $\sigma^2$  here are larger than values reported from the previous EXAFS studies on single-crystalline GaMnN [138, 195], implying that the range of bond lengths is large for both ionic species in the films. This is consistent with Mn incorporation leading to no bond length expansion at some sites, but causing a small increase in bond length at other sites. Since these measurements were performed at low temperature, thermal effects on  $\sigma^2$  are expected to be small. This further indicates the displacement is due primarily to intrinsic structural disorder in the films that is greater than in single crystal films, even within the first atomic shell. As already noted, the combination of the IAD growth process and the very high Mn content results in films far from their lowest energy state, leading to the greater degree of disorder. Note in this regard that there is a slight increase of the Mn-N bond length in a nanocrystalline GaMnN film that has been annealed, with a corresponding decrease of  $\sigma^2$  [196].

In order to check for the presence of other phases, the Fourier transforms of the experimental EXAFS spectra taken at the Mn and Ga *K*-edges

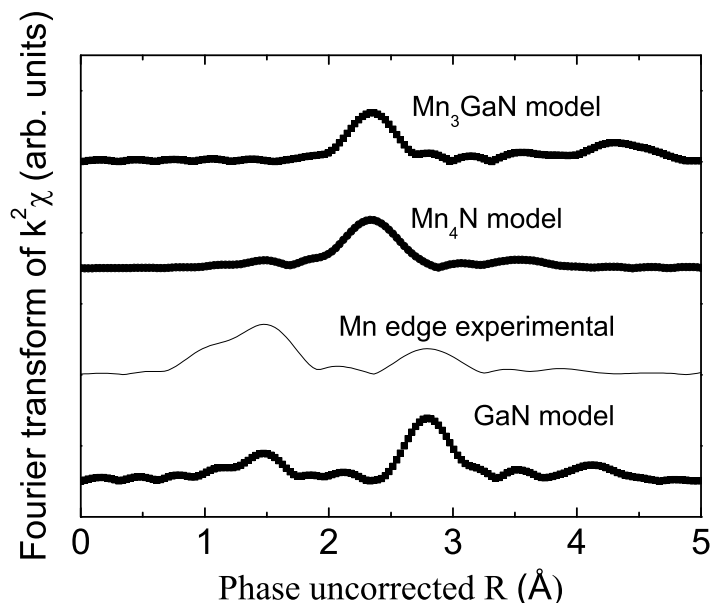


Figure 6.10: Simulations of the pseudo-radial distribution functions for  $\text{Mn}_3\text{GaN}$ ,  $\text{Mn}_4\text{N}$  and GaN compared with the Fourier-transformed Mn edge experimental data from GaMnN. The experimental data are significantly different from the Mn-containing phases, but the peak positions closely resemble the GaN simulation.

for GaMnN are compared to modelled pseudo-rdfs for configurations of Mn in Ga-Mn-N other than for substitutional incorporation. These configurations of Mn correspond to  $\text{Mn}_4\text{N}$  and  $\text{Mn}_3\text{GaN}$ , both phases previously detected in GaMnN films [113–115, 117]. Plotted in Figure 6.10 are the pseudo-rdfs calculated from models of these two impurity phases as well as that from a model of undoped wurtzite GaN, compared with the Mn  $K$ -edge experimental data. The presence of a strongly scattering Mn-related peak at a phase-uncorrected<sup>2</sup> bond length of  $\sim 2.3$  Å in the two Mn-rich compounds does not correlate with the Fourier transforms from the experimental data for either edge, whereas the bond lengths of the first two shells in the wurtzite GaN pseudo-rdf match those seen in the experimental data. Differences in the relative intensities of the first two peaks

<sup>2</sup>EXAFS needs a phase correction determined by the particular element(s) present in that neighbouring shell, and this affects the pseudo-rdf distance values. In this work, the phase has been accounted for only in the fitted values of Table 6.2.

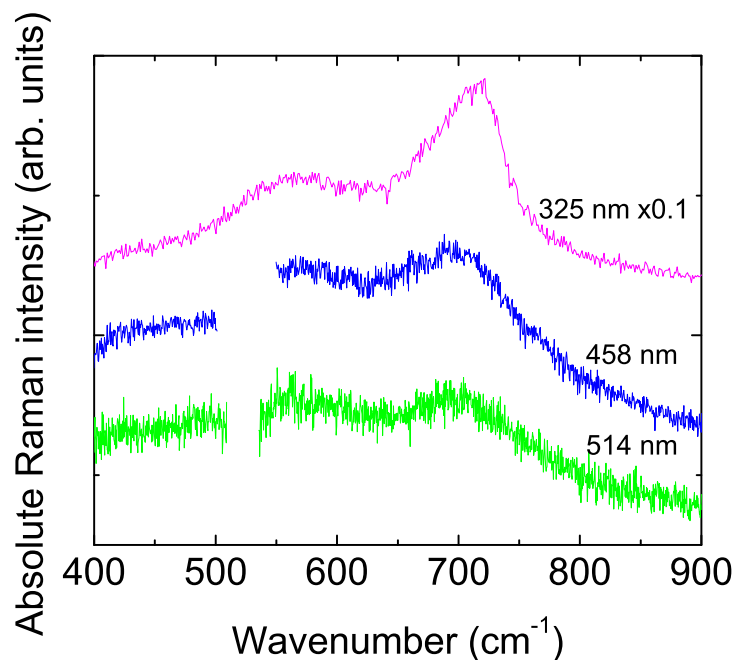


Figure 6.11: Absolute Raman spectra of a GaMnN film with 4.2 at. % Mn deposited on a Si substrate taken at various excitation energies. The substrate peak at  $520\text{ cm}^{-1}$  has been removed from the spectra taken with the 428 and 514 nm excitation energies. Note the resonant Raman enhancement of the  $710\text{ cm}^{-1}$  peak with the 325 nm excitation. Spectra have been shifted vertically for clarity.

are a measure of the level of short-range disorder in the film, and are not accounted for in the modelled pseudo-rdf of crystalline GaN. The measurements strongly suggest the Mn is predominantly incorporated into the film substitutionally for the Ga atoms rather than forming clusters or nanocrystals of Mn-rich phases such as  $\text{Mn}_4\text{N}$  or  $\text{Mn}_3\text{GaN}$ . The Mn in these GaMnN films is then bonded in the same way as Ga in GaN films: tetrahedrally bonded to four N atoms.

Raman spectroscopy has been performed on all GaMnN films discussed in this study, with the range of Mn concentrations from 4-18 at. %. Raman spectra were collected on films grown on Si substrates, under excitation from 514 nm, 458 nm and 325 nm laser sources. The spectra from films grown on other substrates were recorded and found to show no differences from the spectra taken on Si substrate films. Figure 6.11 shows the

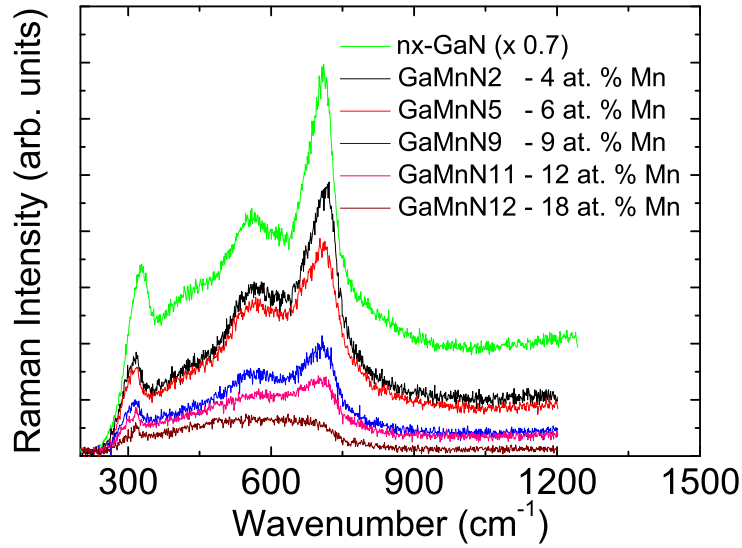


Figure 6.12: UV Raman spectra of GaMnN films with various Mn concentrations on Si substrates. Also plotted is the UV Raman spectrum from a Mn-free *nx*-GaN film grown on Si. All spectra were recorded over 100 seconds and the Si substrate peak at  $520\text{ cm}^{-1}$  has been removed.

Raman spectra taken on a film with the lowest (4.2 at. %) Mn content at 325, 458 and 514 nm excitations. The spectra are normalised by the integrated signal from a polished Si substrate taken with the same collection conditions, corrected for the laser frequency dependence of the Si signal [197], and finally the Si signal peak at  $520\text{ cm}^{-1}$  has been removed. The peak near  $710\text{ cm}^{-1}$  is clearly enhanced under 325 nm (UV) excitation, due to the near-resonant Raman scattering in a GaN-based material (GaN band gap = 3.4 eV) when using the 325 nm (3.8 eV) light. Due to the lower transmission of 325 nm light through the film the substrate signal is far less prominent in this spectrum. Due to this and the more intense Raman scattering peaks that result from the resonant Raman effect, the rest of the discussion of the GaMnN Raman spectra will be on that taken with the 325 nm light only.

Figure 6.12 plots a representative set of data taken on a number of GaMnN films using the 325 nm source. Two spectra were collected for each film over 100 seconds, each covering  $200\text{-}1200\text{ cm}^{-1}$ , and extraneous



peaks from cosmic radiation were removed automatically by the collection software. Also plotted is the (near-resonant) Raman spectrum from a *nx*-GaN film grown using IAD [198]. Note that the peak appearing in all films near  $320\text{ cm}^{-1}$  is an artefact from the sharp cut-off of the laser line filter.

The spectra of GaMnN films containing  $<18\text{ at. \% Mn}$  resemble those of *nx*-GaN films, with broad peaks at approximately  $560\text{ cm}^{-1}$  and  $710\text{ cm}^{-1}$ . As described for the IAD *nx*-GaN films elsewhere, these peaks are associated with  $k \approx 0$  modes for both wurtzite and zincblende GaN [198]. In that study the *nx*-GaN was concluded to have structural order persisting only to distances of several lattice spacings, and the additional broadening and weakening of the peaks in these films with increasing Mn concentrations indicates that the Mn further frustrates ordering. Another cause for the reduction in Raman intensity with higher Mn contents is due to an increasing shift away from resonance conditions. As more Mn is incorporated, the optical absorption edge of the GaMnN films becomes less well-defined (see Section 7.1.2) and the condition of near-resonance is less well satisfied. The Raman scattering intensity of the peaks reduces until the Raman spectrum at  $18\text{ at. \% Mn}$  is broad and featureless below  $800\text{ cm}^{-1}$ . Raman spectra taken with the other excitation wavelengths show a similar decrease in resolution and intensity of the film-related features, indicating that the band edge (and thus the resonance condition) does not shift to lower energies, but becomes broader as the films gain more states in the energy gap region, in agreement with optical and transport measurements of Chapter 7.

The GaMnN films show changes in their Raman spectra under exposure to the UV laser. Figure 6.13 shows Raman spectra taken from GaMnN5 ( $6.4\text{ at. \% Mn}$ ) at 1000 second increments over 3000 seconds of continuous UV exposure. The spectrum at 0 seconds is identical to the spectrum for the same film shown in Figure 6.12, although over time there is a strong enhancement of the GaMnN-related peaks, in particular the  $710\text{ cm}^{-1}$  peak. After 3000 seconds of UV exposure, the half-width of this peak has reduced from  $50\text{ cm}^{-1}$  to  $25\text{ cm}^{-1}$ , indicating a significant reconstruction of local crystalline order, and the area of this peak has increased to

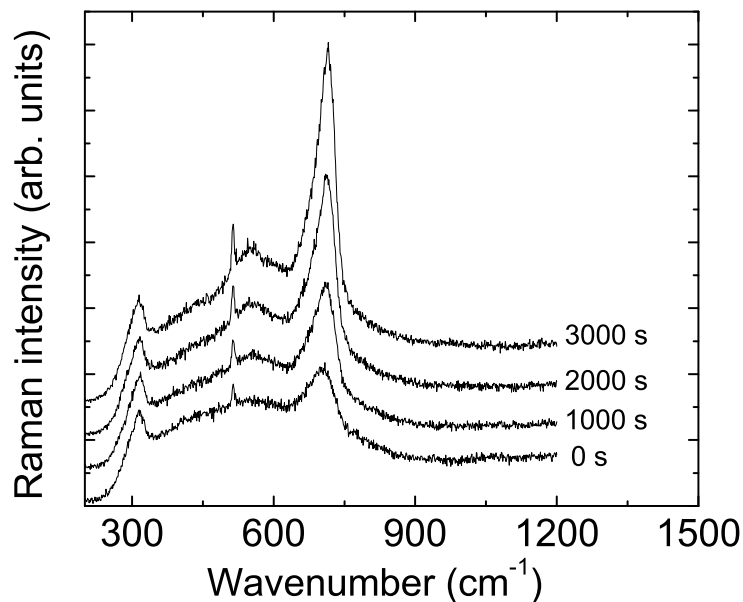


Figure 6.13: Time-dependent UV Raman spectra of GaMnN5 with 6.4 at. % Mn. The Raman peak at  $710\text{ cm}^{-1}$  sharpens, shifts to higher frequencies by  $12\text{ cm}^{-1}$  and increases in peak area by  $2.8\times$  after 3000 seconds of UV laser exposure. Spectra have been shifted vertically for clarity.

380% of the initial spectrum. The peak has also shifted to higher frequencies, from  $710\text{ cm}^{-1}$  to  $722\text{ cm}^{-1}$ , after UV exposure. Additionally, the peak at  $520\text{ cm}^{-1}$  originating from the Si substrate has become more prominent, signifying the film has become more transparent to 325 nm light. These effects are considerably weakened in films with higher Mn contents of 9-10 at. %, and are not visible in the film with 18 at. %. The changes signify that the GaMnN is undergoing a reconstruction process facilitated by the UV laser. These effects can be explained in reference to the effect of annealing on  $nx$ -GaN films.

Annealed  $nx$ -GaN films exhibit a sharpening of the Raman peaks and a shift to higher frequencies [199] of a similar magnitude to that seen in the UV-exposed GaMnN, as well as an increase of the peak intensities. In the annealed  $nx$ -GaN films, these effects are attributed to the healing of stacking faults and the subsequent removal of band-tail states, which steepens the onset of absorption. This brings the films closer to the res-

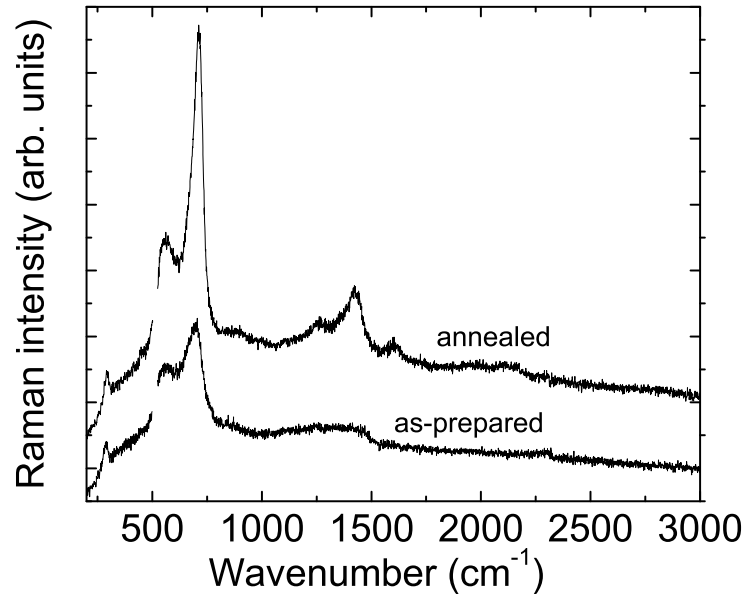


Figure 6.14: Raman spectra of GaMnN containing 6.4 at. % Mn before and after annealing for 1 hour in 10 mbar  $N_2$  at 400 °C. Note the emergence of higher order peaks at  $\sim 1245 \text{ cm}^{-1}$  and  $1440 \text{ cm}^{-1}$  after annealing, and the similarity of the changes in first order modes to those in the UV-exposed film of Figure 6.13.

onant Raman condition of the 325 nm laser light on  $nx$ -GaN films. Also seen in Raman spectra of the annealed  $nx$ -GaN films is the emergence of higher order modes, up to third order. Although Raman spectroscopy was not performed on the UV-exposed sections of the GaMnN films at high enough frequencies to identify the emergence of any higher order modes, note that a GaMnN film annealed for 1 hour at 400 °C under 10 mbar of  $N_2$  gas shows the same changes as in Ref. [199], and clearly shows higher order modes emerging (Figure 6.14). The time-dependent UV-induced effects are much weaker in the annealed GaMnN film, as the annealing has already partially reconstructed the film prior to UV exposure. Clearly the effect of annealing or UV exposure on GaMnN films is similar to that of annealing on  $nx$ -GaN films. The UV or annealing treatment heals stacking faults within the GaMnN crystallites, which sharpens the onset of optical absorption in the films. However, the Raman spectra of such recon-

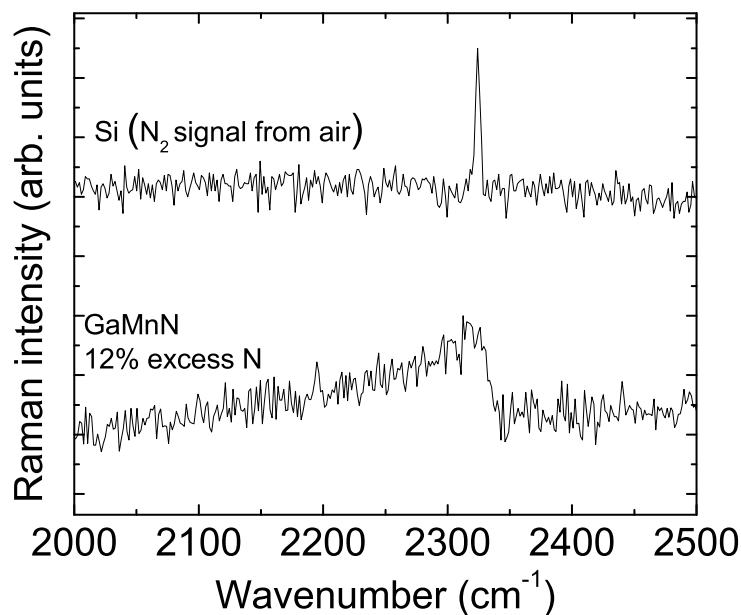


Figure 6.15: 514 nm excitation energy Raman spectrum of GaMnN film containing 12 % excess N (lower plot). The upper plot shows the spectrum of atmospheric N<sub>2</sub> above a clean Si substrate. The excess N is in the GaMnN film in the form of N<sub>2</sub> molecules that weakly interact with the film.

structed GaMnN films are still weaker than those taken from annealed *nx*-GaN films, indicating that the Mn incorporation has an important effect as well. Additionally, the UV-induced effect is smaller but still present in the annealed GaMnN, making it clear that the reconstruction is not complete. There is also no UV-induced enhancement of the Raman spectrum in *nx*-GaN, which confirms this particular effect is associated with the incorporated Mn. The UV-induced reconstruction may involved a re-ordering of Mn-related defect states, but the exact process is certainly complicated and is likely to be difficult to separate from the annealing-induced effect seen in both *nx*-GaN and GaMnN films.

Also visible in the Raman spectra is a low intensity peak broadened to frequencies below  $\sim 2330 \text{ cm}^{-1}$  (Figure 6.15). This peak is present in all GaMnN films that have an excess of N over Ga + Mn, and the same peak in *nx*-GaN has been shown using XANES to correspond to molecular N<sub>2</sub>

present in the films [198, 200]. The presence of this peak in GaMnN confirms that the excess N detected in RBS and NRA compositional analyses is also in these films in the form of molecular N<sub>2</sub>.

## 6.3 MnN

### 6.3.1 Composition

The composition of the MnN films was analysed using RBS and NRA techniques and the films were found to consist of 50 at. % Mn and 50 at. % N within experimental resolution, distributed uniformly throughout the film. O content is determined to be small, within the RBS uncertainty of 1-2 %. XANES measurements show that molecular N<sub>2</sub> is present in the films (Figure 7.12), which adds some uncertainty to the conclusion based on the RBS results. However, a comparison of the relative intensity of the XANES N<sub>2</sub> peak with similar peaks seen in IAD *nx*-GaN films [200] reveals that the proportion of N in molecular N<sub>2</sub> form is within the RBS uncertainty. The RBS measurements indicate that the MnN films are stoichiometric to within the experimental resolution, and that any excess N is in the form of N<sub>2</sub> molecules. The SIMS sputtering yields of Mn and N in MnN (Figure 6.16) are constant throughout the film, and the O yield is very low. The top 20 nm of the film has partially oxidised, with a large increase in O yield accompanied by reduced Mn and N yields. This shows that the small amount of O that is present is almost entirely due to partial oxidation at the film surface only.

### 6.3.2 Structure

To determine the structure of the films, XRD was performed at grazing incidence and EXAFS measurements carried out. The XRD pattern is shown in Figure 6.17, and shows only peaks originating from the distorted rock-salt MnN phase. Debye-Scherrer fitting of the width of the strongest (111) peak indicates an average crystallite size of 8 nm. At that crystallite size it is not possible to resolve the (200) and (002) or (220) and (202) peaks

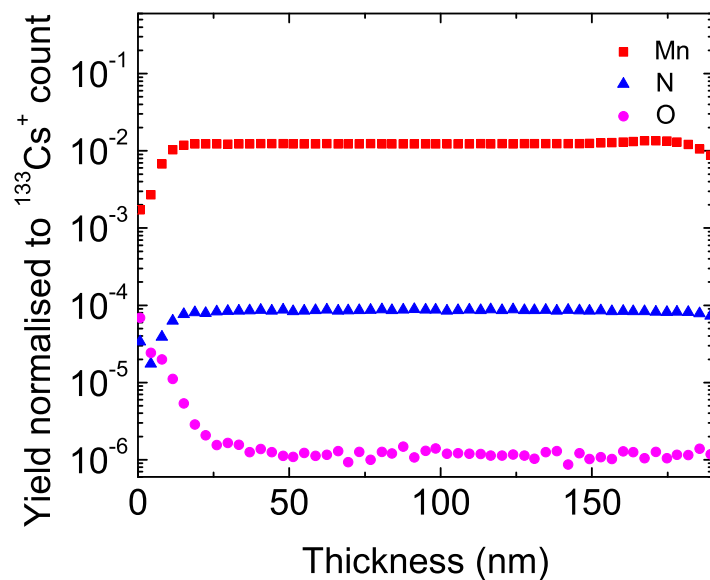


Figure 6.16: Normalised SIMS sputtering yields for MnN.

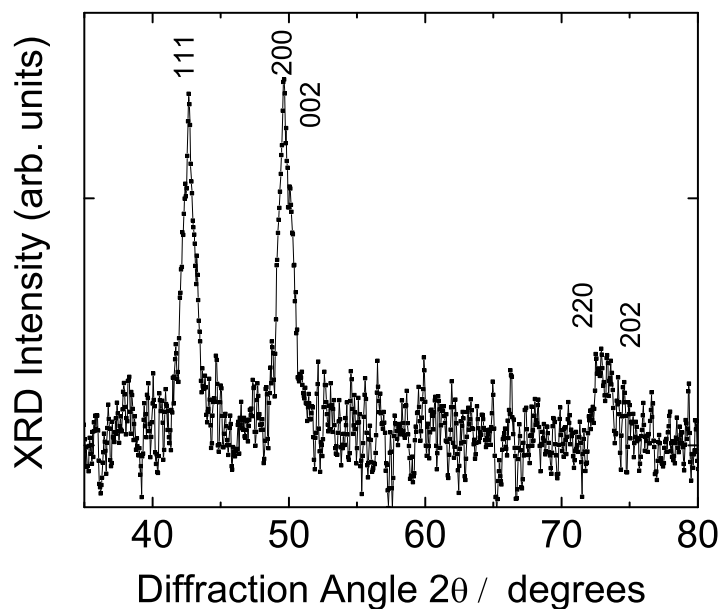


Figure 6.17: XRD pattern of a MnN film fabricated by ion-assisted deposition, demonstrating the nanocrystalline distorted NaCl structure. Peaks are labelled with their corresponding Miller indices. Note the asymmetry in the peaks, indicating the distortion of the cubic structure.

	This work	Suzuki <i>et al.</i> (Ref. [133])
$a$ (Å)	4.195	4.256
$c$ (Å)	4.195	4.189
$c/a$	1	0.9843
$d_{Mn-N}$ (Å)	2.098	$2.128(a)/2.095(c)$

Table 6.3: Fitted EXAFS parameters for MnN.

fully, but the clear evidence of an asymmetry in these features confirms the presence of a distortion along the  $c$  axis, as expected for MnN. The peak positions are in full agreement with the unit cell dimensions for distorted rocksalt MnN, further confirming the 1:1 Mn:N stoichiometry. In particular note that there is no evidence at all of peaks of  $Mn_3N_2$ , a common secondary phase in MnN [167, 201].

Figures 6.18 and 6.19 show the Mn  $K$ -edge EXAFS pattern and the pseudo-rdf for the first four nearest-neighbour shells extracted from an x-ray absorption spectrum taken at 77 K, from Ref. [188]. The parameters obtained from the fit (solid lines in Figure 6.18) are compared in Table 6.3 with the crystalline values reported at room temperature [133]. The EXAFS, which has been simulated using a single peak, is used to fit each shell (i.e. a cubic rocksalt structure is assumed) and the fitted lattice constant is found to be 4.195 Å, intermediate between the  $a$ - $b$  (4.256 Å) and  $c$  (4.189 Å) axis lattice constants of tetragonal MnN. Thus, the results show only MnN to be present, with the interatomic distances and the number of ions within the shells consistent with the expected values. Note, however, that two very closely spaced shells would not be resolved in the EXAFS, preventing detection of the noncubic distortion seen in XRD.

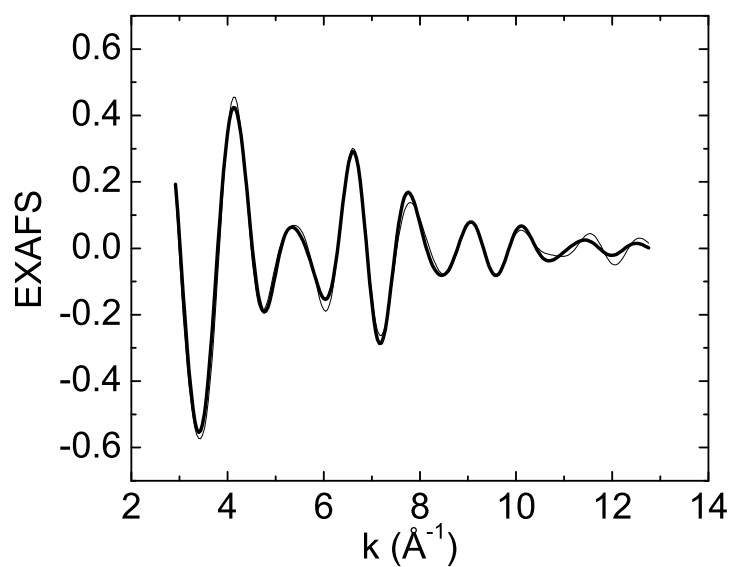


Figure 6.18: EXAFS of a MnN film. The thicker line is a best fit to the data.

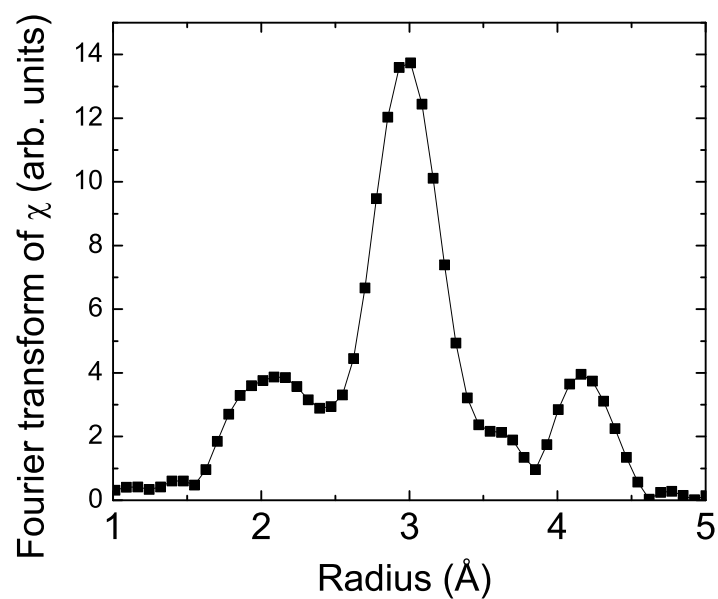


Figure 6.19: Fourier transform of the MnN EXAFS from Figure 6.18, showing the first four nearest-neighbour positions. The squares are the experimental data, the line is a guide to the eye. Phase correction has been applied so the radii values are real.



## 6.4 Summary

### 6.4.1 GaMnN

GaMnN films have been prepared with a range of Mn concentrations (4-18 at. %) and an excess of N in the form of N<sub>2</sub> molecules that weakly interact with the GaMnN material. The films are uniformly nanocrystalline with a random-stacked structure of wurtzite and zincblende GaN sequences. An expansion of the lattice parameter with increasing Mn content indicates that the Mn is predominantly incorporated substitutionally on the Ga lattice site in the Mn<sup>2+</sup> oxidation state. There is no indication of phase segregation or Mn-clustering, and the short-range atomic environment around both the Mn and Ga atoms qualitatively resembles that around Ga in GaN in the wurtzite or zincblende phase. A small expansion of the Mn-N bond length is in agreement with the observed lattice parameter increase. The experimental pseudo-rdfs show significant differences from that simulated for other potential phases GaMn<sub>3</sub>N and Mn<sub>4</sub>N. The optical, electronic and magnetic properties reported in Chapter 7 will thus be characteristic of single-phase nanocrystalline GaMnN films grown through IAD. A UV-induced partial reconstruction of the structure in GaMnN films with less than 10 at. % Mn is observed from time-dependent changes in the Raman spectra, and has a similar effect to that produced by annealing these films or *nx*-GaN. At higher Mn concentrations the condition for resonant Raman scattering when using a 3.8 eV excitation source is lost, and comparison with the optical absorption in Section 7.1.2 confirms this is due to the extra Mn broadening the onset of absorption in the GaMnN films.

### 6.4.2 MnN

MnN films were prepared with a 1:1 Mn:N ratio and were found to be comprised of 8 nm nanocrystals in the distorted NaCl structure previously observed for stoichiometric  $\theta$ -phase MnN. No sign of alternate Mn<sub>*x*</sub>N<sub>*y*</sub> phases is seen in XRD, and the EXAFS results confirm that the lattice parameter and coordination numbers of the first few shells neighbouring Mn atoms are in agreement with this structure. Due to the small size of the

nanocrystals, the shortening of the  $c$  axis is not able to be distinguished in the EXAFS, although an asymmetry in the XRD (002) peak indicates that this strain on the NaCl structure is present in these films.





## Chapter 7

# Electronic, optical and magnetic characteristics

In this chapter the DC electrical resistivity, optical absorption and magnetic character of the GaMnN films will be investigated. The DC electrical resistivity, optical conductivity and magnetic character of MnN will also be investigated. XANES and XES measurements and the optical conductivity results will be interpreted on the basis of calculations of the band structure and PDOS for MnN performed elsewhere.

### 7.1 GaMnN

#### 7.1.1 DC electrical resistivity measurements

The DC electrical resistivity of GaMnN with varying Mn contents was measured as a function of temperature using the four-point probe technique described in Section 5.4 to remove effects from the contact resistance and sample leads. Measured resistivities range over four orders of magnitude ( $\sim 0.1$  to  $10^3 \Omega\text{cm}$ ) at ambient temperatures, strongly dependent on the Mn content. The temperature dependence of the resistivities likewise depends strongly on the composition of the films, but ranges from an increase of between  $\sim 2$  and  $2 \times 10^4$  times when cooling from 300 K to  $\sim 60$  K.

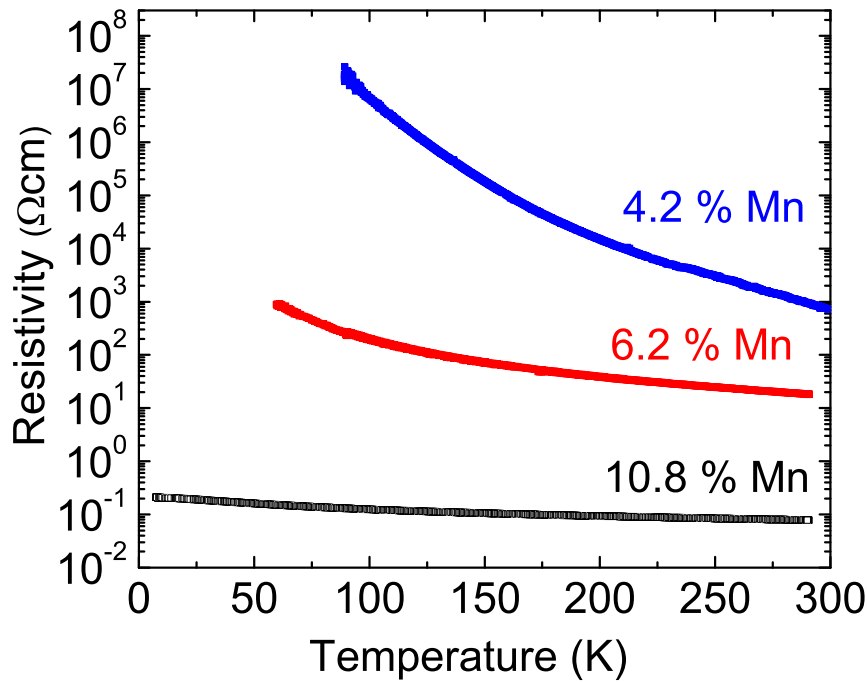


Figure 7.1: Temperature dependent resistivity of GaMnN films. Increasing the Mn content decreases the resistivity and the temperature dependence.

Before discussing the results of temperature-dependent resistivity measurements of the GaMnN films, it is useful to mention the behaviour of Mn-free films of IAD GaN and GaN:O. The room temperature resistivities of  $nx$ -GaN and amorphous GaN:O films have been previously observed to be between  $10^7$  and  $10^{11}$   $\Omega\text{cm}$  at 310 K [182]. The temperature behaviour above room temperature follows the exponential relation of Eq. 2.12 expected for semiconductors with an activation energy of  $\sim 0.80$  eV for  $nx$ -GaN and 1.03 eV for GaN:O [196].

The temperature dependence of resistivity for three films of GaMnN is plotted in Figure 7.1. The film with the lowest Mn content of 4.2 at. % has a resistivity of 943  $\Omega\text{cm}$  at 290 K, which is four orders of magnitude lower than the resistivity of Mn-free IAD films of GaN. There is a strong temperature dependence; the resistivity increases by over four orders of magnitude from 290 to 90 K. Resistivity measurements at lower temperatures were prevented by reaching the leakage current limit for the circuit.

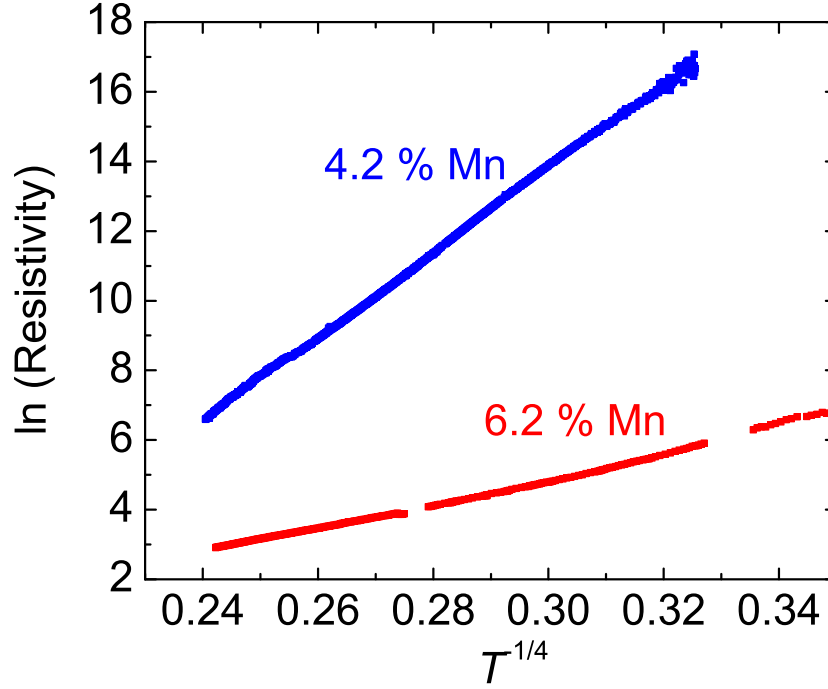
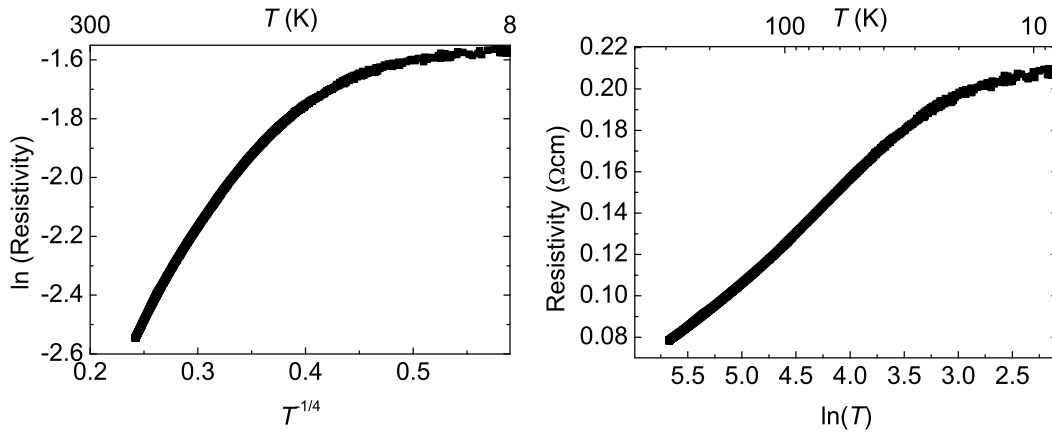


Figure 7.2: Check for variable range hopping in GaMnN films with Mn at 4 and 6 at. %. Resistivity follows  $\sim e^{T^{-1/4}}$  behaviour between 290 and 60 K.

In films with higher Mn contents of 6.2 at. % and 10.8 at. %, the room temperature resistivities are lower, with values of 18 and 0.08  $\Omega\text{cm}$  respectively at 290 K. The film with 6.2 at. % Mn has a resistivity factor increase of  $\sim 20\times$  from ambient to 90 K, considerably less than for the lower Mn content film. The film with 10.8 at. % Mn has an even weaker temperature dependence (increase of  $\sim 2\times$  from 290 K to 90 K). The origin of this change in resistivity and temperature-dependent behaviour can be explained with reference to the models of conduction in disordered semiconductors and metals described in Chapter 2.

Figure 7.2 plots the natural log of the resistivity versus  $T^{-1/4}$  for the 4.2 and 6.2 % Mn films. The relation between these values is linear, and shows that these films conform to the VRH model of conductivity. In Figure 7.3(a) the natural log of the resistivity versus  $T^{-1/4}$  for the 10.8 % Mn film is slightly sublinear over the same temperature range as the lower



(a) Check for variable range hopping.

(b) Check for weak localisation.

Figure 7.3: Temperature-dependent resistivity behaviour of a GaMnN film with 10.8 at. % Mn, plotted in two different ways.

Mn content films, and at lower temperatures the relation significantly departs from VRH behaviour. A more closely linear relationship is obtained over a wider range of temperatures between resistivity and  $\ln(T)$  in Figure 7.3(b) for the 10.8 % Mn film, which indicates that weak localisation is a better model for the resistivity behaviour at this Mn content. This shows the temperature-dependent behaviour of this film is closer to that of a disordered metal than a defective semiconductor.

VRH requires a mixture of filled and empty localised states at the Fermi level, so the conductivity behaviour at lower Mn concentrations supports the hypothesis of Chapter 6 that there is a mixed valency of  $\text{Mn}^{3+/2+}$  ions in the films. At lower Mn contents the Mn acts as an impurity in the GaN band structure. The majority Mn  $3d$  states are within the bandgap of GaN and are filled for the case of a  $\text{Mn}^{2+}$  ion, whereas  $\text{Mn}^{3+}$  has one unoccupied  $3d$  majority state. An electron can hop from a filled  $\text{Mn}^{2+}$   $3d$  state into the unoccupied  $3d$  level of a nearby  $\text{Mn}^{3+}$  ion, whereas hopping between  $\text{Mn}^{2+}$  ions alone is unlikely, due to the large energy gap between the filled majority and empty minority  $3d$  states. Incorporating more Mn into the films increases the density of impurity states in the GaN and decreases the resistivity as a result. However, the temperature-dependent



behaviour shows that the films still retain the electronic band structure of a semiconductor, as the VRH resistivity behaviour of the 6 at. % Mn film is still characteristic of a semiconductor with a high concentration of these localised states.

At a critical concentration of Mn, the impurity states will begin to overlap and form a band of their own, and the conductivity behaviour approaches that of a metal. The critical concentration of Mn that can be incorporated into *nx*-GaN through IAD without altering the semiconducting nature of GaN appears to be near 10 %. At concentrations of Mn above this amount the film will become more conducting and the resistivity more weakly temperature-dependent below ambient temperature, driving the transport characteristics towards the metallic regime.

### 7.1.2 Optical absorption

Figure 7.4 shows the optical absorption of several GaMnN films as a function of incident energy. Plotted in the same figure is the absorption of IAD *nx*-GaN. Near 4 eV the absorption for all Mn concentrations in GaN films approaches that of the Mn-free *nx*-GaN, although there are significant differences at energies lower than the 3.4 eV bandgap of the Mn-free films. The addition of Mn at 4.2 at. % greatly increases the absorption below the GaN absorption edge and significantly broadens the transition from absorbing to transparent in the films. Increasing the Mn content above this level as high as 11.7 at. % increases the in-gap absorption further, but does not alter the basic shape of the 4.2 at. % Mn film absorption curve. This suggests that Mn incorporated into the lattice adds electronic states within a certain energy range inside the bandgap, and adding more Mn broadens the states into an impurity band, but does not significantly affect the position of these impurity levels. The observed absorption behaviour is consistent with a mixed valency of the incorporated Mn. There are a range of spin-allowed optical transitions amongst 3*d* levels of Mn in the 3+ oxidation state and from both the Mn<sup>2+</sup> and Mn<sup>3+</sup> levels into the conduction and valence bands. Transitions involving the Mn levels are broadened in the nanocrystalline films, in contrast to the sharp peaks associated with

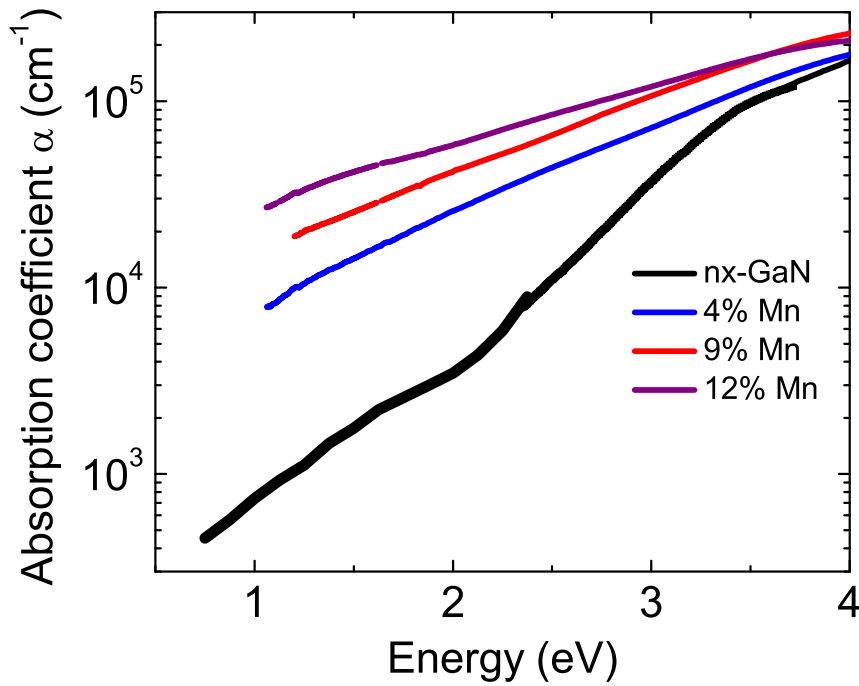


Figure 7.4: Combined optical absorption measurement of GaN and GaMnN films. The incorporation of Mn increases absorption over a broad energy range within the GaN bandgap.

certain Mn states in single crystalline films [143, 144, 148, 151]. The Mn levels are broadened in the nanocrystalline films, leading to broadened optical transition energies, resulting in absorption over the wide range of energies seen.

The formation of impurity levels inside the bandgap that then broaden into a band at higher Mn contents is consistent with the low temperature resistivity behaviour. At lower Mn contents, the  $\text{Mn}^{3+/2+}$  impurity levels are over a large enough spread in energy space to give rise to the absorption seen over a range of sub-bandgap energies, but still sparse enough that the DC electrical conductivity behaviour is like that of a defective semiconductor. As the Mn content is increased, the additional impurity levels cover the same energy range, but become more densely spaced, allowing for the formation of a band as the levels overlap. In films with very large Mn contents, conduction starts to occur within the impurity band it-

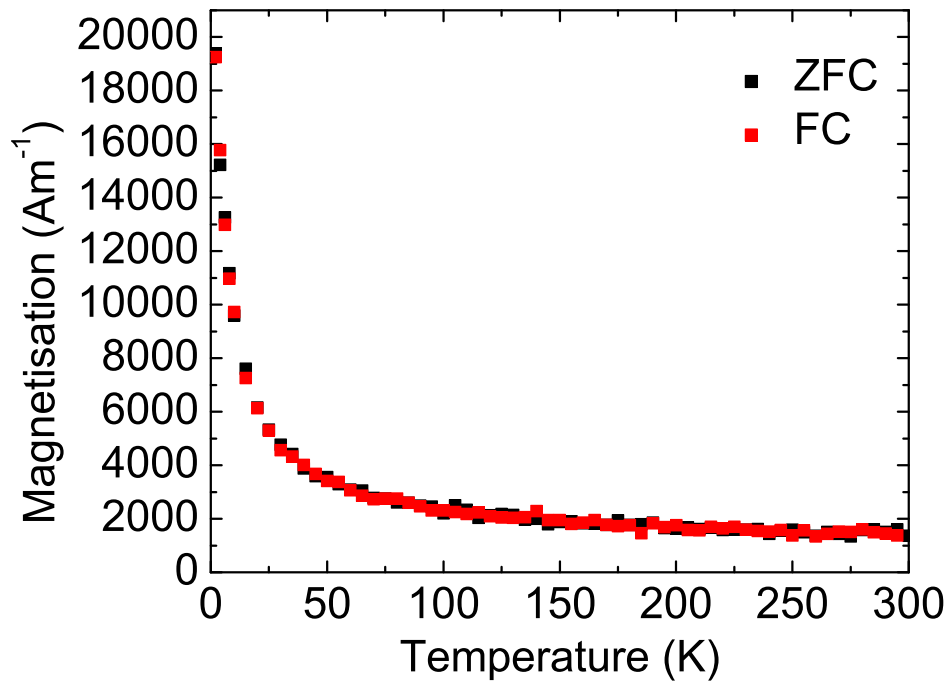


Figure 7.5: Magnetisation of a GaMnN film with 4.3 at. % Mn measured in 1 T. Black points are from the zero-field cooled measurement, red points from the field cooled measurement.

self, and the DC resistivity behaviour approaches that of a metal, since there is a large density of states available within the impurity band.

### 7.1.3 Magnetic properties

The magnetic properties of GaMnN films have been investigated using a SQUID magnetometer. Figure 7.5 shows the ZFC and FC measurements performed in a field of 1 T for a film with 4.3 at. % Mn. The increase of magnetisation as temperature is decreased resembles a paramagnetic material, and no sign of a step-like ferromagnetic transition is seen. The measurements are reversible, i.e. the ZFC and FC measurements overlap over the full temperature range, from 300 K to 2 K. The temperature dependence is similar for loops performed in 100 mT or 6 T fields, with lower or higher magnetisation values respectively. However, the value

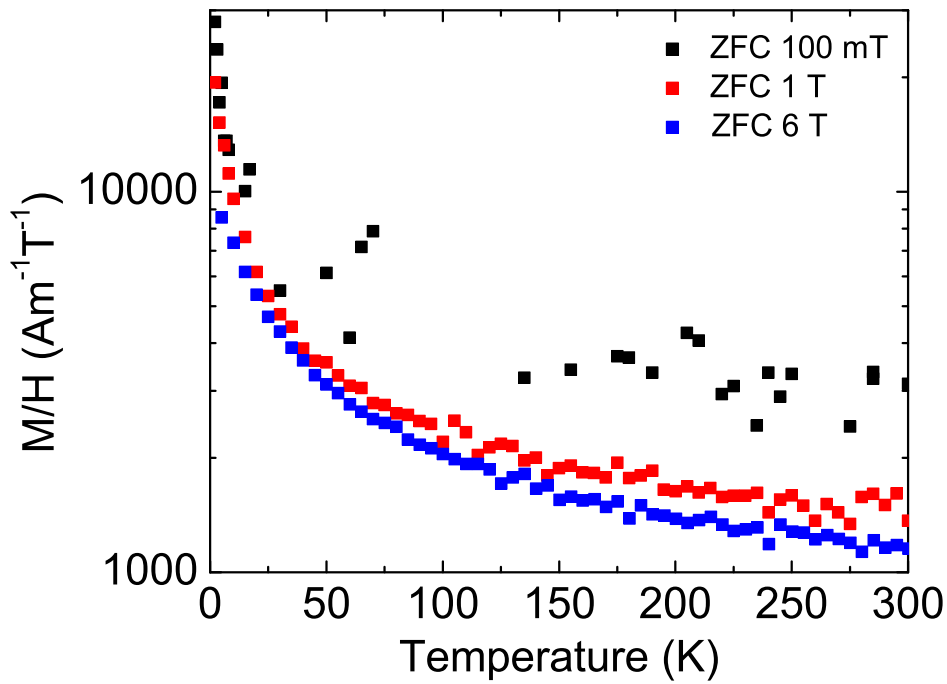


Figure 7.6: ZFC magnetisation of a 4.3 at. % Mn GaMnN film measured in various strengths of applied field, normalised to the field.

of the magnetisation does not scale with the strength of the field. In Figure 7.6,  $M/H$  from ZFC measurements on this film decreases over the entire temperature range as the applied field is increased from 100 mT to 6 T. There are two possible explanations for this trend of a larger applied field producing a smaller magnetisation per unit field. The first is the tendency towards saturation of the total magnetic response at all temperatures for fields above 100 mT, although as will be shown the magnetic field-dependent behaviour is far from significant saturation in these fields even at low temperatures. The second possibility is that there is a coexistence of phases which includes a small phase that saturates at lower fields. GaMnN films with 9 at. % Mn show the same trend in  $M/H$  versus  $T$ , over the entire range of temperature values measured.

Magnetisation measurements as a function of field were performed at low temperatures on these films to investigate the possibility of magnetic saturation or hysteresis. Figure 7.7 shows the  $M$ - $H$  curves measured at 5

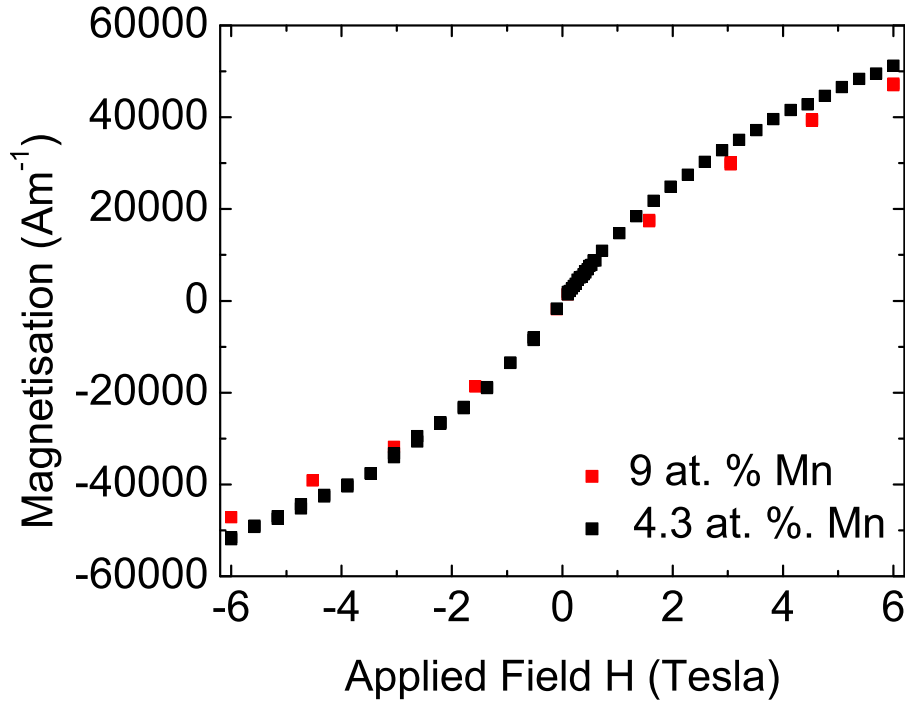


Figure 7.7: Field-dependent magnetisation loops of GaMnN films at 5 K.

K for films with both high and low Mn contents. There is no sign of a full saturation of the net magnetic response in fields as high as 6 T, nor is there a hysteresis or remanent magnetisation in the field loops for either film, ruling out the presence of a significant ferromagnetic phase. Note that the magnetisation measured for the 9 at. % film is actually slightly smaller than for the 4.3 at. % film in all applied fields, despite this film containing over twice the Mn content. As will be shown, these field and temperature dependent measurements together are consistent with a paramagnetic-like phase dominating the magnetisation behaviour in the films, with a minority component from a low-field saturating phase. A coexistence of magnetic phases in DMS is not uncommon [93, 158].

Quantitative analysis of the magnetisation behaviour of both films has been carried out as per the theoretical description of Section 2.1. Modelling the temperature-dependent behaviour with Curie's law does not result in satisfactory fits, but satisfactory fits are obtained with the Curie-Weiss law, valid in the case that the exchange between moments can be

Film	Mn content (at. %)	Field (T)	$\theta_p$ (K)	fitted $T$ range (K)
GaMnN8	4.3	1	$-7.4 \pm 6.6$	0-300
		6	$-13.5 \pm 3.0$	0-300
GaMnN9	9	1	$-20.5 \pm 3.4$	0-300
		6	$-21.2 \pm 3.4$	0-300

Table 7.1: Curie-Weiss law fitting results for GaMnN films. The apparent Curie temperature  $\theta_p$  is negative in all cases, indicating antiferromagnetic correlations in the film.

well represented by a mean field, resulting in a non-zero  $\theta_p$  value. Table 7.1 summarises the results from these Curie-Weiss law fits. The measurement data taken at both 1 T and 6 T applied fields was well modelled over the full temperature range for both films. The fits returned values of  $\theta_p$  that were negative in all cases. An increase of applied field or Mn content results in a larger negative value for  $\theta_p$ . The negative  $\theta_p$  provides evidence that there is antiferromagnetic exchange in the films, and that at larger applied fields the effect of this exchange is more pronounced. The value of  $p_{\text{eff}}$  extracted from the fits to the 4.3 at. % film is  $4.40 \pm 0.06$  in both fields, which compares well with expected values for a free Mn ion (4.0-5.9) [25]. A reasonable value for  $p_{\text{eff}}$  was not extracted from the fit to the 9 at. % Mn film ( $p_{\text{eff}} = 0.87 \pm 0.01$ ). This is not unexpected, as the greater density of Mn in this film may violate the Curie-Weiss law assumption that the exchange interactions between magnetic ions can be represented as a mean field. Small fluctuations in the local Mn density at larger Mn concentrations would mean that the net exchange at individual Mn sites would vary over the film, invalidating a mean-field analysis. The Curie-Weiss law fitting results provide further evidence for the conclusion that there is a coexistence of a dominant near-paramagnetic phase and a smaller saturating phase. The Curie-Weiss analysis suggests that the non-paramagnetic phase is associated with antiferromagnetic exchange. The simultaneous presence of paramagnetic and antiferromagnetic phases has

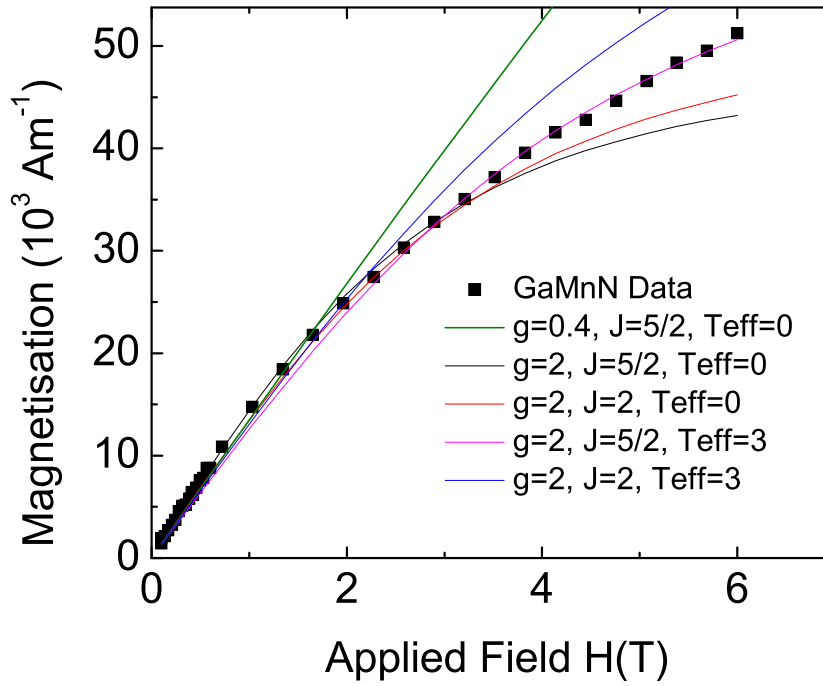


Figure 7.8: Brillouin function fitting to M-H dependence of GaMnN with 4.3 at. % Mn. The measurement was made at 5 K. The best fit corresponds to  $S = (J =) 5/2$  ( $\text{Mn}^{2+}$  ions) with a correction for a coexisting antiferromagnetic phase.

been determined in GaMnN films before [93, 162].

Further support for a minority antiferromagnetic contribution to the magnetisation becomes evident with a Brillouin function fit to the M-H behaviour of the films. Figure 7.8 shows Brillouin function fits to the M-H behaviour of the 4.3 at. % Mn film. Fitting the curvature of the M-H loop is impossible using the values of the Landé  $g$  factor calculated for the free Mn ion in any oxidation state but for  $\text{Mn}^{2+}$ , where  $g = 2$ . However, it is known that crystal field effects on the splitting of levels such as the  $3d$  states in Mn can cause a quenching of the orbital angular momentum component of the magnetic moment [25]. In these cases,  $g = 2$  regardless of the spin state of the ion and the effective total electronic angular momentum  $J$  is comprised of the spin contribution  $S$  only. It is possible to fit the measured data well for low ( $< 3$  T) fields using values of  $J = 5/2$  or  $J = 2$ , although

at higher field strengths there is a significant misfit.

Reasonable fits over the full range of applied fields used can be obtained using an adjusted Brillouin function that considers an effective temperature  $T_{\text{eff}}$ . As outlined in Ref. [162],  $T_{\text{eff}} = T + T_0$ , where  $T$  is the measurement temperature and  $T_0$  arises due to a proportion of Mn ions that do not have a field-dependence of magnetisation well modelled by the Brillouin function.  $T_0$  reflects a proportion of Mn ions that are locked together through exchange coupling, and these Mn ions respond less effectively to an applied magnetic field than non-interacting moments. Now the magnetisation behaviour is modelled with

$$M(H, T) = Ng\mu_B JB_J(H, T_{\text{eff}}), \quad (7.1)$$

where  $T_{\text{eff}}$  is an indication of the strength of the exchange-coupled contribution. This modification to the Brillouin function is justified considering the indication of antiferromagnetic interactions derived from the Curie-Weiss law fitting of the temperature dependence of magnetisation, and of the indication of a saturating component from the  $M/H$  versus  $T$  measurements. The best fit is obtained over the full range of fields using this adjusted Brillouin function with  $J = 5/2$ , which corresponds to the  $\text{Mn}^{2+}$  oxidation state. A reasonable fit is also obtained with  $J = 2$ , so the magnetisation result alone cannot unambiguously determine the state of the magnetically active Mn ions, or of the potential presence of Mn in both  $2+$  ( $J = 5/2$ ) and  $3+$  ( $J = 2$ ) oxidation states. However, further analysis of the results assuming all the magnetically active Mn is in the  $\text{Mn}^{2+}$  oxidation state will be informative, and analysis in terms of  $\text{Mn}^{3+}$  ions would be similar. For the  $J = 5/2$  best fit function,  $T_{\text{eff}} = 8$  K. The 3 K difference from the actual measurement temperature of 5 K is comparable to the values of  $T_0$  reported in Ref. [162] for films with similar Mn content. The value of  $N$ , the number of Mn atoms contributing to the field dependent behaviour, is calculated to be  $1.96(\pm 0.04) \times 10^{17}$  for the best fit. This value is reasonable considering the total number of Mn atoms incorporated into the film is estimated at  $2.6 \times 10^{17}$ , calculated from the volume of the film, the density and molar density of wurtzite GaN and the concen-



tration of Mn of 4.3 at. % from the IBA analysis of Section 6.2.1. Thus 75% of the total incorporated Mn contributes to the paramagnetic temperature dependence of the magnetisation, and this value is in excellent agreement with the Curie-Weiss law fitting result of  $p_{\text{eff}} = 4.4$  per Mn ion, considering this number is equivalent to a system of  $\text{Mn}^{2+}$  ions ( $p_{\text{eff}} = 5.9$ ) where 25% do not contribute to the magnetisation. This remaining 25 % of the Mn can be considered the proportion that provides the non-paramagnetic component, leading to the negative  $\theta_p$  value and the  $T_{\text{eff}}$ . As has been stated, the likely presence of Mn in both 2+ and 3+ oxidation states complicates the above analysis if the crystal field quenching effect on the orbital angular momentum is significant, and an accurate determination of the ratio of these oxidation states is needed for a more precise analysis.

The field loop for the 9 at. % Mn film closely resembles the curvature of the 4.3 at. % film (Figure 7.7), and a good fit is obtained with the adjusted Brillouin function and  $J = 5/2$  once again. Despite a factor of 2.1 increase in the Mn content of this film, the magnitude of the magnetisation at 5 K is slightly smaller than that of the lower Mn content film over the full range of applied fields. The significance of this is that the additional Mn appears not to contribute to the paramagnetic-like magnetisation. Below a critical separation, two Mn ions are expected to experience antiferromagnetic exchange, and the random distribution of Mn on the Ga sites in the low Mn content film means that  $\sim 25$  % of the Mn experiences this exchange. At higher Mn concentration, the average distance between Mn ions is smaller, and a larger proportion of the total Mn content is locked into antiferromagnetic correlations with nearby Mn neighbours. This explains the tendency of  $\theta_p$  to increase with increasing Mn content; a larger proportion of the total Mn content experiences the antiferromagnetic exchange, which enhances  $\theta_p$ .

Note from Figures 7.5 and 7.6 that at ambient temperatures a measurable magnetisation of the order of  $1400 \text{ Am}^{-1}$  persists in all applied fields for the 4.3 at. % Mn film. Using the value for  $N$  derived from the Brillouin function fitting at 5 K, the magnetisation expected at 300 K from purely paramagnetic Mn ions would be  $\approx 340 \text{ Am}^{-1}$ , insufficient to explain the full ambient temperature magnetisation. Other studies have taken such

a phenomenon to be evidence of room temperature ferromagnetism in GaMnN [154, 158]. However, in all of these cases a remanent magnetisation was observed in the field loops at room temperature, and no such remanence is seen as low as 5 K in these films (Figure 7.7). This small room temperature magnetisation can be explained as due to the 25 % of the total Mn content that does not participate in the field-dependent magnetisation behaviour observed at 5 K, when considering a spin canting effect (see below) of the applied magnetic field on the antiferromagnetically correlated Mn ions.

The overall magnetic behaviour of the 4.3 at. % Mn sample can be interpreted as follows. In zero applied field the paramagnetic Mn moments are randomly oriented, and the Mn ions close enough to experience antiferromagnetic exchange align antiparallel relative to each other, resulting in a net zero magnetic moment. As a small magnetic field is applied, the paramagnetic Mn ions start to align as described by the Brillouin function Eqs. 2.5 and 2.6. The applied field also tilts or cants the antiferromagnetically correlated Mn ions slightly away from their antiparallel alignment so that they now have a net magnetic moment in the direction of the applied field. As the field increases in strength, the paramagnetic ions align with the field to a greater degree, while the moment of the spin-canted antiferromagnetic Mn nears saturation. The spin-canted antiferromagnetic phase explains the presence of a saturating positive component to the magnetic moment without hysteresis or a remanent moment as would be the case in the presence of a ferromagnetic phase. The large decrease of  $M/H$  at ambient temperature of Figure 7.6 when increasing the field from 100 mT to 1 T ( $\sim 3000 \text{ Am}^{-1}\text{T}^{-1}$  to  $\sim 1500 \text{ Am}^{-1}\text{T}^{-1}$ ) when compared to the smaller decrease from 1 T to 6 T ( $\sim 1500 \text{ Am}^{-1}\text{T}^{-1}$  to  $\sim 1100 \text{ Am}^{-1}\text{T}^{-1}$ ) is a result of the saturation of the spin-canted component at lower fields. The small divergence from Brillouin-like  $M$ - $H$  behaviour caused by this low-field saturation of the spin-canted component allows the  $M$ - $H$  behaviour of Figure 7.8 to be modelled with a small  $T_{\text{eff}}$  that accounts for the less responsive Mn ions. At higher Mn concentrations, the dominant  $M$ - $H$  behaviour does not change, and the measured magnetisation in a given field is no larger than at lower concentrations (Figure 7.7). This is be-

cause the extra Mn contributes only to the spin-canted moment, which, at 5 K in the fields applied, is still dominated by the paramagnetic contribution to the total response. A greater proportion of the total Mn is in the antiferromagnetically-correlated spin-canted phase at higher Mn concentrations, which increases  $\theta_p$  derived from a Curie-Weiss law analysis, as shown in Table 7.1.

The real picture is likely to be that the Mn ions in the GaMnN films experience a near continuous range of interactions from antiferromagnetism to paramagnetism. However, treating the magnetisation as originating from a coexistence of only two phases, purely paramagnetic Mn or canted antiferromagnetic Mn, a quantitative analysis of the larger than expected observed room temperature magnetisation can be made. Even at 300 K the spin canted moments are not free to respond to thermal randomisation, implying the  $T_N$  of the antiferromagnetic Mn is above room temperature. The magnetisation for the number of  $J = 5/2$  Mn ions obtained from the Brillouin function fit for the 4.3 at. % Mn film is calculated for a field of 1 T at 300 K. The difference between this value and the measured magnetisation in 1 T at 300 K (from Figure 7.5) gives the contribution from the proportion of spin canted Mn ions. This corresponds to a moment of  $0.24 \mu_B$  per spin canted Mn ion. This number is reasonable in comparison with the moment of a free  $S = 5/2$  Mn ion ( $p_{\text{eff}} = 5.9$ ). The average canting angle between moments of  $5.9 \mu_B$  that would give rise to this moment is calculated to be  $177.7^\circ$ , compared to  $180^\circ$  for unconstrained antiferromagnetic alignment.

Figure 7.9 shows ZFC and FC magnetisation curves for a GaMnNO film containing  $\sim 19$  at. % Mn and 36 at. % O measured in a small field of 10 mT. There is a clear irreversibility below  $\sim 220$  K superimposed on the dominant paramagnetic-like behaviour. The field loop for this film at 5 K resembles those in Figure 7.7, showing no sign of hysteresis or remanence, which rules out a ferromagnetic origin of this irreversibility. The presence of an irreversibility in the ZFC-FC curve sequence is one of the fingerprints of spin-glass behaviour. A spin-glass is a material where frustration prevents the lowest energy state of a collection of magnetic ions from being achieved. Possible causes for this frustration include the pres-

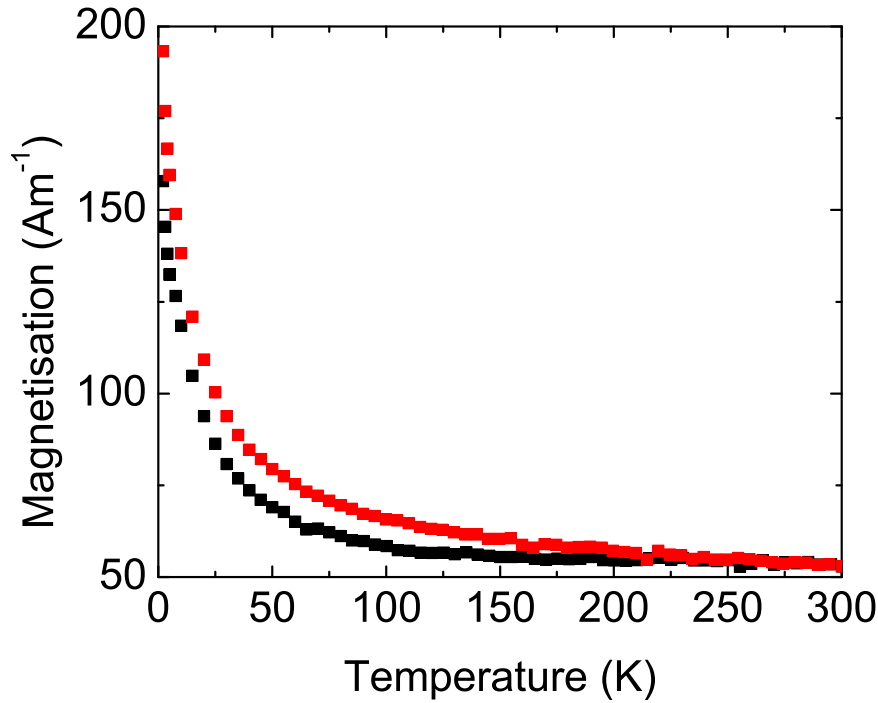


Figure 7.9: Magnetisation of GaMnNO film with 19 at. % Mn and 36 at. % O measured in 10 mT applied field. Black points are from the ZFC measurement, red points from the FC measurement.

ence of a range of differing strengths and signs of exchange interactions or geometric frustration of the lattice. With the very high Mn concentration in this film, a large proportion of the Mn ions will neighbour other Mn ions, leading to a complicated degree of exchange. Spin-glasses typically contain a variety of strengths and signs of exchange interaction, and it is possible there is even a contribution from ferromagnetically correlated Mn ions to the net magnetisation in this film. However, this would certainly be small if it was present, as no hysteresis or remanence was observed. On the other hand, O levels of 12 at. % have been shown to stabilise GaN in an amorphous structure [121], and the similarly high level of disorder expected in the GaMnNO film combined with a spin-canted antiferromagnetically-correlated phase may be sufficient to cause the observed spin-glass freezing temperature  $T_f$  of 220 K. The films with lower

Mn contents described earlier can be likened to spin-glass type materials, where the exchange-correlated ions are not well constrained down to low temperatures, since there is no separation between the ZFC and FC curves. Such a type of material is sometimes known as a spin liquid [202].

## 7.2 MnN

### 7.2.1 Electrical and optical conductivity properties

The DC resistivity, optical conductivity (calculated and measured) and XANES/XES measurements and interpretations included here were for the most part originally published in Granville *et al.* [188].

#### Experiment and comparison with band structure

Figure 7.10 displays the temperature dependence of the normalized resistivity of MnN. The room temperature resistivity is approximately  $135 \mu\Omega\text{cm}$ . The films are clearly metallic, though they show a high residual resistivity of more than  $100 \mu\Omega\text{cm}$  as expected for the very small crystallites in the films. The intrinsic temperature-dependent resistivity is similarly large, rising to  $25 \mu\Omega\text{cm}$  when the temperature reaches 300 K. The inset to Figure 7.10 shows a weak approximately logarithmic upturn below 30 K reminiscent of a Kondo anomaly, which is a feature usually associated with magnetic impurity scattering [203]. The upturn may result from a small proportion of non-stoichiometric material, or may be intrinsic to MnN, but the correct interpretation is not yet clear.

The measured spectral conductivity, obtained from a combination of ellipsometry and FTIR measurements (Figure 7.11, solid blue line), shows a conductivity that rises to  $7500 \text{ Scm}^{-1}$  at the lowest measured frequency, in good agreement with the DC value of  $7400 \text{ Scm}^{-1}$ . This behaviour is characteristic of an intraband metallic contribution, although the data do not fit well to the simple Drude expression

$$\sigma(\omega) = \frac{\sigma_{DC}}{1 + \omega^2\tau^2}. \quad (7.2)$$

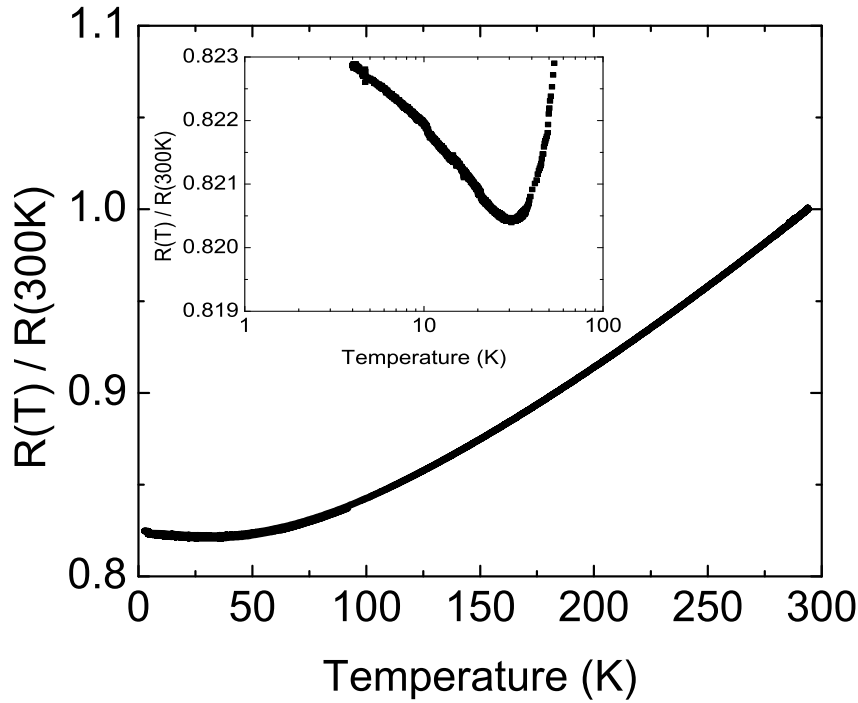


Figure 7.10: Normalized temperature dependent DC resistivity of MnN. The room temperature resistivity is about  $135 \mu\Omega\text{cm}$ . The inset shows the approximately logarithmic Kondo-like resistance anomaly observed at low temperature.

As discussed below there are significant low-frequency interband contributions which overlap the intraband conductivity. In particular, the calculated interband conductivity, (short dashed black line in Figure 7.11) shows a feature at  $1000 \text{ cm}^{-1}$  or  $0.13 \text{ eV}$ . Therefore, a Drude term, shown as a dotted green line, with  $\sigma(0) = 6000 \text{ Scm}^{-1}$  and  $\tau = 9.5 \times 10^{-13}$  seconds was subtracted so as to give approximate agreement between calculated and experimental  $\sigma$  in the region  $1200\text{--}2200 \text{ cm}^{-1}$ . The experimental spectrum after the Drude term subtraction, shown as a long dashed red line, then agrees remarkably well in absolute value and shape of the curve all the way up to about  $9000 \text{ cm}^{-1}$  or  $1.1 \text{ eV}$ . At frequencies above  $5000 \text{ cm}^{-1}$  ( $0.6 \text{ eV}$ ) the conductivity is dominated by interband transitions. In the mea-

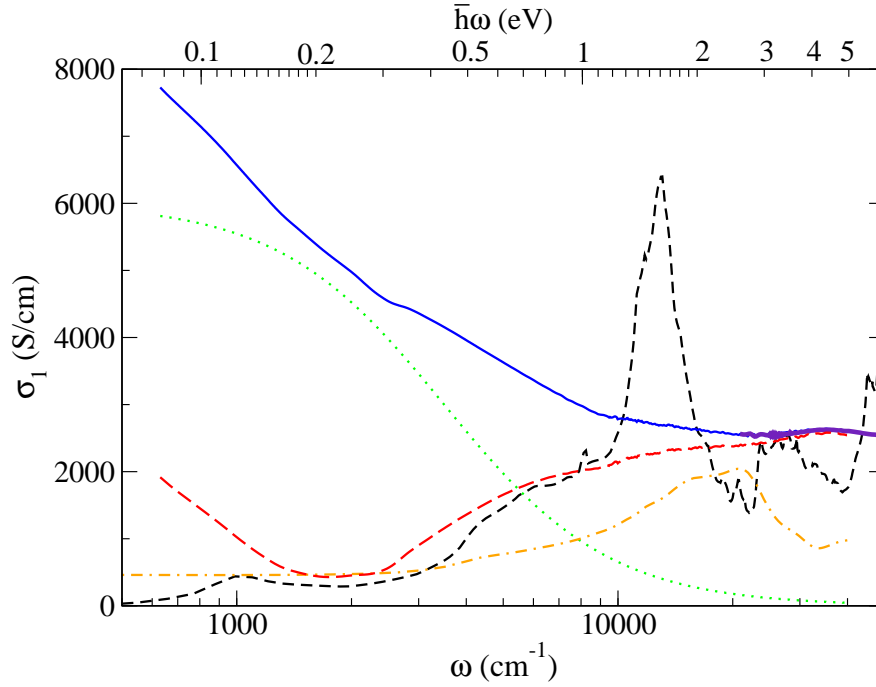


Figure 7.11: Optical conductivity as a function of wavenumber and photon energy (from [188]): Solid blue line experimental data obtained from reflectance and KK analysis in the infrared; indigo part at higher energy was obtained separately from SE in the UV, visible and near-infrared; short-dashed black line, calculated interband contribution to the conductivity; dotted green line, Drude expression with  $\sigma(0) = 6000 \text{ Scm}^{-1}$  and  $1/\tau = 3500 \text{ cm}^{-1}$ ; long-dashed red line, experiment with Drude interband contribution subtracted; dash-dotted orange line, convolution of empty and filled density of states multiplied by frequency and an arbitrary factor.

sured data these are signalled by features with maxima at  $14000 \text{ cm}^{-1}$  (1.7 eV) and  $32000 \text{ cm}^{-1}$  (4.0 eV). For comparison between the experimental and theoretical data the calculated interband contribution was averaged over both polarizations, corresponding to the sample's polycrystalline nature, i.e.  $\sigma_{av} = (2\sigma_{ab} + \sigma_c)/3$ .

The strongest peak in the calculation corresponds well in energy to the observed 1.7 eV experimental feature, and a second peak appears in the calculation at 3.4 eV, near to the measured feature at 4.0 eV. However,

as pointed out in Granville *et al.* [188], both features are much weaker and broader in the experiment than in the theory. The interpretation of the optical conductivity data is summarised below. There is substantial agreement in regards to the energy at which the structure occurs, but a severe disagreement in the strengths of the features, concluded to be due to the nanocrystalline structure of the films. The 1.7 eV peak corresponds to a strong peak in the joint DOS originating from nearly parallel, but not flat, bands across an extended portion of the Brillouin zone. The calculated conductivity is appropriate for fully crystalline material, and thus assumes vertical transitions, or strict momentum conservation. The films used in the experiment are comprised of crystallites of typically 8 nm diameter, and this degree of disorder would be expected to allow violation of the momentum conservation rule for optical transitions. Furthermore it is considered likely, given the high residual resistivity, that the carrier mean free path is limited by defects within the crystallites. Such defects have been detected for IAD-GaN [199] and IAD-GaMnN films (Section 6.2.2 of this work) as well. In the presence of such strong scattering the wavevector of both initial and final states will broaden, in turn broadening the interband absorption features. This argument considers the limit of an extremely short mean free path, corresponding to complete violation of the wavevector conservation rule. The conductivity then may have the form of a convolution of filled and empty sections of the DOS, multiplied by an arbitrary factor. The resulting form of the conductivity is plotted as the dashdotted orange line in Figure 7.11. This successfully accounts for the absence of the strong peak at 1.7 eV, although it clearly does not fully reproduce the shape of the measured conductivity. Moreover, recent optical measurements over 2-6 eV on single crystalline MnN films show close agreement with those from the nanocrystalline films of Figure 7.11, differing only in the sharpness of the broad peak at 4.0 eV [204]. The argument of limitations to the mean free path and the consequent violation of wavevector conservation does not apply to these structurally well-ordered [201] films, and other interpretations are needed to explain the differences between measured and calculated optical conductivities. One potential origin for the disagreement is that of the known difficulties in ap-



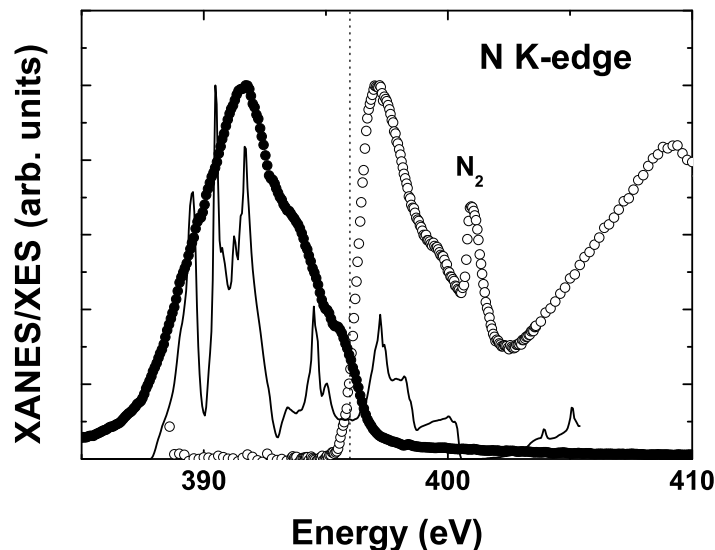


Figure 7.12: XANES (open circles) and XES (filled circles) spectra for N( $1s$ )-( $2p$ ) transitions representing empty and filled states respectively, compared to calculated N( $2p$ ) PDOS (solid line). The narrow peak at 401 eV is due to a small quantity of molecular N<sub>2</sub> trapped within the films (from [188]).

plying local density approximation (LDA) calculations to accurately locate both the valence and conduction bands. Additionally, LDA is not easily applicable to correlated electron systems such as those involving transition metal  $3d$  states [205, 206], and additional corrections to the position of bands are necessary in the case of e.g. LDA band structure calculations for GaMnN.

### 7.2.2 X-ray absorption and emission spectroscopies

Figure 7.12 displays both XANES and XES results for N  $K$ -edge transitions, representing the filled (XES) and empty (XANES) N( $2p$ ) PDOS, reproduced from Granville *et al.* [188]. The XES spectrum was obtained using 419 eV excitation. Note that these techniques do not assign an absolute scale to the PDOS function, and the two sets of results have simply been

normalized to their peak values. On the other hand their energy scales are well-calibrated so that a common Fermi energy for the MnN is clearly seen at 397 eV (relative to the  $1s$  level), where the XES (filled) DOS falls to zero and the XANES (empty) DOS rises rapidly. The figure also shows the PDOS as predicted by the calculated band structure. The agreement in peak positions is reasonable, taking into account the broadening of the experimental results due to both experimental resolution effects and the nanocrystallinity of the sample and the fact that no matrix element energy dependence was taken into account in the calculations. The additional peak at 402 eV in the XANES data is the  $\pi^*$  resonance of a small density of trapped molecular  $N_2$  in the films, as also seen in other IAD-grown films [200, 207]. A corresponding  $N_2$   $3\sigma_g$  resonance was also observed in the XES spectrum when the excitation energy was resonant with the  $\pi^*$  absorption (i.e.  $E_{ex} = 401$  eV). The presence of these two features with well-known energies [208] allowed an excellent confirmation of the energy calibration, and the overlap of the XANES and XES at the Fermi level correctly reproduces the metallic character of MnN.

Figure 7.13 shows XANES results from the Mn( $2p$ ) core level. In this case the PDOS is reproduced some 12 eV above the first edge, representing the spin-orbit splitting of the  $2p_{1/2}$  and  $2p_{3/2}$  states (the  $L_2/L_3$  edges). Again the agreement with the calculated PDOS is reasonable in terms of peak positions. Both experiment and theory show two peaks followed by a shoulder spaced by about 1 eV. The intensities are not expected to match because matrix element effects were not included in the theory.

### 7.2.3 Magnetic properties

The ZFC magnetisation of MnN from 5-300 K in a field of 2 T is plotted in Figure 7.14. There was a paramagnetic-like increase of magnetisation as temperature was decreased, although this temperature-dependent component was of the same magnitude as the total magnetisation at room temperature, and at 5 K the magnetisation of MnN was less than 1/4 of the value of the GaMnN film containing 4.3 at. % Mn (Figure 7.5). Figure 7.15 shows that  $M/H$  for MnN decreased as the applied field  $H$  was in-

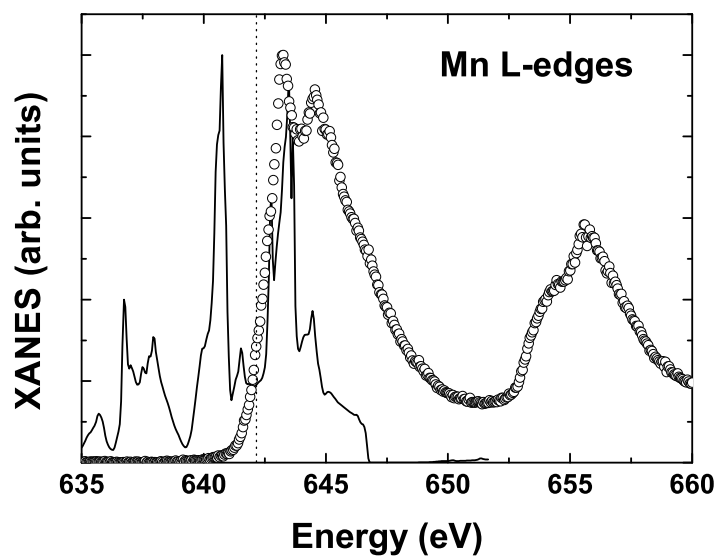


Figure 7.13: XANES for the  $\text{Mn}(2p_{3/2})$  core level (open circles) compared with the calculated  $\text{Mn}(3d)$  PDOS (solid line). The Mn  $L_2$ -edge ( $2p_{1/2}$ ) contributes the features above 652 eV (from [188]).

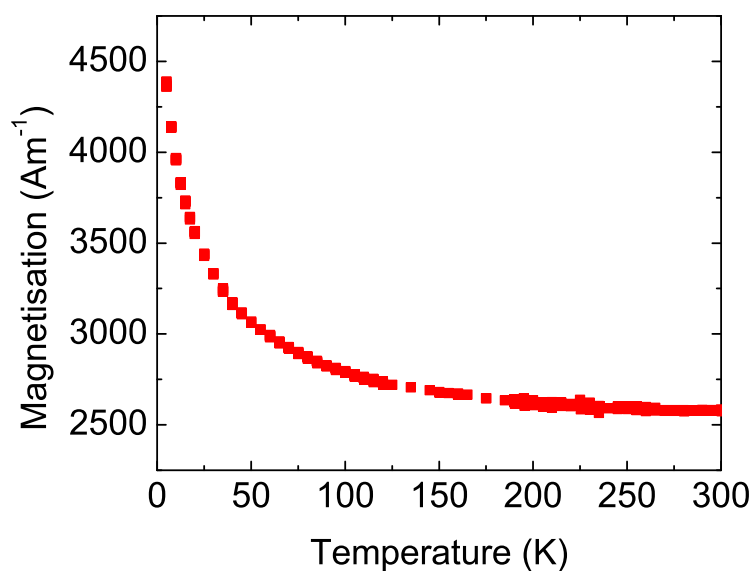


Figure 7.14: ZFC magnetisation of MnN measured in 2 T applied field.

creased. A similar trend was seen in the GaMnN films (Figure 7.6), and as in those films indicates either the onset of magnetic saturation at these fields or the presence of antiferromagnetic exchange. The field-dependent magnetisation of MnN in Figure 7.16 clearly indicates that saturation is not reached at fields of 5 T, and no sign of hysteresis was observed down to 5 K.

MnN has been reported to have a Neel temperature near 650 K [175], and neutron diffraction measurements [176] have shown antiferromagnetic ordering. Although there is a non-zero magnetisation in the MnN films at 300 K, this value corresponds to  $0.005 \mu_B$  per Mn in the largest field of 2 T. Suzuki *et al.* [176] reported a moment of  $3.2 \mu_B$  per Mn ion in MnN at 295 K, and assuming this moment the ambient temperature magnetisation in the MnN films corresponds to a contribution from 0.18 % of the total Mn.

Although the magnetic character has been measured at temperatures considerably lower than the reported MnN  $T_N$ , the temperature-independent component may result from Mn that does not fully participate in the antiferromagnetic alignment, and treating this Mn as magnetically 'free' allows an analysis based on the Curie-Weiss law. A possible origin for this magnetically 'free' Mn are the atoms at the grain boundaries, which may be less well magnetically coupled to the neighbouring atoms due to a reduced degree of structural order. Curie-Weiss law fitting to the temperature-dependent component results in  $\theta_p = -13.1 \pm 0.4$  K in a field of 25 mT and  $-15.5 \pm 0.2$  K in a field of 2 T. This, as well as the observation that an increasing applied field results in a lower magnetisation per unit field (Figure 7.15) indicates the Mn that responds to an applied field experiences negative exchange, and may experience some degree of spin canting, as seen in the GaMnN films. This may also support an antiferromagnetic state in the main part of the film. The coefficient of the Curie-Weiss law fit shows that for the magnetically 'free' Mn  $p_{\text{eff}} = 0.40 \pm 0.02 \mu_B$ . In light of this small value for  $p_{\text{eff}}$  the interpretation of the temperature dependence of magnetisation as resulting from a small fraction of magnetically 'free' Mn seems reasonable. It also suggests that this Mn may see the antiferromagnetic exchange, and the small remnant of magnetisation that results

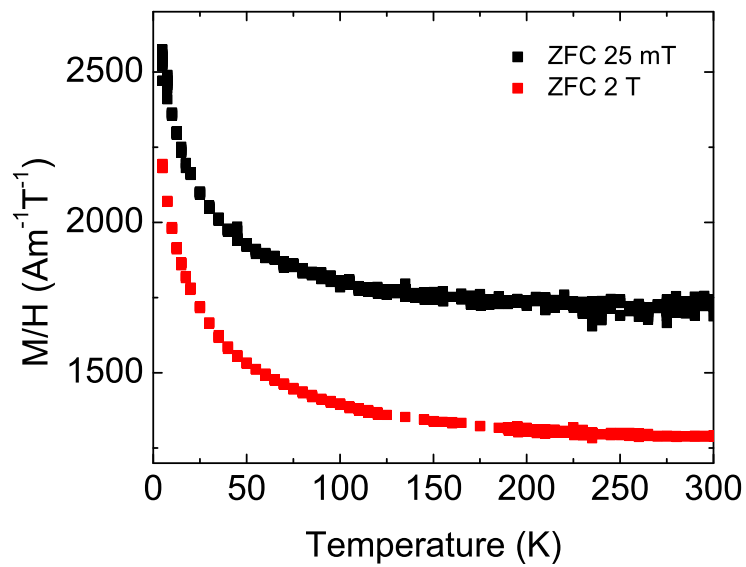


Figure 7.15: ZFC magnetisation of MnN measured in different applied fields, normalised to the field.

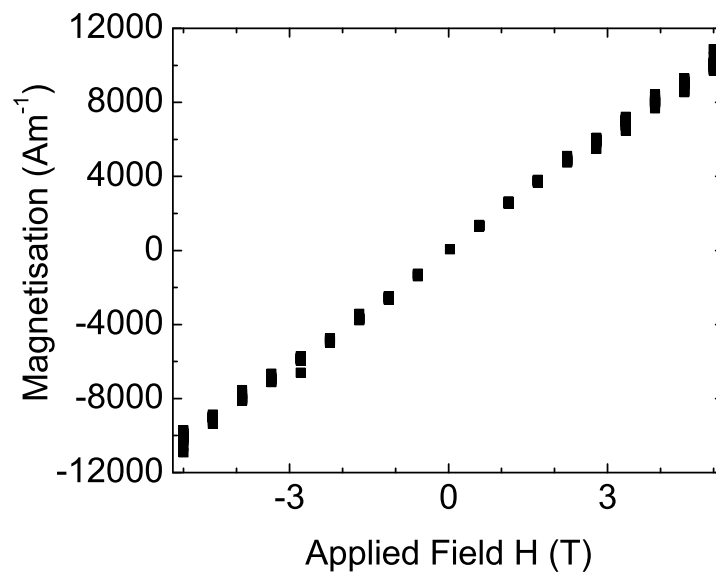


Figure 7.16: Field-dependent magnetisation loop of MnN at 5 K.

in a paramagnetic-like behaviour is from imperfect collinear alignment of the magnetically 'free' Mn moments, or a small excess of paramagnetic Mn ions.

## 7.3 Summary

### 7.3.1 GaMnN

The resistivity of GaMnN up to 10.8 at. % Mn content increases at lower temperatures, indicating semiconducting behaviour. The GaMnN films have lower resistivities compared with Mn-free GaN films, and increasing the Mn content both decreases the resistivity and weakens the temperature dependent resistivity variation. The resistivity of films with 6.2 at. % or less Mn agrees with a VRH model of conduction, associated with carrier hopping between Mn-related defect states in the bandgap of the GaN. At 10.8 at. % Mn there are sufficient dopant/defect states that hopping conductivity is no longer dominant, and instead the temperature-dependent behaviour approaches that of a disordered metal, albeit with a higher resistivity. The Mn induces significant optical absorption below the absorption edge of *nx*-GaN films, over a large range of energies. Addition of more Mn increases absorption below the edge. Consistent with the resistivity results, the optical behaviour shows that the Mn adds localised states into the *nx*-GaN bandgap, and these states start to form an impurity band in which conduction can occur at large enough Mn content ( $\sim 10$  at. %). The magnetisation behaviour of GaMnN films is reasonably modelled with an adjusted Brillouin function for  $\text{Mn}^{2+}$  ( $J = 5/2$ ). The temperature dependence shows a predominantly paramagnetic behaviour up to concentrations of  $\sim 4.3$  at. %, with a significant contribution from spin-canted antiferromagnetically exchange-coupled Mn ions. At Mn levels above this concentration a majority of the Mn ions couple antiferromagnetically and do not contribute further to the magnetisation above the level reached in the more dilute films. A film with a very high Mn concentration and a large degree of structural disorder frustrates these exchange-correlated Mn ions and leads to a spin-glass behaviour. The spin-glass canting of the

correlated Mn reasonably explains deviations from predictions expected in the case of pure paramagnetic behaviour of the Mn. There is no evidence for a ferromagnetic transition, remanence or hysteresis down to 5 K. All optical, resistivity and magnetic measurements are consistent with a mixed valency of incorporated  $\text{Mn}^{3+/2+}$  ions in the GaMnN films.

### 7.3.2 MnN

The resistivity of nanocrystalline MnN behaves like that of a metal, with a large residual value due to the high level of disorder in the films, and a Kondo-like upturn in resistivity below 30 K. The measured spectral conductivity from 0.1-6 eV is in good agreement with a combination of a Drude term and that arising from interband transitions as derived from band structure calculations. Deviations from the calculated conductivity have been elsewhere ascribed to the high degree of disorder in the films which relaxes the momentum conservation rule, as well as some other effects. However, this interpretation may not be valid in light of similar optical conductivity results from single crystalline MnN films where disorder-related effects would not be expected. The XANES and XES of the N  $K$ - and Mn  $L$ - edges show qualitative agreement with band-structure derived PDOS for those elements. Magnetic measurements are consistent with the expected antiferromagnetic ordering of MnN, with a small paramagnetic-like temperature-dependent magnetisation below ambient temperatures which may originate from a fraction of 'free' or spin-canted Mn atoms that are able to partially orient in the presence of a magnetic field.





## Chapter 8

# Rare Earth Nitride Background

### 8.1 Experiment

The first studies on the RENs emerged in the 1960s [209–212], when new techniques for separation of the RE metals allowed reasonably pure starting materials to be used. The materials studied at this time were usually grown in bulk by a high-temperature reactive arc melting reaction of the RE starting materials with  $\text{NH}_3$  or  $\text{N}_2$  gas. Fine powders were yielded by a direct reaction of the REs with  $\text{NH}_3$  or  $\text{N}_2$  gas to form the nitride [213–215], or with the interim step of conversion to the hydride [209, 216–219]. Polycrystalline [220] or single crystal [221] samples were also successfully prepared. In recent years, thin films have been grown by sputtering [222–225].

XRD and neutron diffraction studies on the material produced found a NaCl structure for all of the RENs [226]. A number of investigations into their magnetic properties revealed the series contains ferromagnetic, antiferromagnetic and paramagnetic materials [218, 219, 227, 228]. Table 8.1 summarises the results of these studies. Surprisingly, the conductive and optical characteristics of the RENs were not determined, and few studies addressing these properties have been published. Optical bandgaps in the order of  $\sim 2$  eV were found for DyN, ErN and HoN [209], and a broad absorption edge was seen in an epitaxial GdN film in the same energy range [222], although a recent report concluded that the bandgap of GdN

was near 4.1 eV [225].

Additionally, different groups have found materials that had metallic [218, 221, 229] or insulating [223] charge carrier concentrations and temperature-dependent resistivity behaviours. It has been recognised [209] that the instability of the RENs in moist atmospheres and the difficulty in preparing stoichiometric material [229, 230] was the likely cause for the substantial disagreement in the reported electrical and optical properties. Samples tended to be metal rich or unintentionally contain oxygen, and the expected surplus of conduction electrons could drive an intrinsically semiconducting material to have metallic or semimetallic conduction [209].

## 8.2 Band Structure - Calculation and Experiment

From the 1980s refined methods of band structure calculations provided a mechanism by which the electronic properties of the RENs could be studied. Band structure calculations had previously proved too difficult due to uncertainty about the energies of the  $4f$  electronic levels, which behave largely as core-like states. These studies [234–238] focussed primarily on GdN, which, with a half-filled  $4f$  shell, simplified the calculations somewhat by quenching the orbital component of the magnetic moment of the  $4f$  electrons. A number of these studies report the band structure of GdN calculated using the spin-polarised local density approximation with a self-interaction correction (LSDA+SIC) or a pseudopotential correction (LSDA+U) based on photoemission and inverse photoemission measurements [239] to determine the position of the  $4f$  levels relative to the Fermi energy in other Gd pnictides.

Hasegawa and Yanase [234] find the bandgap of GdN to be 0.2 eV using LDA without corrections, but concede that similar self-consistent calculations underestimate the bandgap of other materials by  $\sim 1.0$  eV. Lambrecht [235] used LSDA+U to find that GdN has a small indirect bandgap of 0.3 eV with a minimum direct bandgap of 0.8 eV in the ferromagnetic ground state (see Figure 8.1), and indirect and direct bandgaps of 0.7–0.85 eV and 1.1–1.2 eV respectively in the paramagnetic state. This study fol-

Nitride	Lattice constant (Å)	Magnetic order	$T_C$ (K)	$\theta_p$ (K)	Moment ( $\mu_B$ /RE ion)	$\mu_{\text{eff}}$ ( $\mu_B$ )
LaN	5.30 <sup>c</sup>	PM				
CeN	5.02 <sup>i</sup>	AFM				
PrN	5.16 <sup>f</sup>	PM		-11 <sup>e</sup> , 0 <sup>c,f</sup>	0.24 <sup>e</sup>	3.57-3.7 <sup>c,e,f</sup>
NdN	5.13 <sup>f</sup>	FM	28 <sup>a</sup> , 35 <sup>h</sup>	19 <sup>c</sup> , 24 <sup>a,f</sup> , 15 <sup>h</sup>	2.0-2.69 <sup>f</sup>	3.71 <sup>c</sup>
SmN	5.04 <sup>f</sup>	AFM		15 <sup>f</sup> , 13 <sup>h</sup>		
EuN	5.01 <sup>f</sup>	PM		-200 <sup>g</sup>		
GdN	4.99 <sup>f</sup>	FM	58 <sup>b</sup> , 60 <sup>j</sup>	81 <sup>b</sup> , 60 <sup>c</sup> , 75 <sup>e</sup> , 69 <sup>f</sup>	6.88-7.2 <sup>b,e</sup>	7.86-8.2 <sup>c,e,f</sup>
TbN	4.94 <sup>f</sup>	FM	42 <sup>d</sup> , 39 <sup>j</sup>	38 <sup>c</sup> , 34 <sup>f</sup>	5.4-7.0 <sup>d</sup>	9.5-10 <sup>c,d,f</sup>
DyN	4.89 <sup>d</sup>	FM	26 <sup>d</sup> , 17 <sup>j</sup>	22 <sup>c</sup> , 20 <sup>f</sup>	4.8-7.4 <sup>d,f</sup>	10.6 <sup>c,f</sup>
HoN	4.87 <sup>d</sup>	FM	18 <sup>d</sup> , 13 <sup>j</sup>	19 <sup>c</sup> , 29, 12 <sup>f</sup>	6.0-8.9 <sup>d,f</sup>	10.3 <sup>c</sup> , 10.8 <sup>d,f</sup>
ErN	4.84 <sup>f</sup>	FM	5 <sup>d</sup> , 6 <sup>j</sup>	5 <sup>c</sup> , 4 <sup>f</sup>	3-6 <sup>d,f</sup>	9.2 <sup>c</sup> , 9.4 <sup>d,f</sup>
TmN	4.81 <sup>d</sup>	PM		-21 <sup>e</sup> , -18 <sup>f</sup>	0 <sup>c</sup>	7.5 <sup>c</sup> , 7.32 <sup>e</sup>
YbN	4.79 <sup>k</sup>	AFM		-90 <sup>c</sup> , -130 <sup>f</sup> , -102 <sup>h</sup>		4.8 <sup>c</sup> , 5.1 <sup>f</sup>
LuN	4.76 <sup>l</sup>	PM				

Table 8.1: Structural and magnetic properties of RENs. FM = ferromagnetic, AFM = antiferromagnetic, PM = paramagnetic. Moment is the maximum value of the moment at low temperatures and  $\mu_{\text{eff}}$  is the paramagnetic moment derived from a Curie-Weiss law fit above  $\theta_p$ .

<sup>a</sup> Schobinger-Papamantellos *et al.* 1973 [231]

<sup>b</sup> Li *et al.* 1997 [232]

<sup>c</sup> Didchenko and Gortsema 1963 [218]

<sup>d</sup> Child *et al.* 1963 [217]

<sup>e</sup> Schumacher and Wallace 1965 [216]

<sup>f</sup> Busch *et al.* 1965 [228]

<sup>g</sup> Busch 1967 [229]

<sup>h</sup> Schumacher and Wallace 1966 [219]

<sup>i</sup> Gambino and Cuomo 1966 [210]

<sup>j</sup> Busch *et al.* 1963 [227]

<sup>k</sup> Brown and Clark 1974 [230]

<sup>l</sup> Klemm and Winkelmann 1956 [233]

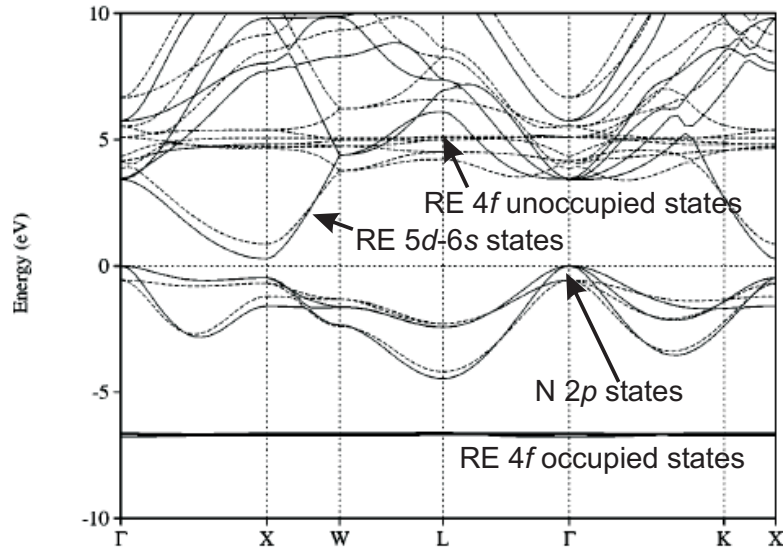


Figure 8.1: LSDA+U calculation of GdN band structure: solid line majority spin, dashed line minority spin, including both  $U_f$  shifts of  $4f$  states and gap correction, from [235].

lowed up on an earlier report by Petukhov *et al.* [236] that treated the  $4f$  states without a pseudopotential shift. Ghosh *et al.* [237] performed a similar calculation to Lambrecht and found the GdN bandgap to be vanishingly small in the spin-polarised state. It was found that a small variation in the starting calculation parameters could cause the conduction band to cross the Fermi level, and they concluded that GdN is on the borderline between metal and semiconductor, possibly undergoing a metal-insulator transition at the Curie temperature. By contrast, Duan *et al.* [238] found a half-metallic ground state for GdN from an LSDA+U calculation using the theoretical equilibrium lattice constant  $4.92 \text{ \AA}$ . As the lattice constant was increased, the valence and conduction bands started to separate, and a bandgap opened up at 14% strain. Most recently, Larson and Lambrecht [240] used LSDA+U with  $4f$  and  $5d$  electronic level pseudopotential shifts determined by photoemission, inverse photoemission and optical absorption above the Curie temperature to show that GdN has a bandgap of 0.09 eV in the spin-polarised state, and 0.46 eV in the paramagnetic state.

Experimental investigations into the band structure of GdN are limited due to the difficulty in preparing stoichiometric samples of all RENs. The only systematic study of GdN in recent years was performed on samples in the form of thin films prepared through  $N^+$  plasma-assisted reactive sputtering and capped with a thin layer of Cr or Al to prevent reaction with moisture [224, 241, 242]. The material was found to have ferromagnetic properties with a saturation moment ( $6.8 \pm 0.3 \mu_B/\text{Gd}$ ) and a  $T_C$  ( $= 59 \text{ K}$ ) in agreement with earlier studies. The resistance at ambient temperature was  $\sim 10 \text{ m}\Omega\text{cm}$ , and the resistivity increased with decreasing temperature, reaching a maximum value of 35% higher than the ambient value at  $T_C$ . Below  $T_C$ , resistivity decreased to 90% of the ambient temperature value near 10 K. The GdN films had a negative magnetoresistance, and it was concluded that the transition to magnetic ordering splits the conduction band enough to cause an overlap of the majority spin band with the valence band states. Thus, the GdN undergoes a semiconductor-metal transition associated with the onset of ferromagnetic ordering. X-ray photoelectron spectroscopy performed on the films found the occupied Gd  $4f$  electronic levels at 7.8 eV below the Fermi level. This compares well with the position of the the occupied  $4f^6$  final state for the other Gd pnictides [239], although it was acknowledged that relaxation effects associated with the photoelectron excitation process prevented an exact determination of the energy position of the occupied  $4f$  electrons in their ground state. Magnetic circular dichroism was observed for both the Gd  $4f$  and N  $2p$  states, and the magnitude of this dichroism closely followed the field dependence of the bulk film magnetisation, showing that these states are those that give rise to the film magnetisation [242]. The presence of dichroism in the N  $2p$  states indicates that some hybridisation of the spin-polarised RE  $4f$  states and these N states takes place, calling into question the current models which treat the magnetic behaviour of the RENs as arising totally from the RE  $4f$  electrons. A full understanding of the contributions to the magnetic ordering has not yet been formulated.

### 8.3 Summary and Outlook

Initial investigations into the RENs in the 1960s found a great variation in their magnetism from one material to the next, but no agreement has been reached on their conduction properties, which appear to depend very sensitively on the material stoichiometry. These early attempts routinely resulted in materials with N vacancies, and it was hypothesised that such vacancies hid the true ground states of the materials - metals or insulators. After little further investigation into the RENs over the last 30 years, advances in band structure calculation methods have led to a rebirth of interest in these materials due to predictions of interesting magnetic and optical properties. One recent experimental study has found that GdN may undergo a semiconductor-metal transition with the establishment of ferromagnetic order, and an initial probe of the DOS has started to aid theoretical efforts towards understanding the band structure of GdN. Additionally, research into the possible use of RE doping into GaN [12–19, 21] and other wide-bandgap semiconductors [16, 20] for encouraging ferromagnetism at high temperatures will benefit from investigation of REN compounds. The focus must now be on continuing the experimental work on stoichiometric RENs, including confirmation of the optical, conductive and band structure properties of GdN, and finding the same for the other thirteen in the series.







## **Chapter 9**

# **Composition, structure, electronic and magnetic properties of rare earth nitrides**

This chapter describes the results of investigations into the compositional, structural, transport and magnetic properties of a number of rare earth nitride thin films. The experimental techniques used are similar to those described in Chapter 5, and only details specific to the measurements applied to the RENs will be mentioned here.

## **9.1 Experimental Techniques**

### **9.1.1 Composition - Ion Beam Analyses**

It is important to determine the composition of the REN films as it is known that their magnetic and structural properties vary strongly with even a few percent of elements such as carbon or oxygen [211, 243]. In this study ion-beam analysis methods were used to determine the composition of the films. The particular methods used were RBS, NRA and PIXE. SIMS has also been performed on a specimen to determine the depth profiles of the elements of interest. RBS, NRA and SIMS techniques were identical to those performed on MnN and GaMnN films, and these techniques as well

as PIXE have been described in Section 5.2.

### 9.1.2 Structural analysis

The structure of the REN films has been investigated using XRD in both normal and grazing incidence geometries (see Section 5.3.1). Raman spectroscopy (Section 5.3.4) was performed through the GaN capping layer onto the films with Ar<sup>+</sup> (514 nm) and He-Ne (633 nm) laser excitation sources. At these wavelengths the GaN capping layer is transparent, and the inelastically scattered Raman spectrum is for the most part due to the underlying REN film and substrate.

### 9.1.3 DC electrical resistivity

The temperature-dependent resistivity behaviour of the RENs has not been clearly determined before, and there are conflicting reports ranging from insulating [223] to semi-metallic [218, 221] and metallic [209] in the literature. The DC electrical resistivity of REN films has been investigated as a function of temperature from 80-320 K after film deposition onto insulating Al<sub>2</sub>O<sub>3</sub> substrates. These measurements were performed *in-situ* at pressures below 10<sup>-5</sup> mbar in order to ensure the measured resistivities originate from the RENs as prepared, considering the high reactivity of these materials in atmospheric conditions. Typical room temperature resistivities of the REN films are between 10<sup>-1</sup> and 1 Ωcm. As already described, the resistivity was monitored during deposition of the capping layer and found not to change, which confirms the GaN and MgF<sub>2</sub> capping layers are highly insulating. After the capping layers had been deposited onto the films, the resistivity measurements for GdN films were repeated *ex-situ* from ~1.4 K to 300 K.

### 9.1.4 Magnetic behaviour

The magnetic properties of the REN films have been investigated using a SQUID magnetometer. The films deposited on Si substrates with GaN capping layers were loaded into the SQUID using the same procedure as

Film	Thickness (nm)	Rare earth %	N %
GdN	223	50	50
DyN	210	46	54
ErN	224	52	48

Table 9.1: Compositions and thicknesses of rare earth nitride films. Uncertainties are estimated at 1 - 2 %.

reported in Section 5.7. ZFC and FC measurements were performed from 2-300 K in fields of 50 mT and 1 T, and field loops measured between 0 and 6 T at temperatures of 5 or 10 K. Diamagnetism from the substrates and capping layers is small relative to the strong magnetic signal from the large moments of the RE ions in the REN films, and can be neglected.

## 9.2 Results

The compositions of a number of REN films are listed in Table 9.1. RE concentrations were determined by RBS measurements and confirmed by PIXE analysis, and the concentration of N was determined using RBS and checked with NRA measurements. NRA was also used to ensure the O content was low (1 % or less) for all films.

Figure 9.1 shows a representative XRD pattern for a 200 nm thick GdN film capped with  $\text{MgF}_2$ . The peaks originating from the GdN film are labelled with their Miller indices, and the remaining peaks arise from the  $\text{MgF}_2$  layer. The GdN peaks are attributed to the cubic NaCl structure, and this structure has been observed in a TEM study of the films [244]. The lattice constant of the films derived from the XRD is 5.01 Å, slightly larger than the reference value for bulk GdN of 4.989 Å [212, 245]. The presence of O in GdN has been observed to decrease the lattice parameter [210, 211], and the slight increase determined in this study supports the conclusion from IBA measurements that O is not present in these films in significant quantities. The films are nanocrystalline, and Debye-Scherrer

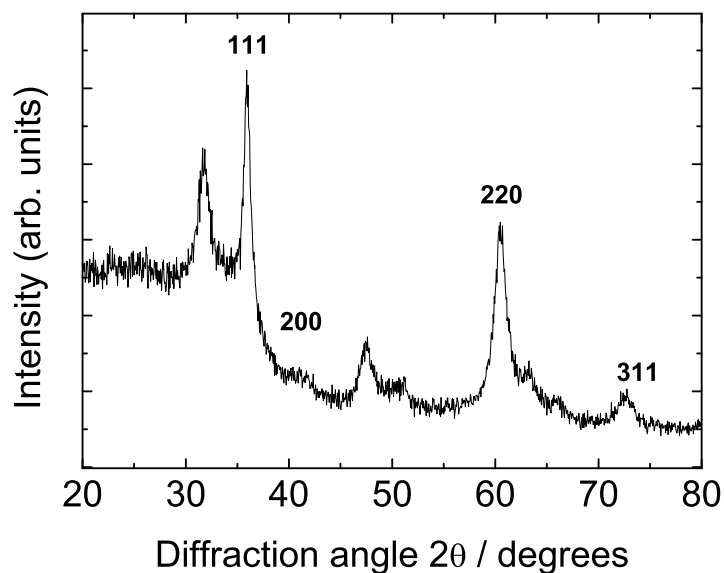


Figure 9.1: XRD pattern of a 200 nm thick GdN film capped with MgF<sub>2</sub>.

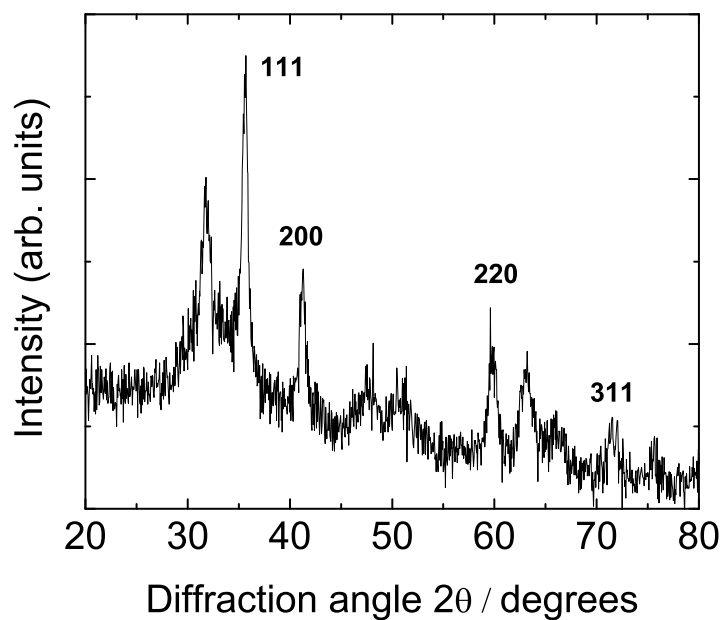


Figure 9.2: XRD pattern of a 200 nm thick SmN film capped with MgF<sub>2</sub>.

fitting of the most prominent peak reveals the crystallites average 10 nm in size. No secondary phases were detected in the XRD pattern and there are no discernible differences in the XRD patterns between films capped with GaN or MgF<sub>2</sub>. The (200) scattering peak at  $2\theta = 41^\circ$  is weaker than expected, suggesting the film may be textured. However, further XRD measurements performed at different angles did not find evidence of a simple texturing. X-ray scattering intensity is proportional to  $Z^2$  ( $Z$  = atomic number), so the peaks seen are predominantly due to scattering from the heavier Gd ions. In light of this, an ordered array of N vacancies is not expected to cause the large observed reduction of the (200) peak intensity. This feature appears to result from a variation in the order of the Gd atoms from the NaCl structure over long ranges in the film. Several options exist that could possibly explain the reduced peak, including a random stacking of alternating crystalline sequences, similar to that seen in the GaMnN films. Note that despite the difference in the implied structure of these films from that of other reports on GdN, the  $T_C$  and magnitude of the magnetic response reported below point to these GdN films maintaining the properties of the highest quality GdN material reported.

Figure 9.2 is an XRD pattern from a 200 nm thick SmN film capped with MgF<sub>2</sub>. The SmN peaks are labelled with their Miller indices, and the other peaks are from the capping layer. The SmN peaks correspond to the expected NaCl structure. The (200) peak is of approximately the expected strength when considered in relation to the (100) and (220) peaks, and the lattice constant derived from this pattern is 5.07 Å (5.04 Å in Ref [228]). The film is nanocrystalline, with an average crystallite size of 13 nm.

Raman spectroscopy measurements also show evidence for the structural differences between GdN and the other RENs investigated. Figure 9.3 shows the Raman spectra of the REN thin films, capped with ~200 nm GaN capping layers. The spectra were acquired using both the He-Ne 633 nm and Ar<sup>+</sup> 514 nm lasers, at two scans of 20 seconds for each measurement. Spectra were measured on films grown on both Al<sub>2</sub>O<sub>3</sub> and Si substrates and found to show the same features. The spectra shown in Figure 9.3 were taken with the 633 nm excitation on Al<sub>2</sub>O<sub>3</sub> substrate films in order to avoid interference from the strong Raman peak from Si at ~520

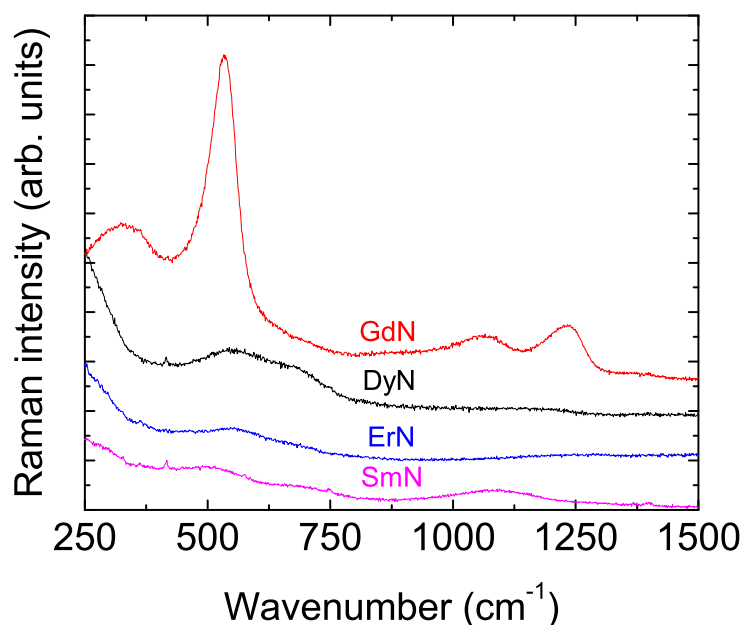


Figure 9.3: Raman spectra of SmN, ErN, DyN and GdN grown using ion-assisted deposition on  $\text{Al}_2\text{O}_3$  substrates taken under 633 nm laser excitation. The marked difference between the GdN spectrum and that of the other RENs supports the structural difference implied by XRD measurements.

$\text{cm}^{-1}$ . Spectra from the SmN, ErN and DyN in Figure 9.3 were taken on films grown using an IAD technique similar to that described in Chapter 4 for growth of GaMnN and MnN films. Raman spectra taken on GdN films grown using either the  $\text{N}_2$  gas or IAD techniques reproduce the same features, and XRD shows that films grown using either technique have the same structure, with a reduction in crystallite size for the IAD films.

In Figure 9.3, the Raman spectra for SmN, ErN and DyN show only weak, broad features from 500-750  $\text{cm}^{-1}$  and in SmN an additional broad feature near 1100  $\text{cm}^{-1}$ . There are no Raman-active vibrational modes for single crystalline NaCl structure materials, and the weak features seen in these films are consistent with a relaxation of the selection rules imposed by long range order, considering that these films are nanocrystalline. The GdN film however shows a strong, sharper peak at 535  $\text{cm}^{-1}$ , and stronger

broad features at  $320\text{ cm}^{-1}$ ,  $1065\text{ cm}^{-1}$  and  $1240\text{ cm}^{-1}$ . These peaks support the inference from XRD on GdN that this material has structural differences from the other RENs, and does not simply form as nanocrystals in the NaCl structure.

The wide variability of the resistivity behaviour of GdN obtained in previous measurements can be explained as a consequence of the difficulty in preparing stoichiometric material. It has already been postulated that N vacancies are the dominant contribution to charge carriers in O-free GdN [212]. As part of the study presented here, during deposition of a GdN film the in-plane conductance was measured as the background  $\text{N}_2$  pressure of the growth was decreased. The conductance rose as the  $\text{N}_2$  pressure fell, and the conductivity is expected to vary only with depth in the film. With this depth dependence only, the measured conductance of a film of thickness  $d$  is given by

$$S(= 1/R) = \frac{W}{L} \int_0^d \sigma(z) dz \quad (9.1)$$

$$\sigma(z) = \frac{L}{W} \frac{d(1/R)}{dz} \quad (9.2)$$

where  $S$  is the conductance,  $R$  is the measured resistance over a path of width  $W$ , length  $L$  and  $z$  is the depth in the film.

Figure 9.4 shows the differential conductivity for a GdN film prepared as  $\text{N}_2$  gas pressure was decreased. The film was deposited at a constant rate of  $2.0\text{ Ås}^{-1}$  throughout. At the beginning of the film growth, when the  $\text{N}_2$  partial pressure was  $10^{-4}$  mbar, the conductivity was constant at a value of  $3\text{ Scm}^{-1}$ . When the  $\text{N}_2$  partial pressure was reduced below  $5 \times 10^{-5}$  mbar, the conductivity of the layer deposited began to increase. As the partial pressure decreased to below  $2.5 \times 10^{-6}$  mbar, the conductivity increased dramatically, indicating the film layer grown at this pressure was metallic with a resistivity lower than  $10^{-2}\text{ Ωcm}$ .

The behaviour of the differential conductivity with  $\text{N}_2$  partial pressure indicates that a lower pressure results in layer growth with a higher concentration of carriers, and implies that the dominant contribution to

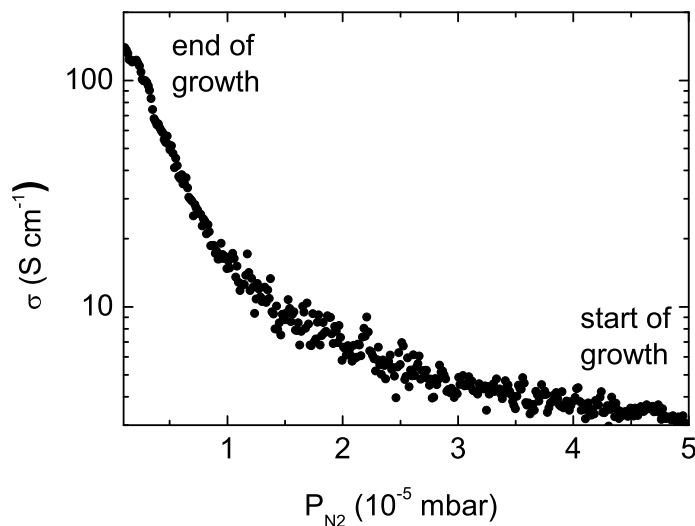


Figure 9.4: The differential conductivity of a GdN film as a function of  $\text{N}_2$  pressure, measured during deposition as the pressure was continuously diminished.

the carrier concentration is in the form of N vacancies. The effect of N vacancies on the film conductivity reconciles the reported low resistivities of bulk GdN with the insulating nature of GdN films capped with NbN [223]. The propensity of uncapped films to react with moisture, liberating  $\text{NH}_3$ , indicates that unprotected GdN is likely to be poor in N, and consequently low resistivities are reported. Films protected with a suitable capping layer, as in Xiao and Chien [223] and this study, are insulating. Reports of capped GdN films with ambient temperature resistivities of  $\sim 10 \text{ m}\Omega\text{cm}$  [224, 241] are consistent with this explanation when one observes the  $\text{N}_2$  background partial pressure during growth of these films was  $2 \times 10^{-5}$  mbar. The film layer studied in this thesis grown at similar partial pressures has a high concentration of carriers owing to a N deficiency (Figure 9.4).

The DC electrical resistivity of a GdN film grown at temperatures between 290 and 310 K with a  $\text{N}_2$  partial pressure of  $1 \times 10^{-4}$  mbar is shown in Figure 9.5. The room temperature resistivity of  $0.3 \Omega\text{cm}$  is characteristic of a heavily doped semiconductor, and is higher than previously reported



values [218, 224]. Fitting the activated conduction model Eq. 2.7 to the temperature-dependent behaviour above 80 K reveals a very small activation energy of  $E_A = 13$  meV (see Figure 9.6), which is further evidence for a heavily doped semiconductor. The resistivity reached a local maximum at 68 K, and dropped as temperature was lowered further. A turning point was reached at 22 K, and below this temperature the resistivity increased again, reaching  $5 \text{ } \Omega\text{cm}$  at 1.4 K, about 17 times the room temperature value. The inset of Figure 9.5 shows a close-up on the resistivity below 30 K. Below  $T_C$ ,  $E_A = 0.2$  meV, which is too small for the activated conduction model to be considered valid, although the smaller gradient of  $\ln(\rho)$  vs  $1/T$  is evidence for a change in the positions of the conduction and/or valence bands in relation to the Fermi level.

The room temperature resistivity of the GdN films is orders of magnitude larger than would normally be expected in the case of a metal (less than  $10^{-4} \text{ } \Omega\text{cm}$ ), although the nanocrystalline nature of the films means that the role of grain boundaries in the DC resistivity characteristic needs to be considered. Grain boundaries comprised of highly disordered or O-rich material could be insulating, and dominate the resistivity behaviour. However, compositional measurements rule out the presence of O in proportions as large as 1%, and the absence of alternate phases in the XRD and TEM [244] measurements on GdN films strongly supports the conclusion that the resistivity behaviour observed originates from the bulk of the GdN film. However, disordered material in the grain boundaries might not be detected in XRD. As will be shown below, the peak in the resistivity observed at 68 K corresponds to the  $T_C$  from magnetic measurements. The magnetic behaviour is a bulk-like effect, not due to grain boundaries, and is in agreement with previous reports on the magnetic character of GdN. The resistivity peak cannot have an origin from grain boundary dominated conduction processes, supporting the conclusion that the resistivity behaviour reported here is also characteristic of the properties of bulk-like GdN.

Temperature-dependent resistivity has been measured for several other RENs *in-situ*, and Figure 9.7 shows these measurements. Their ambient temperature resistivities are all close to that of GdN (shown for compari-

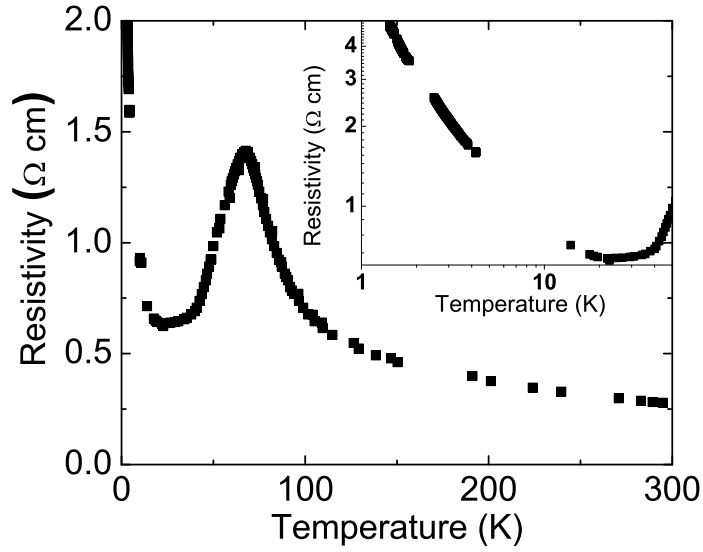


Figure 9.5: Temperature-dependent DC resistivity of a 200 nm thick GdN film capped with GaN.

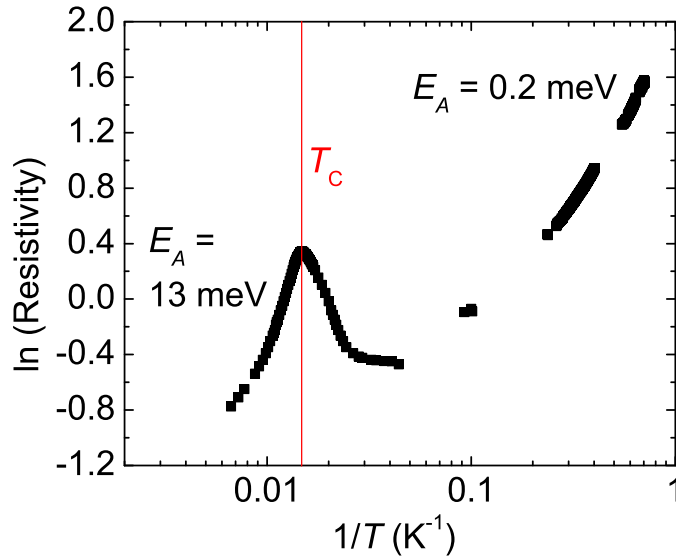


Figure 9.6: Test of activated behaviour of GdN resistivity from Figure 9.5. A fit to activated behaviour above  $T_C$  yields  $E_A = 13$  meV, a valid value for a doped semiconductor. An activated behaviour fit to data below 10 K yields  $E_A < 1$  meV, evidence for a shift of the bands in relation to the Fermi level.

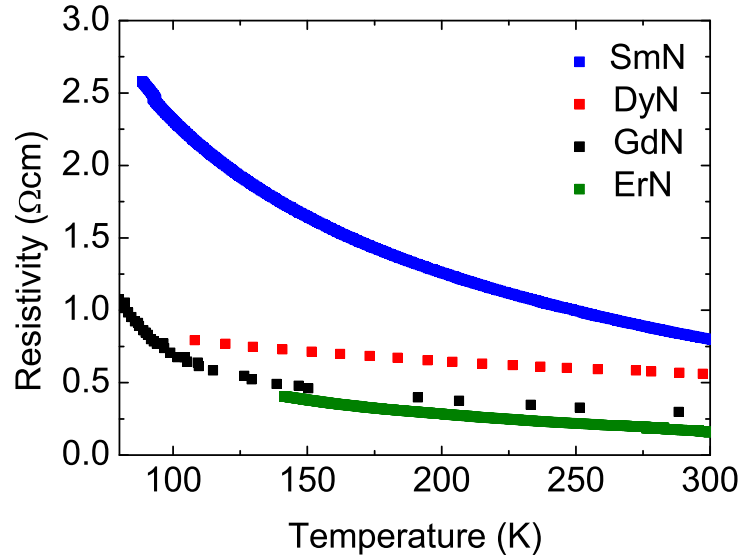


Figure 9.7: Temperature-dependent DC resistivities for various REN thin films capped with GaN. The data from Figure 9.5 for GdN are shown for comparison.

son), and similarly appear to be heavily-doped semiconductors.

The REN series is expected to exhibit a wide variety of magnetic behaviours, so magnetic characterisation of the prepared films has been made using a SQUID magnetometer. The films examined were those capped with GaN and deposited on Si substrates. In all cases except for SmN, the diamagnetic moment from the sample holder, Si substrate and GaN capping layer is small compared with the film moment and thus their effect is neglected.

Figure 9.8 plots the measured ZFC moment of a 200 nm thick GdN film deposited on Si with a 200 nm GaN capping layer, measured from 2 K to 300 K in 50 mT applied field. The measured moment was  $9.4 \times 10^{-6}$  emu at 300 K and followed Curie-Weiss behaviour in the paramagnetic region with a transition temperature of 68 K. Below 70 K the magnetic response increased rapidly and saturated near 5 K.

In the high temperature ( $T > 100$  K) paramagnetic region, the temperature-dependent behaviour can be described with the Curie-Weiss

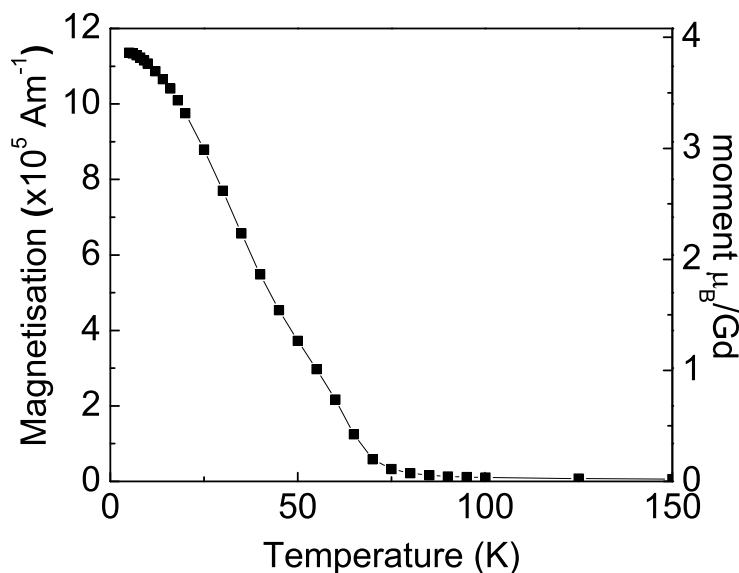


Figure 9.8: ZFC temperature-dependent magnetisation of a 200 nm GdN film capped with GaN. The measurement was taken in a field of 50 mT.

law Eq. 2.4. The value of  $p_{\text{eff}}$  extracted from this data is  $7.0 \pm 0.7$ , comparable to the experimental value for the  $\text{Gd}^{3+}$  ion of 8.0 [25], and in approximate agreement with previously published values for GdN [216, 220, 221, 227, 228, 232]. The implication is that Gd in GdN films can be thought of as present in a  $\text{Gd}^{3+}$  oxidation state in a simplified model of purely ionic bonding with N atoms. The small difference between the isolated RE ion moment and that derived from the above- $T_C$  measurements reflects the reality that the Gd-N bond in GdN is not entirely ionic, and that there is a component of the magnetic moment arising from some 4*f* electron hybridisation with other orbitals [240], resulting in a decreased moment.

Figure 9.9 is a field loop for a GaN-capped GdN film performed at 5 K. The presence of a hysteresis in the inset of Figure 9.9 confirms the ferromagnetic nature of GdN, with a remanence of  $2.74 \mu_B/\text{Gd}$  and a coercive field of around 220 Oe. The saturation moment per Gd in a field of 6 T is  $6.4 \pm 0.6 \mu_B$ , in agreement with the effective magneton value derived from the temperature dependence of the inverse of susceptibility in the

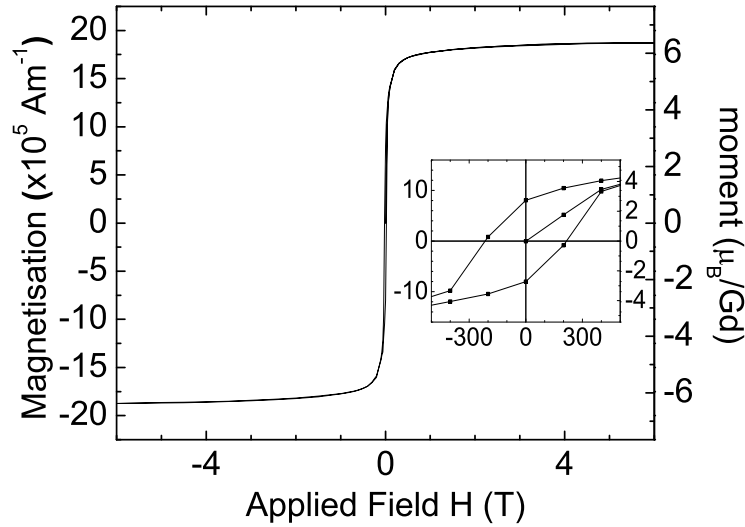


Figure 9.9: Field loop of a GdN film capped with GaN. The inset shows a close-up on the low field magnetisation, showing hysteresis and remanence. The measurement was performed at 5 K.

paramagnetic region. The magnetic behaviour of the films thus conforms fully to previous measurements on O-free GdN [216, 228, 229] and shows no sign of the decreased  $T_C$  and increased saturation field seen in earlier studies of O-bearing material [211, 212], or of the decreased remanence seen in material with a significant concentration of N vacancies [212].

The magnetic responses of the other RENs have also been investigated. The results of these measurements, including those for GdN, are reported in Table 9.2. DyN showed a ferromagnetic-like increase of magnetic moment below 20 K, and the existence of a hysteresis at 5 K confirms the strongly ordered magnetic moment of  $10.5 \mu_B/\text{Dy}$  as extracted from Curie-Weiss law fitting of the high temperature magnetisation. SmN has the smallest moment of all the RENs examined, and this moment dropped sharply below 10 K, signifying an ordered antiparallel alignment of Sm  $4f$  electron spins. ErN followed the Curie-Weiss law closely to 2 K, with no sign of cooperative ordering. There was no hysteresis present at 5 K. The apparent Curie temperature calculated from data measured using 50 mT applied field is -3 K, and 21 K using a field of 2 T. It appears likely

Film	Magnetic character	$T_C$ (K)	$\theta_p$ (K)	$\mu_{\text{eff}}$ ( $\mu_B/\text{RE}$ )	$\chi_{300\text{K}}$ ( $\times 10^{-6}$ )
GdN	Ferromagnetic	68	68	6.97	116670
DyN	Ferromagnetic	20	19	10.5	715000
SmN	Antiferromagnetic	$\sim 10$ ( $T_N$ )			
ErN	Paramagnetic	$< 2$	-3	8.5	1050

Table 9.2: Magnetic characterisation results for rare earth nitride films capped with GaN.

that ErN is a paramagnet to low temperatures, with the positive apparent Curie temperature an artefact of the strong field used.

### 9.3 Discussion and Summary

The REN films are nanocrystalline, with crystallite size around 10 nm, and have formed in the expected NaCl structure reported for stoichiometric material prepared before. The XRD scattering pattern for GdN has a reduced intensity (200) peak, which is not due to texturing and may be due to a random stacking of different lattice site sequences. Raman spectroscopy on the RENs showed a weak scattering from all but GdN, as expected for NaCl structured materials and which confirms the anomalous structure of the GdN. The capped REN films are all insulating, in contrast to a number of earlier reports of metallic behaviour. The resistivity behaviour of the films during growth implies that N vacancies are the source of charge carriers and may explain the lower resistivities reported before. The temperature-dependent resistivity behaviour for all the RENs prepared is semiconductor-like from ambient to liquid  $\text{N}_2$  temperatures. The room temperature resistivities of all the RENs are characteristic of heavily-doped semiconductors.

GdN resistivity reached a maximum at the Curie temperature, 69 K, and below this decreases. However, the resistivity behaviour at liquid He

temperatures shows that GdN is still a semiconductor, and the transition at  $T_C$  is not a semiconductor-metal transition. The magnetisation behaviour is in good agreement with previous reports on O-free material, and the presence of hysteresis at lower temperatures confirms the presence of ferromagnetism below  $T_C$ , which is 69 K. DyN is ferromagnetic below 20 K, SmN antiferromagnetic below 10 K and ErN paramagnetic down to 2 K.

The resistivity and magnetic behaviour of the GdN films allows a qualitative model to be devised of modifications to the band structure induced by the onset of ferromagnetic ordering as temperature is reduced below  $T_C$ . At ambient temperature the GdN films are heavily-doped semiconductors, with the Fermi level located below the conduction band. Thermally-activated conduction occurs, with the Fermi level possibly pinned to shallow donor states within the bandgap, which may be related to N vacancies. As the temperature is reduced, the resistivity increases as expected in a defective semiconductor. Upon cooling through  $T_C$ , the conduction band starts to become spin-split into components of majority and minority spin. The majority spin component of the conduction band lowers in energy, effectively lowering the energy barrier for thermal activation from the N vacancy states into the extended states of the conduction band. As a consequence, the resistivity reaches a maximum at the onset of the spin-splitting of the conduction band at  $T_C$ , and below this temperature resistivity decreases as the majority state contribution to the conduction band lowers further. The minority spin component will raise in energy, ensuring activated conduction is dominated by majority spin carriers. The resistivity reaches a minimum near 22 K once the spin-splitting of the conduction band has essentially saturated, however the majority spin conduction band component has not lowered enough to cross the Fermi level. As temperature is decreased further, the resistivity remains that of a defected semiconductor, albeit with a lower effective activation energy than above  $T_C$ .

It is worth noting that a spin-splitting of the conduction band for GdN upon the transition to ferromagnetic order has very recently been predicted [240, 246], although due to the difficulty in determining the position of the  $4f$  electronic states in the RENs the exact magnitude of the

splitting is uncertain. The change in effective activation energy from the GdN films examined in this study implies a smaller spin splitting-related lowering of the conduction band than has been predicted, although more investigations need to be made in order to reach a full understanding of the structure of energy levels near the Fermi level of the GdN films. In particular a spectroscopic study of the positions and shifts of electronic energy levels in GdN as a function of temperature is highly desired.

A similar peak in the resistivity of GdN coinciding with  $T_C$  has also been observed recently [224], although in that study it was concluded the ferromagnetic state induced an insulator-metal transition. The results reported here extend resistivity measurements to lower temperatures than previously reported, and these are perhaps the most interesting results from this study. The effect of magnetic ordering on the conduction behaviour of GdN is observed, although it is clear that in the ferromagnetically ordered state GdN remains semiconducting.







# Chapter 10

## Summary and Conclusions

The achievements described in this work are the growth of disordered thin films of GaMnN and MnN using ion-assisted deposition, and the characterisation of their compositional, structural, electronic, optical and magnetic properties with a range of complementary techniques. Thin films of a number of the rare earth nitrides were also grown and successfully capped, enabling determination of their structural, resistivity and magnetic properties.

Chapter 2 contains a brief overview of the basic theory of magnetism and describes theories of conduction in disordered semiconductors and metals. A number of terms and equations used throughout this thesis were introduced and defined.

In Chapter 3 a review of the experimental and theoretical progress towards growing and characterising GaMnN was presented. Theoretical predictions vary, but many groups have found that GaMnN has great potential for achievement of a room temperature ferromagnetic semiconductor. Numerous techniques of incorporating Mn into the wurtzite GaN structure have been explored, usually to form crystalline thin films. Experimental investigations of the electronic, optical and magnetic properties of GaMnN have often reported high temperature ferromagnetic behaviour, and numerous theories have been applied to explain the mechanism of this property. However, there is no agreement that such properties are intrinsic to GaN with randomly incorporated Mn, and the problem of ensuring against precipitation of alternate phases in material prepared using stan-

standard thin film growth techniques means that very careful investigations of the structure and magnetic properties must be undertaken for each preparation. Use of growth techniques that produce material far from its equilibrium state and investigation with a number of complementary experimental techniques are strongly suggested as important steps to resolve the question of the properties of single-phase GaMnN. The rest of the chapter deals with previous theoretical and experimental work done on MnN. This material is of interest as a potential secondary phase in GaMnN, as well as for its own potential usefulness in technological applications. Theoretical calculations have found agreement with experiment that the structure is rocksalt, with a distortion along the  $c$  axis due to magnetostriction. The magnetic structure is experimentally found to be antiferromagnetic of the first kind at ambient temperatures, and the Neel temperature is estimated from magnetic measurements to be 650 K, accompanied by a structural transition to the undistorted rocksalt phase.

Chapter 4 provided details of the ion-assisted deposition growth technique used to obtain thin films of GaMnN and MnN. This method involves thermal evaporation of the metals onto a variety of substrate materials whilst simultaneously bombarding them with low energy ( $<1000$  eV) N ions. This was carried out under UHV conditions at ambient temperatures. Growth of rare earth nitride films by evaporation of the metals in the presence of ultra-high purity  $N_2$  gas was also described. The rare earth nitride films are very sensitive to atmospheric water vapour, and thin capping layers of GaN or  $MgF_2$  were deposited on them to protect them from atmosphere, allowing their properties to be measured.

Chapter 5 briefly described the experimental methods used to characterise all films investigated in this thesis. These techniques included compositional, structural, DC resistivity, optical and magnetic measurements. Band structure calculations for MnN performed elsewhere that are associated with this study were briefly mentioned.

In Chapter 6 the compositional and structural characterisation results for the GaMnN and MnN thin films were presented. The GaMnN films are between 97 and 230 nm thick and contain between 4 and 18 at. % Mn. Concentrations of adventitious O were determined to be between 0.5 and

4.4 at. %, and this was mostly due to post-growth oxidation of the top surface of the films. A film was also prepared with 19 at. % Mn and a high intentional O content. There is an excess of N in almost all films, which takes the form of  $N_2$  molecules. The structure of the films and the Raman-active phonon states are similar to that of the random-stacked structure of nanocrystalline Mn-free GaN films grown using ion-assisted deposition. An increase of lattice constant and Mn-N bond length in the films with higher Mn content suggests the Mn is incorporated in the  $Mn^{2+}$  oxidation state. The crystallites are approximately 3 nm in size, but significant disorder persists even within these crystallites. Upon prolonged exposure to UV laser light, a partial reconstruction of the structural order was observed, similar to that induced by annealing of IAD-GaN films. There is no evidence for alternate phases or precipitation within the GaMnN films. The MnN films were found to contain 1:1 ratios of the elements, and O is present at less than 1 at. %, mostly due to post-growth oxidation of the top 10% of the film. The MnN films are comprised of 8 nm nanocrystals in the distorted rocksalt structure, and the pseudo-rdf from EXAFS showed no evidence of any phase but MnN.

In Chapter 7 the electronic and magnetic properties of the GaMnN and MnN films were presented and discussed. GaMnN films with 4-10 at. % Mn are semiconducting below ambient temperature, and addition of Mn decreases both the resistivity and the temperature dependence from that of Mn-free IAD-GaN films. Variable range hopping conduction was observed at lower Mn concentrations, implying a mixture of  $Mn^{2+}/3+$  valency, and at 10 at. % incorporated Mn the film resistivity behaviour approaches that of a disordered metal. The Mn causes a significant increase of optical absorption below the bandgap of  $nx$ -GaN, from 3.4 eV to at least 1 eV. Higher Mn content does not affect the energy profile of absorption in the films, but increases it over the whole range of energies. The results were consistent with Mn-related addition of states within the GaN bandgap. At high enough Mn concentration these states approximate an impurity band in which electrical conduction can take place. The magnetic behaviour of GaMnN films can be modelled as a coexistence of paramagnetic and antiferromagnetic phases from ambient temperature to 2 K, and

can be well explained as due to a proportion of magnetically active Mn in the 2+ oxidation state. Above 4 at. % Mn content all the extra Mn experiences antiferromagnetic exchange. Structural frustration of the antiferromagnetically correlated Mn spins results in spin-glass magnetic behaviour, explaining a ZFC-FC irreversibility in a strongly disordered film below 220 K and a larger than expected ambient temperature magnetisation in all films. The MnN resistivity is metallic, with a Kondo-like anomalous upturn below 30 K. The optical conductivity was measured from 0.08-6 eV and compared with that taken from band structure calculations applied to MnN. Reasonable agreement between theory and experiment was found, although a number of peaks present in the calculations were not found in the experimental optical conductivity. Band structure-derived PDOS for Mn and N are in good agreement with experimental x-ray spectroscopies on the Mn *L* and N *K* edges. The magnetic behaviour of MnN showed evidence for antiferromagnetic exchange, and a small paramagnetic-like temperature dependence below ambient temperatures, which may result from a small proportion of 'free' Mn.

Chapter 8 reviewed the progress made towards understanding the rare earth nitrides. Experimental investigations, chiefly from the 1960s, showed these materials form in the rocksalt structure and the 4*f* electrons give rise to a variety of magnetic behaviours at low temperatures, including ferromagnetism. No agreement had been reached on the conductivity behaviour, or on whether these materials are metals or semiconductors. In more recent years, new methods of band structure calculations have predicted that the combination of interesting magnetic and optical properties of the RENs make them promising materials from both purely scientific and novel electronics standpoints, and it is greatly desired to fully investigate this series.

In Chapter 9 the results of the experimental investigations of the capped rare earth nitride film properties were described. The structure of the ErN, SmN, DyN and GdN films is of nanocrystals in the rocksalt structure around 10 nm in size. XRD and Raman spectroscopy on the GdN films showed that this material may have subtle deviations from the rocksalt structure, and further structural measurements are needed to unam-

biguously determine the cause of the differences. The resistivity of all four RENs is characteristic of heavily doped semiconductors, and from GdN film growth in differing pressures of  $N_2$  gas the dominant defect was strongly suggested to be N vacancies. Magnetic measurements showed ErN is a paramagnet to 2 K, SmN is antiferromagnetic below 10 K and DyN is ferromagnetic with a  $T_C = 20$  K. The GdN film was ferromagnetic below 69 K, and the magnetic characteristics were in agreement with those determined from earlier studies on stoichiometric GdN. The resistivity of GdN reached a maximum at  $T_C = 69$  K. Below 20 K an upturn in the resistivity showed that in the ferromagnetic regime GdN remains a semiconductor. This revealed that exchange-splitting of the conduction band narrows the semiconducting bandgap in the ferromagnetic regime, but there is not a semiconductor-metal transition upon the onset of ferromagnetic order as previously described.

## 10.1 Outlook

Films of GaMnN grown with IAD have successfully incorporated more than 10 at. % Mn without evidence of phase segregation. However, the magnetisation results on the GaMnN films with as much as 18 at. % Mn show no sign of ferromagnetism. All films in this study have ambient temperature resistivities several orders of magnitude greater than the single crystalline films that report room temperature ferromagnetism, and the Mn in the films from this study is incorporated mostly in the 2+ oxidation state. The two mechanisms most cited as the cause for ferromagnetic behaviour in DMS like GaMnN are carrier-induced exchange coupling and double exchange, and the conditions for neither of these are satisfied in the IAD films. It would be of interest to investigate co-doping the GaMnN films with *p*- or *n*- type dopants to investigate their effects on the resistivity and oxidation state of the incorporated Mn ions. At the high Mn concentrations achieved, sufficient carrier concentrations may be incorporated and the conditions observed in room temperature ferromagnetic single crystalline GaMnN films may be able to be reproduced.

The optical conductivity of the MnN films showed significant differ-

ences from the calculated optical response. The previous suggestion that disorder induced effects may explain the departures from theory may not be valid in light of recent measurements on single crystalline MnN films that indicate similar differences to the band structure-derived conductivities. A full investigation of the optical conductivity of single crystalline MnN is desirable, as well as polarisation-dependent optical measurements, which would allow further comparisons with the band structure calculations that exist for MnN. Magnetisation measurements above ambient temperature would prove useful in verifying the state of magnetic ordering in thin films.

The rare earth nitrides are a comparatively unstudied group of materials, and the physical properties of many of them remain undetermined in the literature. Additionally, the recent exciting theoretical predictions of their exotic combination of electronic, optical and magnetic properties is a strong encouragement for further experimental work to be carried out. In particular, spectroscopic measurements of the density of states and exchange-induced shifts of their energy levels upon the transition to the magnetically ordered state would prove extremely useful in determining the potential uses of these materials.







# References

- [1] I. Žutić, J. Fabian, and S. D. Sarma, *Rev. Mod. Phys.* **76**, 323 (2004).
- [2] J. K. Furdyna, *J. Appl. Phys.* **64**, 29 (1998).
- [3] T. Dietl, H. Ohno, F. Matsukura, J. Cibert, and D. Ferrand, *Science* **287**, 1019 (2000).
- [4] H. Ohno, *Science* **281**, 951 (1998).
- [5] K. W. Edmonds, P. Bogusławski, K. Y. Wang, R. P. Campion, S. N. Novikov, N. R. S. Farley, B. L. Gallagher, C. T. Foxon, M. Sawicki, T. Dietl, M. B. Nardelli, and J. Bernholc, *Phys. Rev. Lett.* **92**, 037201 (2004).
- [6] T. Dietl, H. Ohno, and F. Matsukura, *Phys. Rev. B* **63**, 195205 (2001).
- [7] Y. K. Zhou, M. S. Kim, X. J. Li, S. Kimura, A. Kaneta, Y. Kawakami, S. Fujita, S. Emura, S. Hasegawa, and H. Asahi, *J. Phys.: Condens. Matter* **16**, S5743 (2004).
- [8] R. Jones, *Opt. Mats.* **28**, 718 (2006).
- [9] J. H. Park and A. J. Steckl, *J. Appl. Phys* **98**, 056108 (2005).
- [10] Z. Altounian, X. Chen, L. X. Liao, D. H. Ryan, and J. O. Ström-Olsen, *J. Appl. Phys.* **73**, 6017 (1993).
- [11] C. M. Aerts, P. Strange, M. Horne, W. M. Temmerman, Z. Szotek, and A. Svane, *Phys. Rev. B* **69**, 045115 (2004).

- [12] N. Teraguchi, A. Suzuki, Y. Nanishi, Y. Zhou, M. Hashimoto, and H. Asahi, *Solid State Commun.* **122**, 651 (2002).
- [13] M. Hashimoto, A. Yanase, R. Asano, H. Tanaka, H. Bang, K. Akimoto, and H. Asahi, *Jpn. J. Appl. Phys., Part 2* **42**, L1112 (2003).
- [14] S. Dhar, O. Brandt, M. Ramsteiner, V. F. Sapega, and K. H. Ploog, *Phys. Rev. Lett.* **94**, 037205 (2005).
- [15] S. Dhar, L. Pérez, O. Brandt, A. Trampert, K. H. Ploog, J. Keller, and B. Beschoten, *Phys. Rev. B* **72**, 245203 (2005).
- [16] S. Y. Han, J. Hite, G. T. Thaler, R. M. Frazier, C. R. Abernathy, S. J. Pearton, H. K. Choi, W. O. Lee, Y. D. Park, J. M. Zavada, and R. Gwilliam, *Appl. Phys. Lett.* **88**, 042102 (2006).
- [17] S. Dhar, T. Kammermeier, A. Ney, L. Pérez, K. H. Ploog, A. Melnikov, and A. D. Wieck, *Appl. Phys. Lett.* **89**, 062503 (2006).
- [18] J. Hite, G. T. Thaler, R. Khanna, C. R. Abernathy, S. J. Pearton, J. H. Park, A. J. Steckl, and J. M. Zavada, *Appl. Phys. Lett.* **89**, 132119 (2006).
- [19] J. K. Hite, R. M. Frazier, R. Davies, G. T. Thaler, C. R. Abernathy, S. J. Pearton, and J. M. Zavada, *Appl. Phys. Lett.* **89**, 092119 (2006).
- [20] K. Potzger, S. Zhou, F. Eichhorn, M. Helm, W. Skorupa, A. Mücklich, T. Herrmannsdörfer, and A. Bianchi, *J. Appl. Phys.* **99**, 063906 (2006).
- [21] G. M. Dalpian and S. Wei, *Phys. Rev. B* **72**, 115201 (2005).
- [22] J. S. Smart, *Effective Field Theories of Magnetism*, (W. B. Saunders Company, Philadelphia, 1966).
- [23] A. H. Morrish, *The Physical Principles of Magnetism*, (John Wiley & Sons, Inc., New York, 1965).
- [24] J. Crangle, *The Magnetic Properties of Solids*, (Edward Arnold Limited, London, 1977).

- 
- [25] N. W. Ashcroft and N. D. Mermin, *Solid State Physics*, (Thomson Learning, 1976).
- [26] R. M. White, *Quantum Theory of Magnetism*, (McGraw-Hill, Inc., New York, 1970).
- [27] N. F. Mott and E. A. Davis, *Electronic Processes in Non-crystalline Materials*, (Clarendon Press, New York, 1979).
- [28] H. L. Johnson, PhD thesis, Victoria University of Wellington, 1993.
- [29] <http://www.tuat.ac.jp/katsuaki/nandemoQ&A.html>.
- [30] A. B. Shick, J. Kudrnovský, and V. Drchal, *Phys. Rev. B* **69**, 125207 (2004).
- [31] N. Tandon, G. P. Das, and A. Kshirsagar, *cond-mat*, 060606 (2006).
- [32] P. Bogusławski and J. Bernholc, *Phys. Rev. B* **72**, 115208 (2005).
- [33] L. M. Sandratskii, P. Bruno, and J. Kudrnovský, *Phys. Rev. B* **69**, 195203 (2004).
- [34] L. M. Sandratskii, P. Bruno, and S. Mirbt, *Phys. Rev. B* **71**, 045210 (2005).
- [35] L. Kronik, M. Jain, and J. R. Chelikowsky, *Phys. Rev. B* **66**, 041203(R) (2002).
- [36] A. Filippetti, N. A. Spaldin, and S. Sanvito, *J. Magn. Magn. Mater.* **290-291**, 1391 (2005).
- [37] A. Filippetti, N. A. Spaldin, and S. Sanvito, *Chem. Phys.* **309**, 59 (2004).
- [38] B. Sanyal, O. Bengone, and S. Mirbt, *Phys. Rev. B* **68**, 205210 (2003).
- [39] B. S. Kang, W. C. Kim, Y. Y. Shong, and H. J. Kang, *J. Cryst. Growth* **287**, 74 (2006).

- [40] M. Wierzbowska, D. Sánchez-Portal, and S. Sanvito, *Phys. Rev. B* **70**, 235209 (2004).
- [41] K. Sato and H. Katayama-Yoshida, *Jpn. J. Appl. Phys., Part 2* **40**, L485 (2001).
- [42] E. Kulatov, H. Nakayama, H. Mariette, H. Ohta, and Y. A. Uspenskii, *Phys. Rev. B* **66**, 045203 (2002).
- [43] Z. S. Popovic, S. Satpathy, and W. C. Mitchel, *Phys. Rev. B* **70**, 161308(R) (2004).
- [44] L. Bergqvist, O. Eriksson, J. Kudrnovský, V. Drchal, P. Korzhavyi, and I. Turek, *Phys. Rev. Lett.* **93**, 137202 (2004).
- [45] K. Sato, W. Schweika, P. H. Dederichs, and H. Katayama-Yoshida, *Phys. Rev. B* **70**, 201202R (2004).
- [46] O. Eriksson, L. Bergqvist, B. Sanyal, J. Kudrnovský, V. Drchal, P. Korzhavyi, and I. Turek, *J. Phys.: Condens. Matter* **16**, S5481 (2004).
- [47] K. Sato, P. Dederichs, H. Katayama-Yoshida, and J. Kudrnovský, *Physica B* **340-342**, 863 (2003).
- [48] P. Mahadevan and S. Mahalakshmi, *Phys. Rev. B* **73**, 153201 (2006).
- [49] G. M. Dalpian and S. Wei, *Phys. Rev. B* **73**, 245204 (2006).
- [50] P. M. Krstajić, F. M. Peeters, V. A. Ivanov, V. Fleurov, and K. Kikoin, *Phys. Rev. B* **70**, 195215 (2004).
- [51] T. Graf, S. T. B. Goennenwein, and M. S. Brandt, *Phys. Status Solidi B* **239**, 277 (2003).
- [52] A. Kaminski and S. D. Sarma, *Phys. Rev. Lett.* **88**, 247202 (2002).
- [53] G. P. Das, B. K. Rao, and P. Jena, *Phys. Rev. B* **68**, 035207 (2003).
- [54] K. H. Kim, K. J. Lee, D. J. Kim, H. J. Kim, Y. E. Ihm, C. G. Kim, S. H. Yoo, and C. S. Kim, *Appl. Phys. Lett.* **82**, 4755 (2003).

- [55] S. Dhar, O. Brandt, A. Trampert, K. J. Friedland, Y. J. Sun, and K. H. Ploog, *Phys. Rev. B.* **67**, 165205 (2003).
- [56] J. M. Baik, J. Lee, Y. Shon, and T. W. Kang, *J. Appl. Phys.* **93**, 9024 (2003).
- [57] W. Gębicki, J. Strzeszewski, G. Kamler, T. Szyszko, and S. Podsiadło, *Appl. Phys. Lett.* **76**, 3870 (2000).
- [58] T. Szyszko, M. Kamiński, S. Podsiadło, K. Wóznia, L. Dobrzycki, and W. Gębicki, *J. Cryst. Growth* **276**, 419 (2005).
- [59] G. Kamler, J. Zachara, S. Podsiadło, L. Adamowicz, and W. Gębicki, *J. Cryst. Growth* **212**, 39 (2000).
- [60] M. Zając, R. Doradziński, J. Gosk, J. Szczytko, M. Lefeld-Sosnowska, M. Kamińska, A. Twardowski, M. Palczewska, E. Grzanka, and W. Gębicki, *Appl. Phys. Lett.* **78**, 1276 (2001).
- [61] M. Aoki, H. Yamane, M. Shimada, S. Sarayama, H. Iwata, and F. J. Disalvo, *Jpn. J. Appl. Phys., Part 1* **42**, 5445 (2003).
- [62] D. S. Han, J. Park, K. W. Rhie, S. Kim, and J. Chang, *Appl. Phys. Lett.* **86**, 032506 (2005).
- [63] J. M. Baik, Y. Shon, T. W. Kang, and J. Lee, *Appl. Phys. Lett.* **87**, 042105 (2005).
- [64] B. Liu, Y. Bando, C. Tang, D. Goldberg, K. Yamaura, and E. Takayama-Muromachi, *Chem. Phys. Lett.* **405**, 127 (2005).
- [65] Y. P. Song, P. W. Wang, H. Q. Lin, G. S. Tian, J. Lu, Z. Wang, Y. Zhang, and D. P. Yu, *J. Phys.: Condens. Matter* **17**, 5073 (2005).
- [66] J. Xu, J. Li, R. Zhang, X. Xiu, D. Lu, H. Yu, S. Gu, B. Shen, Y. Shi, Y. Ye, and Y. Zheng, *Opt. Mater.* **23**, 163 (2003).
- [67] M. E. Overberg, C. R. Abernathy, S. J. Pearton, N. A. Theodoropoulou, K. T. McCarthy, and A. F. Hebard, *Appl. Phys. Lett.* **79**, 1312 (2001).

- [68] Y. L. Soo, G. Kioseoglou, S. Kim, S. Huang, Y. H. Kao, S. Kuwabara, S. Owa, T. Kondo, and H. Munekata, *Appl. Phys. Lett.* **79**, 3926 (2001).
- [69] S. Kuwabara, T. Kondo, T. Chikyow, P. Ahmet, and H. Munekata, *Jpn. J. Appl. Phys., Part 2* **40**, L724 (2001).
- [70] Y. Cui and L. Li, *Appl. Phys. Lett.* **80**, 4139 (2002).
- [71] T. Okuno, T. Fujino, M. Shindo, M. Katayama, K. Oura, S. Sonoda, and S. Shimizu, *Jpn. J. Appl. Phys., Part 2* **41**, L415 (2002).
- [72] K. Huh, M. Ham, J. Myoung, J. Lee, K. Lee, J. Chang, S. Han, H. Kim, and W. Lee, *Jpn. J. Appl. Phys., Part 2* **41**, L1069 (2002).
- [73] S. Kuroda, E. Bellet-Amalric, R. Giraud, S. Marcet, J. Cibert, and H. Mariette, *Appl. Phys. Lett.* **83**, 4580 (2003).
- [74] M. B. Haider, C. Constantin, H. Al-Britthen, H. Yang, E. Trifan, D. Ingram, and A. R. Smith, *J. Appl. Phys.* **93**, 5274 (2003).
- [75] T. Graf, M. Gjukic, M. Hermann, M. S. Brandt, M. Stutzmann, L. Görgens, J. B. Philipp, and O. Ambacher, *J. Appl. Phys.* **93**, 9697 (2003).
- [76] P. P. Chen, H. Makino, J. J. Kim, and T. Yao, *J. Cryst. Growth* **251**, 331 (2003).
- [77] M. Hashimoto, Y. K. Zhou, H. Tampo, M. Kanamura, and H. Asahi, *J. Cryst. Growth* **252**, 499 (2003).
- [78] G. Thaler, R. Frazier, B. Gila, J. Stapleton, M. Davidson, C. R. Abernathy, S. J. Pearton, and C. Segre, *Appl. Phys. Lett.* **84**, 2578 (2004).
- [79] K. W. Edmonds, N. R. S. Farley, T. K. Johal, R. P. Champion, B. L. Gallagher, C. T. Foxon, and G. van der Laan, *J. Appl. Phys.* **95**, 7166 (2004).
- [80] H. C. Jeon, T. W. Kang, T. W. Kim, and Y. H. Cho, *Solid State Commun.* **138**, 444 (2006).



- [81] J. E. van Nostrand, J. D. Albrecht, B. Claflin, Y. Liu, M. I. Nathan, and P. P. Ruden, *Phys. Status Solidi B* **242**, 3182 (2005).
- [82] C. X. Gao, F. C. Yu, S. Y. Jeong, A. R. Choi, P. Parchinskiy, D. J. Kim, H. J. Kim, Y. E. Ihm, C. G. Kim, and C. S. Kim, *J. Magn. Magn. Mater.* **304**, e158 (2006).
- [83] F. Takano, H. Ofuchi, J. W. Lee, K. Takita, and H. Akinaga, *Physica B* **376-377**, 658 (2006).
- [84] M. L. Reed, M. K. Ritums, H. H. Stadelmaier, M. J. Reed, C. A. Parker, S. M. Bedair, and N. A. El-Masry, *Mater. Lett.* **51**, 500 (2001).
- [85] X. M. Cai, A. B. Djurisic, M. H. Zie, H. Liu, X. X. Zhang, J. J. Zhu, and H. Yang, *Mat. Sci. Eng., B* **117**, 292 (2005).
- [86] K. Sardar, A. R. Raju, B. Bansal, V. Venkataraman, and C. N. R. Rao, *Solid State Commun.* **125**, 55 (2003).
- [87] F. E. Arkun, M. J. Reed, E. A. Berkman, N. A. El-Masry, J. M. Zavada, M. L. Reed, and S. M. Bedair, *Appl. Phys. Lett.* **85**, 3809 (2004).
- [88] M. H. Kane, A. Asghar, A. M. Payne, C. R. Vestal, Z. J. Zhang, M. Strassburg, J. Senawirante, N. Dietz, C. J. Summers, and I. T. Ferguson, *Phys. Status Solidi C* **2**, 2441 (2005).
- [89] D. O'Mahony, J. G. Lunney, G. Tobin, and E. McGlynn, *Solid-State Electron.* **47**, 533 (2003).
- [90] N. Theodoropoulou, A. F. Hebard, M. E. Overberg, C. R. Abernathy, S. J. Pearton, S. N. G. Chu, and R. G. Wilson, *Appl. Phys. Lett.* **78**, 3475 (2001).
- [91] Y. Shon, Y. H. Kwon, D. Y. Kim, X. Fan, D. Fu, and T. W. Kang, *Jpn. J. Appl. Phys., Part 1* **40**, 5304 (2001).
- [92] C. Liu, E. Alves, A. R. Ramos, M. F. da Silva, J. C. Soares, T. Matsutani, and M. Kiuchi, *Nucl. Instrum. Methods Phys. Res., Sect. B* **191**, 544 (2002).

- [93] V. A. Guzenko, N. Thillosen, A. Dahmen, R. Calarco, L. H. Th. Schäpers, M. Luysberg, B. Schineller, M. Heuken, and A. Kaluza, *J. Appl. Phys.* **96**, 5663 (2004).
- [94] F. Zhang, N. Chen, X. Liu, Z. Liu, S. Yang, and C. Chai, *J. Cryst. Growth* **262**, 287 (2004).
- [95] L. L. Guo, W. Z. Shen, and Y. H. Zhang, *J. Appl. Phys.* **99**, 113533 (2006).
- [96] M. R. Islam, N. F. Chen, and M. Yamada, *Mater. Sci. Semicond. Process.* **9**, 184 (2006).
- [97] J. M. Baik, Y. Shon, T. W. Kang, and J. Lee, *Appl. Phys. Lett.* **84**, 1120 (2004).
- [98] M. Jeong, M. Ham, J. Myoung, and S. K. Noh, *App. Surf. Sci.* **222**, 322 (2004).
- [99] R. Y. Korotkov, J. M. Gregie, B. Han, and B. W. Wessels, *Physica B* **308-310**, 18 (2001).
- [100] M. J. Reed, F. E. Arkun, E. A. Berkman, N. A. El-Masry, J. Zavada, M. O. Luen, M. L. Reed, and S. M. Bedair, *Appl. Phys. Lett.* **86**, 102504 (2005).
- [101] Y. Shon, Y. H. Kwon, S. U. Yuldashev, Y. S. Park, D. J. Fu, D. Y. Kim, H. S. Kim, and T. W. Kang, *J. Appl. Phys.* **93**, 1546 (2003).
- [102] K. H. Baik, R. M. Frazier, G. T. Thaler, C. R. Abernathy, S. J. Pearton, J. Kelly, R. Rairigh, A. F. Hebard, W. Tang, M. Stavola, and J. M. Zavada, *Appl. Phys. Lett.* **83**, 5458 (2003).
- [103] J. Q. Wang, P. P. Chen, H. B. Mao, Z. Q. Zhu, and W. Lu, *Physica B* **358**, 185 (2005).
- [104] T. Graf, M. Gjukic, M. Hermann, M. S. Brandt, and M. Stutzmann, *Phys. Rev. B* **67**, 165215 (2003).

- [105] M. Kamiński, T. Szyszko, S. Podsiadło, K. Woźniak, L. Dobrzycki, W. Gębicki, J. Gosk, M. Zając, and A. Twardowski, *J. Cryst. Growth* **291**, 12 (2006).
- [106] G. Thaler, R. Frazier, B. Gila, J. Stapleton, R. Davies, C. R. Abernathy, and S. J. Pearton, *Electrochem. Solid-State Lett.* **8**, G20 (2005).
- [107] H. Munekata, H. Ohno, S. von Molnar, A. Segmüller, L. L. Chang, and L. Esaki, *Phys. Rev. Lett.* **63**, 1849 (1989).
- [108] G. Martínez-Criado, A. Somogyi, M. Hermann, M. Eickhoff, and M. Stutzmann, *Jpn. J. Appl. Phys.* **43**, L695 (2004).
- [109] G. Thaler, R. Frazier, B. Gila, J. Stapleton, M. Davidson, C. R. Abernathy, S. J. Pearton, and C. Segre, *Appl. Phys. Lett.* **84**, 1314 (2004).
- [110] K. J. Lee, F. C. Yu, J. A. Kim, D. J. Kim, B. G. Kim, Y. H. Kang, H. J. Kim, and Y. E. Ihm, *Phys. Status Solidi B* **241**, 1525 (2004).
- [111] S. J. Pearton, C. R. Abernathy, M. E. Overberg, G. T. Thaler, D. P. Norton, N. Theodoropoulou, A. F. Hebard, Y. D. Park, F. Ren, J. Kim, and L. A. Boatner, *J. Appl. Phys.* **93**, 1 (2003).
- [112] I. T. Yoon, T. W. Kang, and D. J. Kim, *Mater. Sci. Eng., B*, doi:10.1016/j.mseb.2006.07.017 (2006).
- [113] K. W. Edmonds, S. V. Novikov, M. Sawicki, R. P. Campion, C. R. Staddon, A. D. Giddings, L. X. Zhao, K. Y. Wang, T. Dietl, C. T. Foxon, and B. L. Gallagher, *cond-mat*, 0411476.
- [114] R. Giraud, S. Kuroda, S. Marcet, E. Bellet-Amalric, X. Biquard, B. Barbara, D. Fruchart, D. Ferrand, J. Cibert, and H. Mariette, *Europhys. Lett.* **65**, 553 (2004).
- [115] K. H. Kim, K. J. Lee, D. J. Kim, H. J. Kim, Y. E. Ihm, C. G. Kim, S. H. Yoo, and C. S. Kim, *Appl. Phys. Lett.* **82**, 1775 (2003).
- [116] Y. Y. Yu, R. Zhang, X. Q. Xiu, Z. L. Xie, H. Q. Yu, Y. Shi, B. Shen, S. L. Gu, and Y. D. Zheng, *J. Cryst. Growth* **269**, 270 (2004).

- [117] S. S. A. Seo, M. W. Kim, Y. S. Lee, T. W. Noh, Y. D. Park, G. T. Thaler, M. E. Overberg, C. R. Abernathy, and S. J. Pearton, *Appl. Phys. Lett.* **82**, 4749 (2003).
- [118] G. T. Thaler, R. M. Frazier, J. Stapleton, C. R. Abernathy, S. J. Pearton, J. Kelly, R. Rairigh, A. F. Hebard, and J. M. Zavada, *Electrochem. Solid-State Lett.* **7**, G34 (2004).
- [119] D. O'Mahony, F. McGee, M. Venkatesan, J. G. Lunney, and J. M. D. Coey, *Superlattices Microstruct.* **36**, 403 (2004).
- [120] A. Bittar, H. J. Trodahl, N. T. Kemp, and A. Markwitz, *Appl. Phys. Lett.* **78**, 619 (2001).
- [121] F. Budde, B. J. Ruck, A. Koo, S. Granville, H. J. Trodahl, A. Bittar, G. V. M. Williams, M. J. Ariza, B. Bonnet, D. J. Jones, J. B. Metson, S. Rubanov, and P. Munroe, *J. Appl. Phys.* **98**, 063514 (2005).
- [122] C. Yeh, Z. W. Lu, S. Froyen, and A. Zunger, *Phys. Rev. B* **46**, 10086 (1992).
- [123] K. W. Edmonds, S. V. Novikov, M. Sawicki, R. P. Campion, C. R. Staddon, A. D. Giddings, L. X. Zhao, K. Y. Wang, T. Dietl, C. T. Foxon, and B. L. Gallagher, *Appl. Phys. Lett.* **86**, 152114 (2005).
- [124] Y. Han, M. W. Fay, P. D. Brown, S. V. Novikov, K. W. Edmonds, B. L. Gallagher, R. P. Campion, C. R. Staddon, and C. T. Foxon, *J. Cryst. Growth* **284**, 324 (2005).
- [125] J. Y. Chang, G. H. Kim, J. M. Lee, S. H. Han, H. J. Kim, W. Y. Lee, M. H. Ham, K. S. Huh, and J. M. Myoung, *J. Appl. Phys.* **93**, 7858 (2003).
- [126] P. P. Chen, H. Makino, J. J. Kim, and T. Yao, *Phys. Status Solidi C* **0**, 2882 (2003).
- [127] H. Nakayama, H. Mashita, E. Kulatov, R. Funahashi, and H. Ohta, *J. Magn. Magn. Mater.* **258-259**, 323 (2003).

- [128] J. M. Baik, H. S. Kim, C. G. Park, and J. Lee, *Appl. Phys. Lett.* **83**, 2632 (2003).
- [129] K. H. Ploog, S. Dhar, and A. Trampert, *J. Vac. Sci. Technol. B* **21**, 1756 (2003).
- [130] M. Leszczynski, H. Teisseyre, T. Suski, I. Grzegory, M. Bockowski, J. Jun, S. Porowski, K. Pakula, J. M. Baranowski, C. T. Foxon, and T. S. Cheng, *Appl. Phys. Lett.* **69**, 73 (1996).
- [131] *Handbook of Chemistry and Physics, 86th edition (2005-2006)*, <http://www.hbcnetbase.com>.
- [132] S. Strite and H. Morkoç, *J. Vac. Sci. Tech. B* **10**, 1237 (1992).
- [133] K. Suzuki, T. Kaneko, H. Yoshida, Y. Obi, H. Fujimori, and H. Morita, *J. Alloys. Compd.* **306**, 66 (2000).
- [134] K. Ando, *Appl. Phys. Lett.* **82**, 100 (2003).
- [135] B. K. Rao and P. Jena, *Phys. Rev. Lett.* **89**, 185504 (2002).
- [136] M. Sato, H. Tanida, K. Kato, T. Sasaki, Y. Yamamoto, S. Sonoda, S. Shimizu, and H. Hori, *Jpn. J. Appl. Phys., Part 1* **41**, 4513 (2002).
- [137] S. Podisadło, T. Szyszko, W. Gębicki, J. Gosk, R. Bacewicz, L. Dobrzycki, K. Wozniak, M. Zając, and A. Twardowski, *Chem. Mater.* **15**, 4533 (2003).
- [138] X. Biquard, O. Proux, J. Cibert, D. Ferrand, H. Mariette, R. Giraud, and B. Barbara, *J. Supercond.* **16**, 127 (2003).
- [139] B. He, X. Zhang, S. Wei, H. Oyanagi, S. V. Novikov, K. W. Edmonds, C. T. Foxon, G. Zhou, and Y. Jia, *Appl. Phys. Lett.* **88**, 051905 (2006).
- [140] A. Y. Polyakov, A. V. Govorkov, N. B. Smirnov, N. Y. Pashkova, G. T. Thaler, M. E. Overberg, R. Frazier, C. R. Abernathy, S. J. Pearton, J. Kim, and F. Ren, *J. Appl. Phys.* **92**, 4989 (2002).

- [141] T. Kondo, S. Kuwabara, H. Owa, and H. Munekata, *J. Cryst. Growth* **237-239**, 1353 (2002).
- [142] T. Miura, Y. Yamamoto, S. Itaya, K. Suga, K. Kindo, T. Takenobu, Y. Iwasa, and H. Hori, *Physica B* **346-347**, 402 (2004).
- [143] T. Graf, M. Gjukic, M. S. Brandt, M. Stutzmann, and O. Ambacher, *Appl. Phys. Lett.* **81**, 5159 (2002).
- [144] A. Wolos, A. Wyszomolek, M. Kaminska, A. Twardowski, M. Bockowski, I. Grzegory, S. Porowski, and M. Potemski, *Phys. Rev. B* **70**, 245202 (2004).
- [145] A. Wolos, M. Palczewska, M. Zajac, J. Gosk, M. Kaminska, A. Twardowski, M. Bockowski, I. Grzegory, and S. Porowski, *Phys. Rev. B* **69**, 115210 (2004).
- [146] M. Strassburg, M. H. Kane, A. Asghar, Q. Song, Z. J. Zhang, J. Senawiratne, M. Alevli, N. Dietz, C. J. Summers, and I. T. Ferguson, *J. Phys.: Condens. Matter* **18**, 2615 (2006).
- [147] R. Y. Korotkov, J. M. Gregie, B. Han, and B. W. Wessels, *Physica B* **308-310**, 30 (2001).
- [148] R. Y. Korotkov, J. M. Gregie, and B. W. Wessels, *Appl. Phys. Lett.* **80**, 1731 (2002).
- [149] O. Gelhausen, E. Malguth, M. R. Phillips, E. M. Goldys, M. Strassburg, A. Hoffmann, T. Graf, M. Gjukic, and M. Stutzmann, *Appl. Phys. Lett.* **84**, 4514 (2004).
- [150] I. T. Yoon, T. W. Kang, M. C. Jeong, M. H. Ham, and J. M. Myoung, *Appl. Phys. Lett.* **85**, 4878 (2004).
- [151] T. Yamamoto, S. Marcet, E. Gheeraert, S. Kuroda, H. Mariette, D. Ferrand, and J. Cibert, *J. Cryst. Growth* **275**, e2233 (2005).
- [152] S. Marcet, D. Ferrand, S. Kuroda, E. Gheeraert, R. M. Galera, J. Cibert, and H. Mariette, *Mater. Sci. Eng., B* **126**, 240 (2006).

- [153] Y. Shon, Y. H. Kwon, T. W. Kang, X. Fan, D. Fu, and Y. Kim, *J. Cryst. Growth* **245**, 193 (2002).
- [154] G. T. Thaler, M. E. Overberg, B. Gila, R. Frazier, C. R. Abernathy, S. J. Pearton, J. S. Lee, S. Y. Lee, Y. D. Park, Z. G. Khim, J. Kim, and F. Ren, *Appl. Phys. Lett.* **80**, 3964 (2002).
- [155] T. Sasaki, S. Sonoda, Y. Yamamoto, K. Suga, S. Shimizu, K. Kindo, and H. Hori, *J. Appl. Phys.* **91**, 7911 (2002).
- [156] M. Ham, M. Jeong, W. Lee, J. Myoung, J. Chang, and S. Han, *Jpn. J. Appl. Phys., Part 2* **42**, L1372 (2003).
- [157] S. J. Pearton, C. R. Abernathy, G. T. Thaler, R. Frazier, F. Ren, A. F. Hebard, Y. D. Park, D. P. Norton, W. Tang, M. Stavola, J. M. Zavada, and R. G. Wilson, *Physica B* **340-342**, 39 (2003).
- [158] H. Hori, S. Sonoda, T. Sasaki, Y. Yamamoto, S. Shimizu, K. Suga, and K. Kindo, *Physica B* **324**, 142 (2002).
- [159] K. Ando, *Appl. Phys. Lett.* **82**, 100 (2003).
- [160] A. Wolos, M. Palczewska, Z. Wilamowski, M. Kaminska, A. Twardowski, M. Bockowski, I. Grzegory, and S. Porowski, *Appl. Phys. Lett.* **83**, 5428 (2003).
- [161] R. Giraud, S. Kuroda, S. Marcet, E. Bellet-Amalric, X. Biquard, B. Barbara, D. Fruchart, D. Ferrand, J. Cibert, and H. Mariette, *J. Magn. Magn. Mater.* **272-276**, e1557 (2004).
- [162] M. Zając, J. Gosk, M. Kamińska, A. Twardowski, T. Szyszko, and S. Posiadło, *Appl. Phys. Lett.* **79**, 2432 (2001).
- [163] H. C. Jeon, T. W. Kang, T. W. Kim, J. Kang, and K. J. Chang, *Appl. Phys. Lett.* **87**, 092501 (2005).
- [164] K. H. Kim, K. J. Lee, D. J. Kim, C. S. Kim, H. C. Lee, C. G. Kim, S. H. Yoo, H. J. Kim, and Y. E. Ihm, *J. Appl. Phys.* **93**, 6793 (2003).

- [165] S. Dhar, O. Brandt, A. Trampert, L. Daweritz, K. J. Friedland, K. H. Ploog, J. Keller, B. Beschoten, and G. Guntherodt, *Appl. Phys. Lett.* **82**, 2077 (2003).
- [166] M. Zając, J. Gosk, E. Grzanka, M. Kamińska, A. Twardowski, B. Strojek, T. Szyszko, and S. Podsiadło, *Appl. Phys. Lett.* **93**, 4715 (2003).
- [167] H. Yang, H. Al-Britthen, A. R. Smith, J. A. Borchers, R. L. Cappelletti, and M. D. Vaudin, *Appl. Phys. Lett.* **78**, 3860 (2001).
- [168] A. Janotti, S. Wei, and L. Bellaiche, *Appl. Phys. Lett.* **82**, 766 (2003).
- [169] J. Häglund, G. Grimvall, T. Jarlborg, and A. F. Guillermet, *Phys. Rev. B* **43**, 14400 (1991).
- [170] H. Shimizu, M. Shirai, and N. Suzuki, *J. Phys. Soc. Jpn.* **66**, 3147 (1997).
- [171] B. R. Sahu and L. Kleinman, *Phys. Rev. B* **68**, 113101 (2003).
- [172] W. R. L. Lambrecht, M. Prikhodko, and M. S. Miao, *Phys. Rev. B* **68**, 174411 (2003).
- [173] M. Marques, L. K. Teles, L. M. R. Scolfaro, J. Furthmüller, F. Bechstedt, and L. G. Ferreira, *Appl. Phys. Lett.* **86**, 164105 (2005).
- [174] M. S. Miao and W. R. L. Lambrecht, *Phys. Rev. B* **71**, 214405 (2005).
- [175] K. Suzuki, T. Kaneko, H. Yoshida, Y. Obi, H. Fujimori, and H. Morita, *J. Alloys Compd.* **306**, 66 (2000).
- [176] K. Suzuki, Y. Yamaguchi, T. Kaneko, H. Yoshida, Y. Obi, H. Fujimori, and H. Morita, *J. Phys. Soc. Jpn.* **70**, 1084 (2001).
- [177] A. Leineweber, R. Niewa, H. Jacobs, and W. Kockelmann, *J. Mater. Chem.* **10**, 2827 (2000).
- [178] H. Yang, H. Al-Britthen, E. Trifan, D. C. Ingram, and A. R. Smith, *J. Appl. Phys.* **91**, 1053 (2002).



- [179] K. Suzuki, T. Suzuki, Y. Fujinaga, T. Kaneko, H. Yoshida, Y. Obi, and S. Tomiyoshi, *J. Alloys Compd.* **360**, 34 (2003).
- [180] K. Sato, P. H. Dederichs, and H. Katayama-Yoshida, *Physica B* **376-377**, 639 (2006).
- [181] Y. Kang and D. C. Ingram, *J. Appl. Phys.* **93**, 3954 (2003).
- [182] A. Koo, F. Budde, B. J. Ruck, H. J. Trodahl, A. Bittar, A. Preston, and A. Zeinert, *J. Appl. Phys.* **99**, 034312 (2006).
- [183] P. Stumm and D. A. Drabold, *Phys. Rev. Lett.* **79**, 677 (1997).
- [184] U. D. Lanke, A. Koo, S. Granville, H. J. Trodahl, A. Markwitz, V. J. Kennedy, and A. Bittar, *Mod. Phys. Lett.* **15**, 1355 (2001).
- [185] L. R. Doolittle, *Nucl. Inst. Meth. B* **9**, 344 (1986).
- [186] U. D. Lanke, A. Koo, B. J. Ruck, H. K. Lee, A. Markwitz, V. J. Kennedy, M. J. Ariza, D. J. Jones, J. Rozière, A. Bittar, and H. J. Trodahl, *Mat. Res. Symp. Proc.* **693**, 347 (2002).
- [187] B. Ravel and M. Newville, *J. Synchrotron Rad.* **12**, 537 (2005).
- [188] S. Granville, B. J. Ruck, F. Budde, A. Koo, J. E. Downes, H. J. Trodahl, A. Bittar, N. Strickland, G. V. M. Williams, W. R. L. Lambrecht, T. Learmonth, K. E. Smith, V. J. Kennedy, A. Markwitz, and T. Schmitt, *Phys. Rev. B* **72**, 205127 (2005).
- [189] P. Y. Yu and M. Cardona, *Fundamentals of Semiconductors*, (Springer, Heidelberg, 1999).
- [190] G. Turrell and J. Corset, editors, *Raman Microscopy - Developments and Applications*, (Academic Press, London, 1996).
- [191] B. J. Ruck, PhD thesis, Victoria University of Wellington, 1998.
- [192] O. K. Andersen, O. Jepsen, and M. Šob, *Electronic Band Structure and its Applications*, (Springer, Heidelberg, 1987).

- [193] W. R. L. Lambrecht, M. Prikhodko, and M. S. Miao, Phys. Rev. B. **68**, 174411 (2003).
- [194] W. R. L. Lambrecht, B. Segall, J. Rife, W. R. Hunter, and D. K. Wickenden, Phys. Rev. B. **51**, 13516 (1995).
- [195] R. Bacewicz, J. Filipowicz, S. Podsiadło, T. Szyszko, and M. Kamiński, J. Phys. Chem. Solids **64**, 1469 (2003).
- [196] A. Koo, PhD thesis, Victoria University of Wellington, 2005.
- [197] A. Compaan and H. J. Trodahl, Phys. Rev. B **29**, 793 (1984).
- [198] H. J. Trodahl, F. Budde, B. J. Ruck, S. Granville, A. Koo, and A. Bittar, J. Appl. Phys. **97**, 084309 (2005).
- [199] H. J. Trodahl, C. E. A. Grigorescu, A. Bittar, F. Budde, B. J. Ruck, S. Granville, G. V. M. Williams, O. Monnereau, and R. Notonier, J. Non-Cryst. Solids **352**, 1282 (2006).
- [200] B. J. Ruck, A. Koo, U. D. Lanke, F. Budde, S. Granville, H. J. Trodahl, A. Bittar, J. B. Metson, V. J. Kennedy, and A. Markwitz, Phys. Rev. B. **70**, 235202 (2004).
- [201] H. Yang, H. Al-Brithen, E. Trifan, D. C. Ingram, and A. R. Smith, J. Appl. Phys. **91**, 1053 (2002).
- [202] J. E. Greedan, J. Mater. Chem. **11**, 37 (2001).
- [203] M. P. Marder, *Condensed Matter Physics*, (Wiley, New York, 2000).
- [204] S. Granville and A. R. Smith, *et. al* (unpublished) .
- [205] A. I. Lichtenstein and M. I. Katsnelson, Phys. Rev. B. **57**, 6884 (1998).
- [206] A. Georges, G. Kotliar, W. Krauth, and M. Rozernberg, Rev. Mod. Phys. **68**, 13 (1996).
- [207] B. J. Ruck, A. Koo, U. D. Lanke, F. Budde, H. J. Trodahl, G. V. M. Williams, A. Bittar, J. B. Metson, E. Nodwell, T. Tiedje, A. Zamina, and S. Eisebatt, J. Appl. Phys. **96**, 3571 (2004).

- [208] P. Glans, P. Skytt, K. Gunnelin, J. Guo, and J. Nordgren, *J. Electron Spectrosc. Relat. Phenom.* **82**, 193 (1996).
- [209] N. Sclar, *J. Appl. Phys* **35**, 1534 (1964).
- [210] R. J. Gambino and J. J. Cuomo, *J. Electrochem. Soc.* **113**, 401 (1966).
- [211] R. J. Gambino, T. R. McGuire, H. A. Alperin, and S. J. Pickart, *J. Appl. Phys.* **41**, 933 (1970).
- [212] R. A. Cutler and A. W. Lawson, *J. Appl. Phys.* **46**, 2739 (1975).
- [213] D. B. McWhan, *J. Chem. Phys.* **44**, 3528 (1966).
- [214] T. R. McGuire, R. J. Gambino, S. J. Pickart, and H. A. Alperin, *J. Appl. Phys.* **40**, 1009 (1969).
- [215] H. A. Eick, N. C. Baenziger, and L. Eyring, *J. Am. Chem. Soc.* **78**, 5987 (1956).
- [216] D. P. Schumacher and W. E. Wallace, *J. Appl. Phys.* **36**, 984 (1965).
- [217] H. R. Child, M. K. Wilkinson, J. W. Cable, W. C. Koehler, and E. O. Wollan, *Phys. Rev.* **131**, 922 (1963).
- [218] R. Didchenko and F. P. Gortsema, *J. Phys. Chem. Solids* **24**, 863 (1963).
- [219] D. P. Schumacher and W. E. Wallace, *Inorg. Chem.* **5**, 1563 (1966).
- [220] D. X. Li, Y. Haga, H. Shida, and T. Suzuki, *Physica B* **199&200**, 631 (1994).
- [221] P. Wachter and E. Kaldis, *Solid State Commun.* **34**, 241 (1980).
- [222] L. F. Schneemeyer, R. B. van Dover, and E. M. Gyorgy, *J. Appl. Phys.* **61**, 3543 (1987).
- [223] J. Q. Xiao and C. L. Chien, *Phys. Rev. Lett.* **76**, 1727 (1996).
- [224] F. Leuenberger, A. Parge, W. Felsch, K. Fauth, and M. Hessler, *Phys. Rev. B* **72**, 014427 (2005).

- [225] E. Shalaan and H. Schmitt, *Opt. Commun.* **260**, 588 (2006).
- [226] F. Hulliger, *Handbook on the Physics and Chemistry of Rare Earths*, Chapter 33 (North-Holland Publishing Company, 1979).
- [227] G. Busch, P. Junod, O. Vogt, and F. Hulliger, *Phys. Lett.* **6**, 79 (1963).
- [228] G. Busch, P. Junod, F. Levy, A. Menth, and O. Vogt, *Phys. Lett.* **14**, 264 (1965).
- [229] G. Busch, *J. Appl. Phys.* **38**, 1386 (1967).
- [230] R. C. Brown and N. J. Clark, *J. Inorg. Nucl. Chem.* **36**, 2507 (1974).
- [231] P. Scobinger-Papamantellos, P. Fischer, O. Vogt, and E. Kaldis, *J. Phys. C: Solid State Phys.* **6**, 725 (1973).
- [232] D. X. Li, Y. Haga, H. Shida, T. Suzuki, Y. S. Kwon, and G. Kido, *J. Phys. Condens. Matter* **9**, 10777 (1997).
- [233] V. W. Klemm and G. Winkelmann, *Z. anorg. allg. Chem.* **231**, 138 (1956).
- [234] A. Hasegawa and A. Yanase, *J. Phys. Soc. Jpn.* **42**, 492 (1977).
- [235] W. R. L. Lambrecht, *Phys. Rev. B* **62**, 13538 (2000).
- [236] A. G. Petukhov, W. R. L. Lambrecht, and B. Segall, *Phys. Rev. B* **53**, 4324 (1996).
- [237] D. B. Ghosh, M. De, and S. K. De, *Phys. Rev. B* **72**, 045140 (2005).
- [238] C. Duan, R. F. Sabiryanov, J. Liu, W. N. Mei, P. A. Dowben, and J. R. Hardy, *Phys. Rev. Lett.* **94**, 237201 (2005).
- [239] H. Yamada, T. Fukawa, T. Muro, Y. Tanaka, S. Imada, S. Suga, D.-X. Li, and T. Suzuki, *J. Phys. Soc. Jpn.* **65**, 1000 (1996).
- [240] P. Larson and W. R. L. Lambrecht, *Phys. Rev. B* **74**, 085108 (2006).
- [241] F. Leuenberger, PhD thesis, University of Göttingen, 2004.

- 
- [242] F. Leuenberger, A. Parge, W. Felsch, F. Baudalet, C. Giorgetti, E. Dartyge, and F. Wilhelm, *Phys. Rev. B* **73**, 214430 (2006).
- [243] M. Kuznietz, *J. Appl. Phys.* **42**, 1470 (1971).
- [244] W. R. McKenzie, P. Munroe, F. Budde, B. Ruck, S. Granville, and H. Trodahl, *Curr. Appl. Phys.* **6**, 407 (2006).
- [245] J. Kordis, K. A. Gingerich, R. J. Seyse, E. Kaldis, and R. Bischof, *J. Cryst. Growth* **17**, 53 (1972).
- [246] S. Bhattacharjee and S. M. Jaya, *Eur. Phys. J. B.* **49**, 305 (2006).